A CRYSTALLOGRAPHIC AND MECHANISTIC INVESTIGATION OF MANGANESE(I) TRICARBONYL COMPLEXES

By

THEMBANI TWALA

A thesis submitted to meet the requirements for the degree of

MAGISTER SCIENTIAE

In the

DEPARTMENT OF CHEMISTRY

FACULTY OF SCIENCE

At the

UNIVERSITY OF THE FREE STATE

Supervisor: Prof. Hendrik G. Visser

Co-Supervisor: Dr. Marietjie Schutte-Smith

November 2013

A CRYSTALLOGRAPHIC AND MECHANISTIC INVESTIGATION OF MANGANESE(I) TRICARBONYL COMPLEXES

By

THEMBANI NTHABISENG TWALA

A thesis submitted to meet the requirements for the degree of

MAGISTER SCIENTIAE

In the

DEPARTMENT OF CHEMISTRY

FACULTY OF SCIENCE

At the

UNIVERSITY OF THE FREE STATE

Supervisor: Prof. Hendrik G. Visser

Co-Supervisor: Dr. Marietjie Schutte-Smith

November 2013

OPSOMMING

Mangaan word grotendeels gebruik as katalis in die epoksidasie van olefiene en die selektiewe oksidasie van ongeaktiveerde C-H bindings in alkane. Nog ‘n belangrike gebruik van mangaan is die katalise van water oksidasie. Mangaan komplekse word gebruik in die produksie van waterstof deur middel van water splyting.

Baie van die radiofarmaseutiese studies in literatuur is gebasseer op tegnesium as metaal. ^{99m}Tc het ‘n paar gepaste eienskappe vir potensiële radiofarmaseutiese middels en word as gevolg daarvan gesien as ‘n ideale radio isotoop. Renium word gebruik as model vir tegnesium radiofarmaseutiese middels terwyl ^{186}Re en ^{188}Re gebruik word in middels vir been metastase.

Mangaan is toksies vir die menslike liggaam en daarom word dit nie gebruik in radiofarmasie nie. Daar is wel studies gedoen op die onderdrukking van kanker gewasse deur MnSOD, ‘n mitochondriale ensiem. Bitter min navorsing is gedoen op die koördinasie chemie van mangaan, veral die trikarboniel akwa sisteme. Sover is daar slegs 5 mangaan trikarboniel akwa komplekse gelys op die CSD.

In hierdie studie word daar ‘n vergelyking getref tussen mangaan (I) and renium (I) trikarboniel komplekse. Kemp en Schutte *et al*. het verskeie renium (I) trikarboniel komplekse gesintetiseer met N,N’-, N,O- en O,O’-bidentate ligande. 2,2’-Bipiridien (Bipy) en 1,10-fenantrolien was gebruik as N,N’-bidentate ligande, quinolien-2,4-dikarboksielsuur (2,4-Quin) en piridien-2-karboksielsuur (Pico) as N,O-bidentate ligande en 3-hidroksieflavoon (Flav) en tropoloon (Trop) as O,O’-bidentate ligande. Dieselfde N,N’- en N,O- bidentate ligande sowel as 3-hidroksieflavoon is in hierdie studie gebruik om sodoende ‘n goeie vergelyking te kan maak tussen die renium (I) en mangaan (I) komplekse.

Die sintese van al die komplekse word gegee in Hoofstuk 3. Die komplekse is gekarakteriseer deur middel van UV/vis, ^{13}C KMR, ^{1}H KMR sowel as IR. Slegs twee van die komplekse is gekarateriseer met behulp van X-straal kristallografie, *fac*-[Mn(CO)$_3$(Bipy)(H$_2$O)][CF$_3$SO$_3$] en *fac*-[Mn(CO)$_3$(Phen)(H$_2$O)][CF$_3$SO$_3$]. Beide die monokliniese komplekse het in die $P2_1/c$ ruimtegroep gekristalliseer. Die Mn-N,N’ bindingsafstande is gerapporteer as 2.051(2) Å en 2.058(19) Å vir *fac*-[Mn(CO)$_3$(Phen)(H$_2$O)][CF$_3$SO$_3$], en 2.042(4) Å en 2.040(4) Å vir *fac*-[Mn(CO)$_3$(Bipy)(H$_2$O)][CF$_3$SO$_3$].

Opsomming

Die metanol substitusie reaksie tussen *fac*-$[Mn(CO)_3(Phen)(MeOH)]^+$, *fac*-$[Mn(CO)_3(Bipy)(MeOH)]^+$, *fac*-$[Mn(CO)_3(Pico)(MeOH)]$ en *fac*-$[Mn(CO)_3(2,4\text{-}Quin)(MeOH)]$ en verskillende monodentate ligande, piridien (Py), tio-ureum (TU) en bromied ione (Br^-), is gevolg. Eerstens het die eerste orde tempo konstante vir al die reaksies die volgende tendens gevolg: k_1 Br^- > k_1 TU > k_1 Py en tweedens het die N,O-bidentate komplekse vinniger reageer as die N,N'-bidentate komplekse. Beide hierdie tendense is ook waargeneem vir die renium (I) trikarboniel komplekse. Effens negatiewe $\Delta S^{\dagger}$ waardes is waargeneem vir al die reaksies wat 'n uitruilings assosiatiewe tipe meganisme voorstel.

In geheel is daar bevestig dat die mangaan komplekse baie vinniger reageer as die ooreenstemmende renium komplekse. 'n Toename (vanaf Re na Mn) in k_1 van ~10 en ~7 is waargeneem vir die reaksie tussen die bromied ione en die Phen en Bipy komplekse onderskeidelik. Vir die reaksie tussen piridien en die Phen en Bipy komplekse is 'n toename van ~40 en ~30 onderskeidelik waargeneem. Die Pico komplekse het 'n toename in k_1 getoon van 'n faktor ~40 vir die reaksie met bromied ione en 'n faktor ~590 vir die reaksie met piridien. Die komplekse met quinolien-2,4-dikarboksielsuur as bidentate ligand het 'n massiewe toename van ~1150 in die k_1 waarde getoon vanaf die renium kompleks na die mangaan kompleks. Hierdie resultate dui die invloed wat die quinolien-2,4-dikarboksielsuur ligand op die mangaan (I) senter het aan.

TABLE OF CONTENTS

TABLE OF CONTENTS

Table of Contents

Table of Contents

Table of Contents

ABBREVIATIONS

2,4-Quin	quinoline-2,4-dicarboxylic acid
Å	angstrom
BBB	blood brain barrier
BFC	bifunctional chelate
Bipy	2,2'-bipyridyl
Br^-	bromide ions
DMSA	dimercaptosuccinic acid
fac	*facial*
Flav	3-hydroxyflavone
FT-IR	fourier transform infra-red
HOMO	highest occupied molecular orbital
IR	infra-red
L-L'-bid	bidentate ligand
LUMO	lowest occupied molecular orbital
MAG_3	mercaptoacetylglycylglycylglycine
MEMRI	manganese enhanced magnetic resonance imaging
MIBI	2-methoxy-2-methylpropylisocyanide
MnSOD	manganese superoxide dismutase
MRI	magnetic resonance imaging
NMR	nuclear magnetic resonance spectroscopy
PET	positron emission tomography
Phen	1,10-phenanthroline
Pico	pyridine-2-carboxylic acid
Py	pyridine
SPECT	single photon emission computed tomography
$t_{1/2}$	half-life
Trop	tropolone
TU	thiourea
UV/vis	ultraviolet/visible spectroscopy

Abbreviations

α	alpha
β^-	beta
γ	gamma
β^+	positron
σ	sigma
π	pi
ν_{CO}	C=O stretching frequency
keV	kilo electron volts
MeV	mega electron volts
$\Delta H^\dagger$	enthalpy activation energy
$\Delta S^\dagger$	entropy activation energy
$\Delta V^\dagger$	volume of activation
k_{obs}	observed *pseudo* first-order rate constant
k_1	first-order rate constant for forward reaction
k_{-1}	rate constant for reverse reaction
K_1	equilibrium constant
°	degrees

ABSTRACT

Manganese has largely been used as a catalyst in epoxidation of olefins and the selective oxidation of unactivated C-H bonds in alkanes. Another major use of manganese is in water oxidizing catalysis, where manganese compounds are used in the production of hydrogen by water splitting. By looking at the manganese triad, a lot of radiopharmaceutical studies have been performed with Technetium. ^{99m}Tc is the radionuclide of choice since it has the ideal properties necessary for potential radiopharmaceuticals. Rhenium has been used as model for technetium radiopharmaceuticals and ^{188}Re and ^{186}Re have proved their use in bone metastases.

Manganese has not been used in radiopharmaceuticals as it is somewhat toxic to the body. Some studies have been performed on tumor suppression using MnSOD, a mitochondrial enzyme. Very little work has been done on manganese coordination chemistry especially in terms of tricarbonyl aqua complexes. So far about 5 manganese tricarbonyl aqua complexes have been reported on the CSD.

In this study, a comparison of manganese (I) and rhenium (I) tricarbonyl complexes is made. Rhenium (I) tricarbonyl aqua complexes have been synthesized by Kemp and Schutte *et al*. using N,N'-, N,O- and O,O'- bidentate ligands. The chosen N;N'-bidentate ligands are 2,2'-bipyridyl (Bipy) and 1,10-phenanthroline (Phen), N,O-bidentate ligands are quinoline-2,4-dicarboxylic acid (2,4-Quin) and picolinic acid (Pico) and finally the O,O'-bidentate ligands chosen were 3-hydroxyflvone (Flav) and tropolone (Trop). In this study, the same N,N'- and N,O-bidentate ligand systems were used as well as 3-hydroxyflavone as O,O'-bidentate ligand in order to successfully compare these two metal cores.

The synthesis of all the complexes has been reported in Chapter 3 and these were characterized by UV/vis, ^{13}C NMR, ^{1}H NMR and IR. Only two of the complexes were characterized by X-ray diffraction; *fac*-$[Mn(CO)_3(Bipy)(H_2O)][CF_3SO_3]$ and *fac*-$[Mn(CO)_3(Phen)(H_2O)][CF_3SO_3]$. These monoclinic complexes both crystallized in the $P2_1/c$ space group. The Mn-N,N' bond distances were 2.051(2) Å and 2.058(19) Å for *fac*-$[Mn(CO)_3(Phen)(H_2O)][CF_3SO_3]$, and 2.042(4) Å and 2.040(4) Å for the *fac*-$[Mn(CO)_3(Bipy)(H_2O)][CF_3SO_3]$ crystal structure.

A kinetic study was performed for the reaction between *fac*-$[Mn(CO)_3(Phen)(MeOH)]^+$, *fac*-$[Mn(CO)_3(Bipy)(MeOH)]^+$, *fac*-$[Mn(CO)_3(Pico)(MeOH)]$ and *fac*-$[Mn(CO)_3$(2,4-Quin)(MeOH)] and different monodentate entering ligands pyridine (Py), thiourea (TU)

Abstract

and bromide ions (Br^-). For all the reactions, the first order rate constants followed the following trend: k_1 Br^- > k_1 TU > k_1 Py. It was also observed that the N,O-bidentate complexes overall reacted faster than the N,N'-bidentate ligands. Both these trends were observed for the Re (I) complexes as well. Slightly negative $\Delta S^{\dagger}$ values, with large esd's, were observed for all of the reactions which indicates towards an associative interchange mechanism.

Overall, it was confirmed that the manganese complexes reacted much faster than the corresponding rhenium complexes. For the Phen and Bipy complexes, an increase in k_1 of ~10 and ~7 for the reaction with bromide ions and ~40 and ~30 for the reaction with pyridine was found respectively. The Pico complexes showed an increase in k_1 of a factor ~40 for the reaction with bromide ions and a factor ~590 for the reaction with pyridine. The complexes with the quinoline-2,4-dicarboxylic acid as bidentate ligand showed an tremendous increase of ~1150 for the reaction with pyridine from the rhenium complex to the manganese complex. This indicates the influence quinoline-2,4-dicarboxylic acid has on the reactivity of the manganese (I) centre.

First and foremost, I would like to thank God for helping me against all odds, for guiding and supporting me to complete this degree. I am living proof that all things are possible through Him. I am in awe everyday of all the blessings He showers me with. He truly is an amazing God.

I would like to give a big thank you to Prof André Roodt who gave me the opportunity to be in his research group. Because of this I have grown and developed into a better scientist. I am very honoured and proud to be a part of this amazing research group, it was a privilege to be a part of this team.

To Prof Deon Visser, thank you for seeing such great potential in me and for pushing me to my limits so that I finally saw the potential I have. I do not think I would have been this far if it wasn't for you believing in me; you truly are a great motivator and supervisor!

To Marietjie Schutte-Smith, I am truly blessed to have you around. Thank you for all the patience and support and helping me time and time again. Thank you for all your inputs, I don't think I would have made it through these two years if you weren't there guiding me. Because of you and Deon I developed into a better scientist and person.

To the inorganic group, I would like to thank everyone for the help and for the great group members that you are.

To Leandra, Carla, Ilana, Maryke, Truidie, Alice and Tinus; thank you for the support you have shown me since day one in the group. You never hesitated to help me when I needed it, I appreciate it. A special thank you to Carla and Ilana for all the training with the equipment, again I truly appreciate it.

To my friends; Dika, Sibongile, Khanya and Pholani, I want to thank you for all the laughs I shared with you since our honours year, it has been amazing!

To my wonderful mother, Busisiwe Molefe, thank you for being there and supporting my studies since the beginning. You have been through drum majorette competitions, sport matches and never have I heard you complain. I am the young woman I am because of you. You are my rock, my support system and the strongest woman I know. Thank you for encouraging me every time I wanted to give up. I hope you know that I would not be here at the end of my MSc studies had it not been for your strength. Thank You!!

To my siblings, Sandisile and Fana, I have been truly blessed to have you in my life. You two have also been the best support and I only hope to inspire you to study hard and do what you love. You mean the world to me. To my friend, my adopted sister, Nnini Moabi, thank you for staying up with me and being my alarm clock. I really appreciate you and your friendship!

Last but not least, I would like to thank my late grandparents, Zibuse and Christinah Twala. Every day I brag about how blessed I am to have been raised by grandparents like you. I would like to dedicate this thesis to the both of you because if it wasn't for the foundation you laid for us, I would never have this chance. Thank you for your love and support!

APPENDIX A: Basic Theory on IR, UV/vis, NMR, Chemical Kinetics and XRD

A.1 Introduction

Infrared(IR), Ultraviolet-visible(UV/vis) and Nuclear Magnetic Resonance(NMR) spectroscopy as well as chemical kinetics and X-Ray diffraction(XRD) are a few characterization techniques used in chemistry to identify molecular structures. The spectroscopy characterization techniques (IR, ^{1}H and ^{13}C-NMR and UV/vis) make use of absorption, transmission and reflection of radiation in order to determine the molecular structures, while the XRD technique shows the actual arrangement of atoms in space. Chemical kinetics is used to determine the rate of these chemical reactions. All of the Mn (I) tricarbonyl complexes in this study were characterized using the above mentioned techniques.

A.2 Infrared Spectroscopy

Infrared spectroscopy is a technique established to measure the physical property of matter and chemical composition. It is a measurement of the ability to absorb, transmit or reflect radiation. The advantage of infrared spectroscopy is that any sample can be studied, whether it is a liquid, a solution, a paste, a powder or a gas. This technique is based mainly on the vibrations from the atoms of a molecule. A spectrum of the sample is obtained by passing radiation through that specific sample. A fraction of the incident radiation that is absorbed is then determined at a particular energy.[1]

A.2.1 Electromagnetic Radiation

The electromagnetic spectrum has several systems of radiation namely: radiowave, microwave, infrared, ultraviolet-visible, x-ray as well as γ-ray. The term electromagnetic radiation originates from Maxwell's classical theory of electrodynamics and magnetodynamics. In this theory, Maxwell interpreted the nature of the various

[1] N.L. Alpert., W.E. Keiser., H.A. Szymanski., *IR: Theory and Practice of Infrared Spectroscopy*, Plenum/Rosetta,1973, 1.

radiations. Radiation is a combination of two mutually perpendicular electric and magnetic fields that oscillate in a single plane at right angles to each other. The fields are diffused as a sine wave. The distance between two positions in the same phase is known as the wavelength (λ) and the number of times the electromagnetic radiation oscillates is called the frequency. The velocity (v) of the propagation in vacuum is constant for all regions of the spectrum and known as velocity of light, $c = 3 \times 10^8$ m.s^{-1}.

Therefore

$$c = \lambda\nu \qquad \text{(Eq. 1)}$$

Einstein, Plank and Bohr worked on proving that electromagnetic radiation could be reported as a stream of particles. Bohr's equation can be written as follows:

$$E = h\nu \qquad \text{(Eq. 2)}$$

Where *E* is the energy, h is Planck's constant and ν is the velocity. [2]

A.2.2 The Infrared Process and Uses

When infrared radiation is absorbed the process is known as a quantized process, where molecules are excited to a higher energy state. A molecule only absorbs selected energies of infrared radiation and this absorption of infrared radiation shows energy changes of the order from 8 kJ.mol^{-1} to 40 kJ.mol^{-1}.

The radiation that takes place in this energy range corresponds to that of the stretching and the bending vibrational frequencies of the bonds in most covalent molecules. The only bonds in a molecule that can absorb infrared energy are those that possess a dipole moment that changes as a function of time. [3]

The infrared spectrum can be used to identify a unique molecule as much as a fingerprint can be used for humans. No two molecules with different structures have the exact same infrared absorption pattern or infrared spectrum. Every type of bond has its own different natural frequency of vibration.

[2] Stuart, B., *Modern Infrared Spectroscopy*, John Wiley & Sons, Ltd., 1996, 2.
[3] Pavia, D.L., Lampman, G.M., Kriz, G.S., *Introduction To Spectroscopy*, 3rd Ed., Thomson Learning, Inc., 2001, 15.

A.2.3 Fourier Transform Spectrometers

Modern infrared spectrometers are designed with an optical pathway that produces a pattern known as an interferogram. This wave-like pattern contains the frequencies that make up an infrared spectrum. The Fourier transform is a mathematical operation which is capable of separating the individual absorption frequencies from the interferogram to produce a spectrum identical to dispersive spectrometers. This is known as Fourier transform infrared spectrometer (FT-IR). A Fourier transform provides a spectrum with a better signal-to-noise ratio. The advantage of the FT-IR is the fact that it has great speed and great sensitivity.

On a computer-interfaced FT-IR, a spectrum is obtained by first obtaining an interferogram of the "background". The "background" consists of infrared-active atmospheric gases, carbon dioxide and water vapour. A sample is then placed into the beam and a spectrum from the Fourier transform is obtained. A spectrum of the sample analysed is yielded when the computer software automatically subtracts the spectrum of the background from the spectrum of the sample. [3]

A.2.4 Modes of Vibration

When molecular dipoles experience changes that are related to vibrations and rotations, there is an interaction between the infrared radiation and matter. A molecule can be viewed as a system of masses that are joined by bonds that possess spring-like properties. Diatomic molecules are a simple example. They possess three degrees of translational freedom and two degrees of rotational freedom and they also have atoms that move relative to one another. These stretching and bending movements are generally known as vibrations. Diatomic molecules have 3N degrees of freedom since they contain N number of atoms. There are two types of vibrations that are involved:

- Stretching – Change in bond length.
- Bending – Change in bond angle.

Bonds that stretch in-phase experience what is known as symmetrical stretching while those that stretch out-of-phase experience asymmetric stretching (Figure 1).

In bending vibrations, there should be a plane cutting the hydrogen and carbon atoms of a molecule. The hydrogens move in the same direction or in opposite directions of this plane. There are four types of bending vibrations

namely: scissoring, rocking, wagging and twisting (Figure 2). [2]

Symmetric Stretch **Asymmetric Stretch**

Figure 1: Diagram illustrating the stretching vibrations.

Rocking **Scissoring**

Twisting **Wagging**

Figure 2: Diagrams illustrating the bending vibrations.

The absorption of an infrared spectrum is contributed to vibrations. For the absorption to appear there is a change in the dipole moment of the molecule. The absorption band is more intense when the change in dipole is large. Carbonyls can show an intense absorption peak since the dipole moment increases when the CO bond is stretched.

The asymmetrical molecules have more vibrations than symmetrical molecules and for this reason the vibrations from the symmetrical molecules are weaker and will not lead to a change in dipole. [2]

A.2.5 The Infrared of Metal Carbonyls

The C-O stretching of carbonyl ligands in metal complexes give very sharp and strong bands. These are clearly separated from other bands of other ligands present. The position of the terminal carbonyl band is determined by a process known as back-bonding. This is when the electrons from the d-orbitals of the metal bond into π^* antibonding orbitals of the ligand. This bonding weakens the C-O bond and the wave number is lower than that of the free carbonyls. The carbonyls largely investigated are those in a terminal environment (M-CO) and those in a bridging environment (M-CO-M). Terminal CO ligands appear at a higher wavenumber range (2130 - 1700 cm^{-1}) than the bridging CO ligands range (1900 - 1780 cm^{-1}). Terminal CO ligands may appear below 1900 cm^{-1} due to the severe reduction of the carbonyl strength through $d \rightarrow \pi^*$ bonding, while bridging CO ligands may appear above 1900 cm^{-1} due to the absence of electronic effects. [4]

A.3 Ultraviolet and Visible Spectroscopy

Ultraviolet-visible spectroscopy is used in the characterization of the absorption, transmission and reflectivity of compounds. The ultraviolet region of the electromagnetic spectrum is from a wavelength range of 200 to 400 nm while the visible region ranges from 400 to 800 nm. A spectrum is produced from transitions that involve electrons in the outer orbitals of atoms and molecules.

When radiation is passed through transparent matter, a portion of the radiation is likely to be absorbed. When this happens, the residual radiation is passed through a prism; this yields a spectrum known as the absorption spectrum. As a result of energy absorption, molecules pass from a state of low energy to that of a higher energy. In the case of ultraviolet and visible spectroscopy, the transitions that occur due to the absorption of electromagnetic radiation are transitions between electronic energy levels. When a molecule absorbs energy, an electron is promoted from the highest occupied molecular orbital (HOMO) to the lowest unoccupied molecular orbital (LUMO). [3]

[4] Stuart, B., *Infrared Spectroscopy: Fundamentals and Applications*, John Wiley & Sons, Ltd., 2004, 107.

A.3.1 Molecular Orbitals and Transitions

There is a difference in energy between these electronic states of many molecules. The lowest-energy occupied molecular orbitals are the sigma bonding (σ) orbitals which correspond to σ bonds. The pi bonding (π) orbitals lie at higher energy levels and the orbitals that have unshared pairs, nonbonding orbitals (n), lie at even higher energies. The orbitals of the highest energy are the unoccupied orbitals known as antibonding orbitals (π^* and σ^*). These orbitals are illustrated in Figure 3.

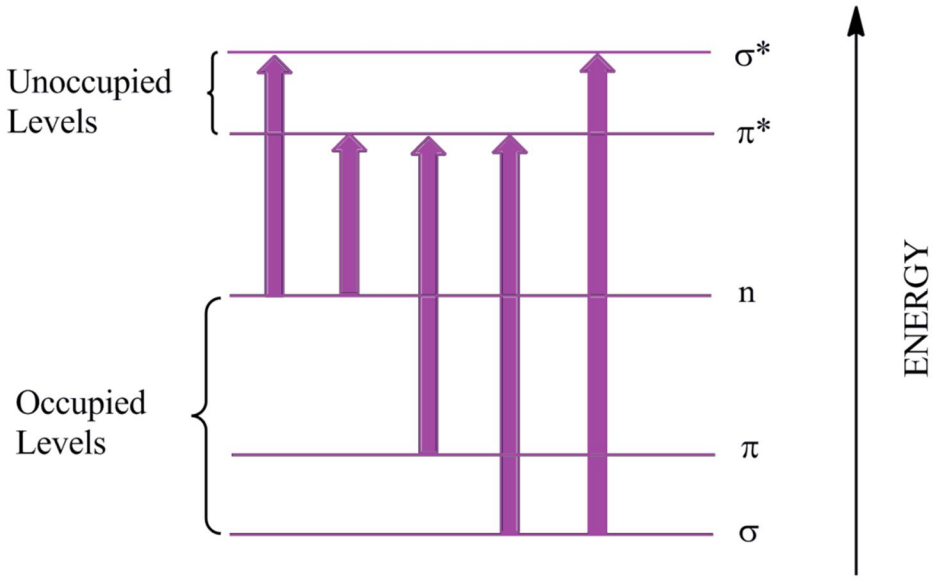

Figure 3: Diagram illustrating energy levels in ultraviolet-visible spectrocopy.

The transitions between these energy levels are as follows:

- Single bond molecules have transitions from σ which are at low energy levels to σ^* which are at high energy levels. When in the ground state, the σ orbital is occupied by a pair of electrons and the σ^* orbital is not occupied.
- Double bonded compounds contain π orbitals which are occupied by a pair of electrons and higher energy π^* which are not occupied in the ground state.
- The transitions of n to σ^* orbitals are observed when saturated compounds with lone pairs are involved. [5]

There are certain restrictions called selection rules that are considered with the transitions. The most important selection rule states that when transitions change the spin quantum number of an electron, they may not take place. These transitions are known as “forbidden” transitions. An example of a “forbidden” transition is the n to π^*

[5] Brown, S. B., *An Introduction to Spectroscopy for Biochemists*, Academic Press,1980, 17.

transition. These "forbidden" transitions have a lower intensity of the absorption than those allowed by the selection rule.

A.3.2 The Beer-Lambert Relationship

Beer's law states that the absorption of radiant energy is proportional to the total number of molecules in the light path. Lambert's law states that the proportion of radiant energy absorbed by a substance is independent of the intensity of the incident radiation. Generally, Beer's law describes the basic relationship between the value of the absorbance and the concentration of the absorbing substance. The amount of radiation absorbed by a substance is determined by the measurement of the difference in intensity between the incident radiation (I_0) on the sample and the transmitted radiation (I) from the sample.

The transmittance (T) is defined by:

$$T = \frac{I}{I_0} \qquad \text{(Eq. 3)}$$

The transmittance has a linear relationship with the absorbance (A) which is given by:

$$A = -\log T = log\ \frac{I_0}{I} \qquad \text{(Eq. 4)}$$

The Beer-Lambert law can be expressed as:

$$A = \varepsilon lc \qquad \text{(Eq. 5)}$$

where ε is the molar absorption coefficient for the substance, l is the light path in centimetres and c is the concentration of the sample.

The Beer-Lambert equation expresses a linear relationship between the recorded absorbance and the concentration of the sample.[6]

[6] Holme, D.J., Peck, H., *Analytical Biochemistry,* 2nd Ed., Longman Group UK Ltd. and John Wiley and Sons Inc, 1993, 41.

A.4 Nuclear Magnetic Resonance

Nuclear magnetic resonance (NMR) is a technique used by chemists to identify the structure of small molecules. In magnetic resonance, a quantum of energy from a radiofrequency is absorbed by a system that contains unpaired electron spins that are placed in a strong static magnetic field. In a nuclear magnetic resonance experiment, nuclei with a superimposed field B_1 are irradiated by inducing transitions between different energy levels. This condition is known as the resonance condition which allows the interaction between the magnetic component of the radiation and the nuclear dipoles.

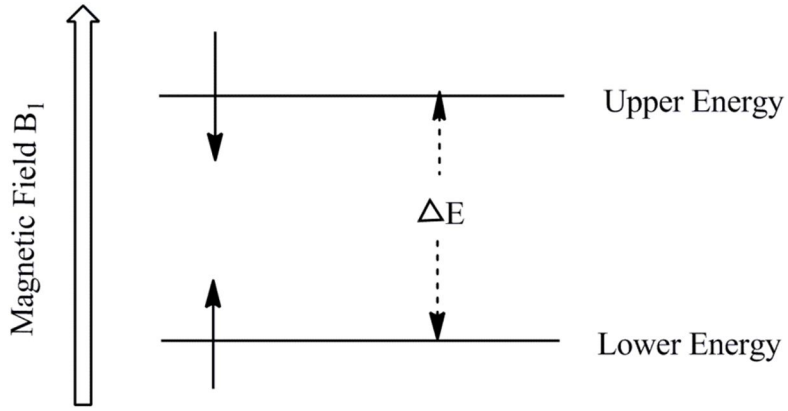

Figure 4: Diagram illustrating what occurs during an NMR experiment.

The transitions that occur from the lower to the upper energy level correspond to absorption of energy, while those in the reverse direction correspond to emission of energy. These transitions occur when the frequency of the electromagnetic radiation corresponds to the Larmor frequency (Figure 4).

When the lower energy level has an excess of the number of nuclei, the absorption of energy from the irradiating field is dominant and a signal is observed. When the population of nuclei in the lower level is equal to the upper level, no signal is observed. This is known as saturation.[7]

A.4.1 Chemical Shifts

During an NMR experiment, an internal standard is added to the sample being examined. In ^{1}H and ^{13}C NMR spectroscopy the internal standard used is tetramethylsilane (TMS). TMS is a suitable choice because it contains twelve

[7] Friebolin, H., *Basic One- and Two-Dimensional NMR Spectroscopy,* 4th Ed., Wiley-VCH, 2005, 7.

equivalent, highly shielded protons. Only a small amount is needed and it gives one single sharp peak which is clearly separated from other resonances.

The position in which a peak appears on the spectrum is specified by measuring its frequency separation from the reference peak, and this difference is divided by the frequency of the reference peak. The chemical shift, δ, is given by:

$$\delta(ppm) = 10^6 \times \frac{\nu - \nu_{ref}}{\nu_{ref}} \qquad \text{(Eq. 6)}$$

where ν is the frequency of the NMR is line and ν_{ref} is the frequency of the internal standard.[8] The frequency at which the protons resonate differs. When a magnetic field is applied and a tiny electric current is set up, the electrons that surround a nucleus will oppose the magnetic field that is applied and this is known as "shielding". The electron distribution differs for all atoms so the more electronegative it is the less shielded it is and has a higher chemical shift.[9]

A.4.2 Spin-Spin coupling and its effect on NMR Spectra

Nuclear spin-spin coupling is a phenomenon that causes NMR lines to split with characteristic relative intensities and spacings. This phenomenon arises because the hydrogens on adjacent carbon atoms can act as if they "sense" one another. The general *n* + 1 rule is applied in which protons that have *n* equivalent neighbouring protons show *n* + 1 peaks in their NMR peaks. The magnetic moment of the ^{13}C nucleus is what splits the ^{1}H resonance into two. The magnetic field direction is determined by the ^{13}C magnetic quantum number.

- When m = $+\frac{1}{2}$, the ^{1}H resonance is shifted to a lower frequency since the magnetic field opposes the external field. This means the proton is shielded.
- When m = $-\frac{1}{2}$, the resonance is shifted to a higher frequency since the magnetic field adds to the external field. This means the proton is deshielded.[10]

The degree to which the NMR lines split is known as the coupling constant and represented as *J* in Hz. The size of the coupling constant is determined by the bond distance between the protons, the angle between the C-H bonds and electronegative

[8] Keeler, J., *Understanding NMR Spectroscopy*, John Wiley & Sons Ltd, 2005, 6.
[9] Clayden, J., Greeves, N., Warren, S., *Organic Chemistry,* 1st Ed, Oxford University Press, 2000.
[10] Hore, P.J., *Nuclear Magnetic Resonance*, Oxford University Press, 1995, 22, 259.

substituents. The coupling constant may either be positive or negative and depends on the arrangement of nuclear spins.

A.5 Chemical Kinetics

Chemical kinetics is a study that deals with the rates of chemical reactions. The study can be used to get information about the stability of a component and how feasible it is to prepare it in the laboratory. Kinetics studies are used to understand the reaction mechanisms of simple and complex reactions that could involve only one step or several consecutive steps. A reaction mechanism is what defines the progress of events from reactants to products. It indicates whether the chemical reactions progress by a single molecular process or by several.[11]

A.5.1 The Rate of the Reaction

The rate of a chemical reaction in a closed constant-volume system can be defined as the rate of change of the concentration of any of the reactants or products with time. The general chemical reaction is considered:

$$aA + bB \rightarrow cC + dD \qquad \text{(Eq. 7)}$$

From Equation 7 the unique rate of reaction can be defined as:

$$R = -\frac{1}{a}\frac{dA}{dt} = -\frac{1}{b}\frac{dB}{dt} = \frac{1}{c}\frac{dC}{dt} = \frac{1}{d}\frac{dD}{dt} \qquad \text{(Eq. 8)}$$

Equation 8 shows the decrease in concentration with time for components A and B, which is defined by the term $-d[A]/dt$ and $-d[B]/dt$. There is an increase in concentration with time for components C and D and they are defined as $d[C]/dt$ and $d[D]/dt$. This is known as the rate of reaction which is the same for all reactants and products.[12]

A.5.2 The Rate Law

The rate law can be expressed as follows:

$$Rate = k[A]^x[B]^y \qquad \text{(Eq. 9)}$$

[11] Espenson, J. H., *Chemical Kinetics and Reaction Mechanisms*, McGraw-Hill, 1981, 1.
[12] Laidler, K.J., Meiser, J.H., Sanctuary, B.C., *Physical Chemistry*, Houghton Mifflin Company, 2003, 363.

This is expressed by a constant multiplied by some function of concentrations. The exponents *x* and *y* are called the order of the reaction in terms of *A* and *B* while *k* symbolises the rate constant. The rate law is important because it comprises of the concentrations of the necessary species to get from the reactant to the product by the lowest energy pathway. An acceptable mechanism must predict a rate law that is consistent with the experimental rate law.[13]

A.5.3 The *Pseudo*-First Order Reaction

In *pseudo*-first order conditions, the monitored concentration of the reactants is made smaller than that of the other reactants; as a result these concentrations remain constant during the reaction. If the conditions for Equation 6 have been set as:

$$[B] >> [A] \qquad \text{(Eq. 10)}$$

Then the rate equation is stated as:

$$Rate = k_{obs}[A]^m \; and \; then \; k_{obs} = k[B]^n \qquad \text{(Eq. 11)}$$

k_{obs} is the observed *pseudo*-first order rate constant. When the concentration of B is varied, the rate constant *k* can be determined. The second order system can be described by:

$$a[A] + b[B] \rightleftarrows m[M] \qquad \text{(Eq. 12)}$$

and the rate law as:

$$Rate = k_1[A][B] + k_2[A] \qquad \text{(Eq. 13)}$$

For *pseudo*-first order conditions, k_{obs} is then given as:

$$k_{obs} = k_1[B] + k_2 \qquad \text{(Eq. 14)}$$

[13] House, J. E., *Principles of Chemical Kinetics*, Times Higher Education Group, 1997, 2.

where k_1 represents the forward reaction and k_2 represents the reverse reaction. The equilibrium constant can be represented as:

$$K_{eq} = \frac{k_1}{k_2} \quad \text{(Eq. 15)}$$

Intergration of the initial rate equation from t = 0 to t gives the equation:

$$ln\frac{[C]t}{[C]_0} = k_{obs} \quad \text{(Eq. 16)}$$

Here $[C]_t$ and $[C]_0$ represent the change in concentration of the reactant at time = *t* and *0* respectively. The concentration of a solution can be related to the absorbance and therefore the Beer-Lambert law can be used in chemical kinetics. Absorbance can be given by:

$$A_t = A_\infty - (A_\infty - A_0)e^{k_{obs}t} \quad \text{(Eq. 17)}$$

The absorbance after time t is expressed by A_t and at infinite time A_∞. Equation 17 is used in a least-square fit to determine the observed rate constant.

A.6 X-Ray Diffraction

Crystallography is the study of the arrangement of component atoms in a crystal. Many physical and chemical properties are dependent on the crystal structure. X-ray diffraction was later discovered in which a single crystal is mounted in a beam of X-rays. A suitable crystal with dimensions of round about 0.1 × 0.1× 0.1 mm must be used so it is possible to put it in the primary X-ray beam for analysis. A plane of atoms in the crystal is what gives rise to the narrow diffracted beam. The beam is recorded as well as the intensity of each spot. The resulting data set gives the position, intensity and *hkl* index from where it is converted into an electron density map. The Miller Indices (*hkl*) specify the internal planes through a crystal structure. The first analysis by single-crystal X-ray diffraction was performed by W.L. Bragg in 1913 which proved that a zinc blend had a face-centered cubic structure.[14]

[14] Tilley, R., *Crystals and crystal structures*, John Wiley & Sons, Ltd, 2006, 5.

A.6.1 Bragg's Law

In 1913 W.L. Bragg showed that a distribution of scattered radiation by an angle could be understood if the diffracted beams were considered to behave as if they were reflected from planes passing through points of the crystal lattice. Bragg derived the following equation:

$$n\lambda = 2dsin\theta \qquad \text{(Eq. 18)}$$

where λ is the wavelength of the radiation, n is an integer, d is the interplanar spacing between the lattice planes in the crystal and θ is the Bragg angle of incidence of the X-ray beam (Figure 5).

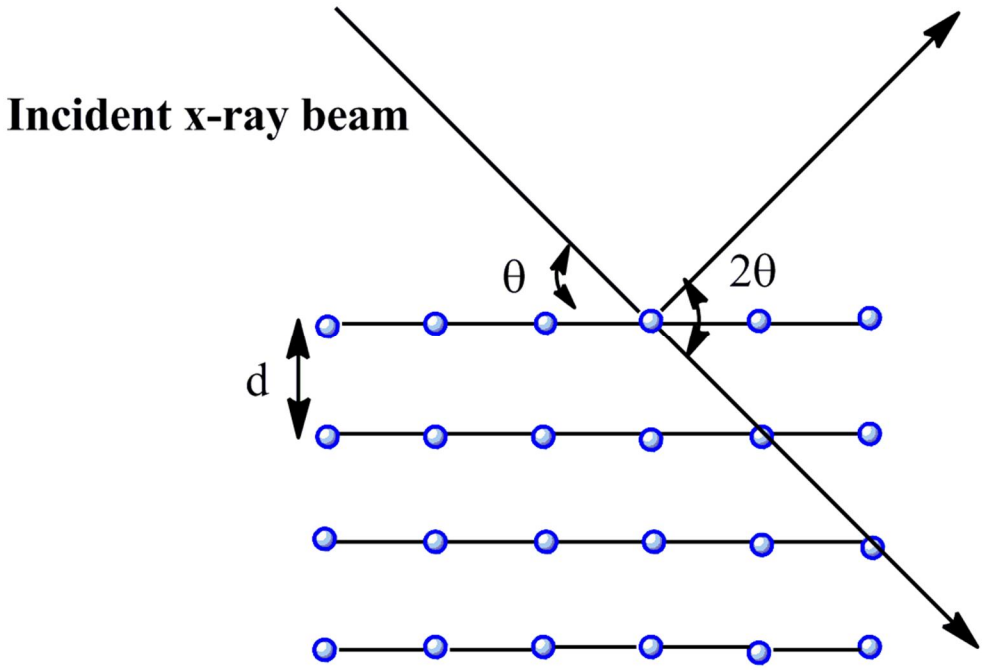

Figure 5: Diagram illustrating X-ray diffraction according to Bragg's law.

Bragg's equation can be derived by considering that the path difference between the scattered waves from adjacent parallel lattice planes is an integral number of wavelengths. The diffraction maxima are observed only when there is an appropriate relation between the wavelength, interplanar spacing and angle of incidence. The directed beams are commonly known as 'reflections' because it appears as if the

reflection occurred from the lattices, with a direct beam that deviated by an angle *2θ* from its original direction. [15]

A.6.2 The Structure Factor

The structure factor *F (hkl)* is an expression of the combined scattering of X-rays for all atoms in the unit cell compared to that of a single electron. The amplitude |*F(hkl)*| is measured in electrons. For a combined scattered wave from the (*hkl*) planes, the components that are required are g_j and Φ_j. The resultant wave for the unit cell is therefore given as

$$Fhkl = \sum_{j=1}^{N} g_j \exp(i\phi_j) = \sum_{j=1}^{N} g_j \exp[(hx_j + ky_j + lz_j)] \quad \text{(Eq. 19)}$$

where g_j is known as the atomic scattering factor. The above equation shows that the structure factor magnitude depends only on the relative disposition of the N atoms in the unit cell and their respective scattering powers g_j. Equation 16 is also considered to represent a wavelet having an amplitude |*F(hkl)*| and a phase $Q_j = 2\pi (hx_j + ky_j + lz_j)$ which is used to express the pathlength for each scattered wavelet. The structure factor is simply the result of the wavelets scattered by the N atoms in a unit cell. The structure factor can be expressed as:

$$F(hkl) = A'(hkl) + iB'(hkl) \quad \text{(Eq. 20)}$$

$$A'(hkl) = \sum_{j=1}^{N} g_j \cos 2\pi(hx_j + ky_j + lz_j) \quad \text{(Eq. 21)}$$

$$B'(hkl) = \sum_{j=1}^{N} g_j \sin 2\pi(hx_j + ky_j + lz_j) \quad \text{(Eq. 22)}$$

Therefore :

$$F(hkl) = \sum_{j=1}^{N} g_j \cos 2\pi(hx_j + ky_j + lz_j) + i \sin 2\pi(hx_j + ky_j + lz_j) \quad \text{(Eq. 23)}$$

[15] Glusker, J. P., Trueblood, K. N., *Crystal Structure Analysis*, Oxford University Press, 1972, 32.

A.6.2.1 Ideal Intensity

The square of the amplitude of the wave is directly proportional to the energy associated with a cosine wave. This is expressed in terms of the intensity of the scattered wave from the unit cell as $I_o(hkl)$ where *o* represents an experimentally observed quantity. The symbol $I_o(hkl)$ may be used to represent $|F(hkl)|^2$ which is called the ideal intensity.[16] Therefore:

$$I_o(hkl) \alpha \, |F(hkl)|^2 \qquad \text{(Eq. 24)}$$

A.6.3 The Phase Problem

When the structure factor amplitude $|F(hkl)|$ and the phase angles are known, the electron density distribution of the unit cell can be calculated. The electron density can then be used to obtain the structure factors. The only difficulty here is that the data contains only the structure factor amplitudes and not their phase angles and this is what is known as the Phase Problem. Methods have been derived to solve the Phase Problem namely: The Patterson's function and the Direct Method.

A.6.4 Methods of Solving the Phase Problem

- **Direct Method**

A very important technique in the solving of the Phase Problem is the Direct Method. It has the ability to yield good phase information for structures containing no heavy atoms. A common feature of this structure-determining method is that the values for the phases of x-ray reflections are derived initially by structure factor calculations on only parts of the structure.

- **The Patterson's Function**

In 1935 Patterson published a paper that indicated how useful the phaseless quantities $|F|^2$ from the Fourier calculation are. He showed that where the usual synthesis with *F*'s as coefficients showed the distribution of atoms in the cell and that the calculated $|F|^2$ had peaks corresponding to all the interatomic vectors. Patterson recognised that because of the high degree of order in the crystal, the averaging overall directions could

[16] Ladd, M.F.C., Palmer, R.A., *Structure Determination by X-Ray Crystallography*, Plenum Press, 1993, 198.

be eliminated and detailed information about both the magnitudes and the directions of the interatomic vectors could be obtained.[17]

Thus a peak at the *UVW* in a Patterson's map indicates that there exists an atom in the crystal atoms at $x_1; y_1; z_1$ and at $x_2; y_2; z_2$ such that:

$$u = x_1 - x_2$$

$$v = y_1 - y_2$$

$$w = z_1 - z_2$$

A one-dimensional electron density distribution map, *p(X)* for a regularly repeating cell, length *a*, can be expressed by:

$$P(X) = \frac{1}{a}\sum_{all} F(h)\exp(-2\pi i h X) \qquad \text{(Eq. 25)}$$

And extended to three dimensions as:

$$P(UVW) = \frac{1}{V_c}\sum_h \sum_k \sum_l |F(hkl)|^2 \exp[2\pi i(hU + kV + lW)] \qquad \text{(Eq. 26)}$$

- **Least-Square Refinement**

Another important part of determining the atomic coordinates of a unit cell is assessing the correctness of the resulting structure. When the atomic coordinates in the proposed structure correlate with that in the crystal then the calculated and observed structure-factor magnitudes should be the same. These are expressed as $|F_c|$ and $|F_o|$ respectively. The difference between them, $||F_c| - |F_o||$, represents the order of the agreement and the if the proposed model is incorrect.

$$R = \frac{\sum ||Fc| - |Fo||}{\sum |Fo|} \qquad \text{(Eq. 27)}$$

where *R* is known as the R-factor for a set of structure-factor magnitudes. When $R < 0.50$ it suggests that the structure is correct, although smaller *R* values are needed for credibility.[18]

[17] Stout, G. H., Jensen, L. H., *X-Ray Structure Determination: a Practical Guide*, The MacMillan Company, 1968, 270.
[18] Azároff, L.V. *Elements of X-Ray Crystallography*, McGraw-Hill, 1968, 323.

APPENDIX B

Table B.1: Atomic coordinates (x 10^4) and equivalent isotropic displacement parameters ($Å^2$ x 10^3) for *fac*-[Re(Phen)$(CO)_3(H_2O)][CF_3SO_3]$. U(eq) is defined as one third of the trace of the orthogonalized U^{ij} tensor.

	x	y	z	U(eq)
Mn(01)	1263(1)	2915(1)	3696(1)	18(1)
S(1)	3537(1)	5484(1)	6203(1)	30(1)
F(1)	5535(2)	3686(2)	6879(1)	36(1)
N(01)	3076(2)	2083(2)	4630(1)	18(1)
C(01)	1803(3)	2275(2)	3036(1)	26(1)
F(2)	4555(2)	4376(2)	7534(1)	41(1)
N(02)	292(2)	1227(2)	3731(1)	20(1)
O(04)	01(2)	3484(2)	4511(1)	24(1)
C(013)	5229(3)	719(2)	5909(1)	23(1)
F(3)	3279(2)	3140(2)	6555(1)	47(1)
O(2)	3123(2)	4995(2)	5450(1)	37(1)
C(015)	2727(2)	942(2)	4829(1)	18(1)
O(02)	-1388(2)	3948(2)	2310(1)	37(1)
O(03)	2689(2)	5390(2)	3742(1)	35(1)
O(01)	2090(2)	1858(2)	1858(2)	41(1)
O(3)	2261(2)	5867(3)	6269(1)	57(1)
C(03)	2192(3)	4422(2)	3747(1)	24(1)
O(1)	4807(2)	6338(2)	6527(1)	44(1)
C(016)	3289(3)	-971(2)	5614(1)	24(1)
C(018)	804(3)	-712(2)	4485(1)	24(1)
C(019)	1230(2)	479(2)	4338(1)	18(1)
C(011)	4484(2)	2512(2)	5057(1)	22(1)
C(02)	-405(3)	3547(2)	2867(1)	25(1)
C(014)	3759(3)	229(2)	5463(1)	20(1)
C(012)	5583(3)	1852(2)	5696(1)	24(1)
C(1)	4254(3)	4096(3)	6826(1)	27(1)
C(017)	1875(3)	-1417(2)	5139(1)	27(1)
C(022)	-1095(3)	793(2)	3254(1)	25(1)
C(020)	-665(3)	-1137(2)	3960(2)	29(1)
C(021)	-1607(3)	-386(2)	3351(2)	29(1)

Table B.2: Bond distances (Å) and angles (°) for *fac*-[Re(Phen)$(CO)_3(H_2O)][CF_3SO_3]$.

Bond	Bond Distance	Bond Angle	Angle
Mn(01)-C(01)	1.801(2)	C(01)-Mn(01)-C(02)	87.42(11)
Mn(01)-C(02)	1.811(3)	C(01)-Mn(01)-C(03)	91.33(11)
Mn(01)-C(03)	1.823(3)	C(02)-Mn(01)-C(03)	87.52(11)
Mn(01)-N(02)	2.051(2)	C(01)-Mn(01)-N(02)	91.90(10)
Mn(01)-N(01)	2.0578(19)	C(02)-Mn(01)-N(02)	95.71(10)
Mn(01)-O(04)	2.0731(17)	C(03)-Mn(01)-N(02)	175.53(9)
S(1)-O(3)	1.433(2)	C(01)-Mn(01)-N(01)	92.49(10)
S(1)-O(1)	1.438(2)	C(02)-Mn(01)-N(01)	176.04(9)
S(1)-O(2)	1.4438(19)	C(03)-Mn(01)-N(01)	96.44(9)
S(1)-C(1)	1.820(3)	N(02)-Mn(01)-N(01)	80.33(8)
F(1)-C(1)	1.332(3)	C(01)-Mn(01)-O(04)	174.50(9)
N(01)-C(011)	1.332(3)	C(02)-Mn(01)-O(04)	96.52(9)

N(01)-C(015)	1.367(3)	C(03)-Mn(01)-O(04)	92.68(9)
C(01)-O(01)	1.138(3)	N(02)-Mn(01)-O(04)	83.91(7)
F(2)-C(1)	1.328(3)	N(01)-Mn(01)-O(04)	83.31(8)
N(02)-C(022)	1.333(3)	O(3)-S(1)-O(1)	116.03(15)
N(02)-C(019)	1.362(3)	O(3)-S(1)-O(2)	113.11(13)
O(04)-H(1A)	0.859(17)	O(1)-S(1)-O(2)	114.97(13)
O(04)-H(1B)	0.861(18)	O(3)-S(1)-C(1)	103.54(14)
C(013)-C(012)	1.373(3)	O(1)-S(1)-C(1)	103.17(12)
C(013)-C(014)	1.406(3)	O(2)-S(1)-C(1)	103.88(12)
C(013)-H(013)	0.9300	C(011)-N(01)-C(015)	117.68(19)
F(3)-C(1)	1.326(3)	C(011)-N(01)-Mn(01)	129.26(16)
C(015)-C(014)	1.397(3)	C(015)-N(01)-Mn(01)	113.04(14)
C(015)-C(019)	1.428(3)	O(01)-C(01)-Mn(01)	177.5(2)
O(02)-C(02)	1.146(3)	C(022)-N(02)-C(019)	117.7(2)
O(03)-C(03)	1.140(3)	C(022)-N(02)-Mn(01)	129.09(17)
C(016)-C(017)	1.355(3)	C(019)-N(02)-Mn(01)	113.21(14)
C(016)-C(014)	1.435(3)	Mn(01)-O(04)-H(1A)	117(2)
C(016)-H(016)	0.9300	Mn(01)-O(04)-H(1B)	114(2)
C(018)-C(019)	1.404(3)	H(1A)-O(04)-H(1B)	103(2)
C(018)-C(020)	1.407(3)	C(012)-C(013)-C(014)	118.9(2)
C(018)-C(017)	1.427(3)	C(012)-C(013)-H(013)	120.5
C(011)-C(012)	1.396(3)	C(014)-C(013)-H(013)	120.5
C(011)-H(011)	0.9300	N(01)-C(015)-C(014)	123.3(2)
C(012)-H(012)	0.9300	N(01)-C(015)-C(019)	116.36(19)
C(017)-H(017)	0.9300	C(014)-C(015)-C(019)	120.3(2)
C(022)-C(021)	1.396(4)	O(03)-C(03)-Mn(01)	175.8(2)
C(022)-H(022)	0.9300	C(017)-C(016)-C(014)	120.5(2)
C(020)-C(021)	1.367(4)	C(017)-C(016)-H(016)	119.7
C(020)-H(020)	0.9300	C(014)-C(016)-H(016)	119.7
C(021)-H(021)	0.9300	C(019)-C(018)-C(020)	117.0(2)
		C(019)-C(018)-C(017)	118.7(2)
		C(020)-C(018)-C(017)	124.3(2)
		N(02)-C(019)-C(018)	123.3(2)
		N(02)-C(019)-C(015)	116.8(2)
		C(018)-C(019)-C(015)	119.8(2)
		N(01)-C(011)-C(012)	122.5(2)
		N(01)-C(011)-H(011)	118.8
		C(012)-C(011)-H(011)	118.8
		O(02)-C(02)-Mn(01)	173.9(2)
		C(015)-C(014)-C(013)	117.6(2)
		C(015)-C(014)-C(016)	118.9(2)
		C(013)-C(014)-C(016)	123.5(2)
		C(013)-C(012)-C(011)	120.0(2)
		C(013)-C(012)-H(012)	120.0
		C(011)-C(012)-H(012)	120.0
		F(3)-C(1)-F(2)	109.4(2)
		F(3)-C(1)-F(1)	107.1(2)
		F(2)-C(1)-F(1)	107.1(2)
		F(3)-C(1)-S(1)	111.38(17)
		F(2)-C(1)-S(1)	110.85(18)
		F(1)-C(1)-S(1)	110.84(16)
		C(016)-C(017)-C(018)	121.6(2)
		C(016)-C(017)-H(017)	119.2
		C(018)-C(017)-H(017)	119.2
		N(02)-C(022)-C(021)	122.8(2)

		N(02)-C(022)-H(022)	118.6
		C(021)-C(022)-H(022)	118.6
		C(021)-C(020)-C(018)	119.7(2)
		C(021)-C(020)-H(020)	120.2
		C(018)-C(020)-H(020)	120.2
		C(020)-C(021)-C(022)	119.5(2)
		C(020)-C(021)-H(021)	120.3
		C(022)-C(021)-H(021)	120.3

Table B.3: Anisotropic displacement parameters ($Å^2$ x 10^3) for *fac*-[Re(Phen)$(CO)_3(H_2O)][CF_3SO_3]$. The Anisotropic displacement factor exponent takes the form: $-2\pi^2(h2a^{*2}U^{11} + ... + 2hka^*b^*U^{12})$.

	U11	U22	U33	U23	U13	U12
Mn(01)	15(1)	18(1)	20(1)	2(1)	8(1)	1(1)
S(1)	27(1)	34(1)	27(1)	0(1)	10(1)	7(1)
F(1)	27(1)	38(1)	41(1)	3(1)	16(1)	5(1)
N(01)	15(1)	18(1)	21(1)	-1(1)	9(1)	-1(1)
C(01)	27(1)	22(1)	30(1)	6(1)	15(1)	5(1)
F(2)	40(1)	61(1)	23(1)	-2(1)	16(1)	-6(1)
N(02)	15(1)	21(1)	23(1)	-2(1)	9(1)	-1(1)
O(04)	21(1)	26(1)	26(1)	-3(1)	12(1)	0(1)
C(013)	22(1)	24(1)	19(1)	-1(1)	6(1)	4(1)
F(3)	43(1)	51(1)	41(1)	-3(1)	18(1)	-26(1)
O(2)	39(1)	44(1)	24(1)	0(1)	12(1)	-2(1)
C(015)	19(1)	18(1)	19(1)	-2(1)	11(1)	-1(1)
O(02)	29(1)	36(1)	31(1)	5(1)	3(1)	6(1)
O(03)	42(1)	25(1)	42(1)	0(1)	25(1)	-9(1)
O(01)	60(1)	34(1)	48(1)	3(1)	41(1)	8(1)
O(3)	35(1)	89(2)	47(1)	5(1)	19(1)	26(1)
C(03)	21(1)	27(1)	24(1)	2(1)	12(1)	2(1)
O(1)	44(1)	26(1)	49(1)	0(1)	13(1)	-3(1)
C(016)	31(1)	20(1)	23(1)	2(1)	14(1)	1(1)
C(018)	24(1)	22(1)	30(1)	-3(1)	17(1)	-3(1)
C(019)	17(1)	18(1)	21(1)	-3(1)	11(1)	-2(1)
C(011)	17(1)	19(1)	29(1)	-1(1)	10(1)	-2(1)
C(02)	22(1)	23(1)	29(1)	-1(1)	12(1)	0(1)
C(014)	22(1)	20(1)	20(1)	-1(1)	12(1)	1(1)
C(012)	15(1)	25(1)	26(1)	-5(1)	6(1)	-2(1)
C(1)	22(1)	35(2)	26(1)	-3(1)	12(1)	-7(1)
C(017)	34(1)	20(1)	31(1)	1(1)	19(1)	-4(1)
C(022)	16(1)	28(1)	26(1)	-5(1)	7(1)	-3(1)
C(020)	25(1)	23(1)	40(1)	-6(1)	18(1)	-7(1)
C(021)	19(1)	30(1)	35(1)	-9(1)	11(1)	-8(1)

Table B.4: Hydrogen coordinates (x 10^4) and isotropic displacement parameters ($Å^2$ x 10^3) for *fac*-[Re(Phen)$(CO)_3(H_2O)][CF_3SO_3]$.

	x	y	z	U(eq)
H(013)	5950	283	6341	28
H(016)	3960	-1447	6040	29
H(011)	4744	3279	4924	26
H(012)	6556	2180	5979	29
H(017)	1597	-2201	5244	33
H(022)	-1750	1298	2840	30
H(020)	-995	-1925	4029	34

H(021)	-2580	-658	3003	35
H(1A)	-160(20)	3840(30)	4342(19)	68(12)
H(1B)	1320(30)	4030(30)	4836(18)	79(13)

Table B.5: Torsion angles (°) for *fac*-[Re(Phen)(CO)$_3$(H$_2$O)][CF$_3$SO$_3$].

Torsion Angle	Angle	Torsion Angle	Angle
C(01)-Mn(01)-N(01)-C(011)	85.8(2)	C(02)-Mn(01)-N(01)-C(011)	174.4(13)
N(02)-Mn(01)-N(01)-C(011)	177.3(2)	O(04)-Mn(01)-N(01)-C(011)	-97.8(2)
C(01)-Mn(01)-N(01)-C(015)	-95.67(16)	C(02)-Mn(01)-N(01)-C(015)	-7.0(14)
C(03)-Mn(01)-N(01)-C(015)	172.71(15)	N(02)-Mn(01)-N(01)-C(015)	-4.17(14)
O(04)-Mn(01)-N(01)-C(015)	80.76(15)	C(02)-Mn(01)-C(01)-O(01)	-42(5)
C(03)-Mn(01)-C(01)-O(01)	-129(5)	N(02)-Mn(01)-C(01)-O(01)	54(5)
N(01)-Mn(01)-C(01)-O(01)	134(5)	O(04)-Mn(01)-C(01)-O(01)	94(5)
C(01)-Mn(01)-N(02)-C(022)	-84.9(2)	C(02)-Mn(01)-N(02)-C(022)	2.7(2)
C(03)-Mn(01)-N(02)-C(022)	139.0(11)	N(01)-Mn(01)-N(02)-C(022)	-177.1(2)
O(04)-Mn(01)-N(02)-C(022)	98.7(2)	C(01)-Mn(01)-N(02)-C(019)	95.78(16)
C(02)-Mn(01)-N(02)-C(019)	-176.62(15)	C(03)-Mn(01)-N(02)-C(019)	-40.3(12)
N(01)-Mn(01)-N(02)-C(019)	3.58(14)	O(04)-Mn(01)-N(02)-C(019)	-80.65(15)
C(011)-N(01)-C(015)-C(014)	1.5(3)	Mn(01)-N(01)-C(015)-C(014)	-177.21(16)
C(011)-N(01)-C(015)-C(019)	-177.1(2)	Mn(01)-N(01)-C(015)-C(019)	4.1(2)
C(01)-Mn(01)-C(03)-O(03)	92(3)	C(02)-Mn(01)-C(03)-O(03)	5(3)
N(02)-Mn(01)-C(03)-O(03)	-132(3)	N(01)-Mn(01)-C(03)-O(03)	-175(3)
O(04)-Mn(01)-C(03)-O(03)	-92(3)	C(022)-N(02)-C(019)-C(018)	-0.2(3)
Mn(01)-N(02)-C(019)-C(018)	179.21(17)	C(022)-N(02)-C(019)-C(015)	178.1(2)
Mn(01)-N(02)-C(019)-C(015)	-2.5(2)	C(020)-C(018)-C(019)-N(02)	1.0(3)
C(017)-C(018)-C(019)-N(02)	-179.8(2)	C(020)-C(018)-C(019)-C(015)	-177.3(2)
C(017)-C(018)-C(019)-C(015)	1.9(3)	N(01)-C(015)-C(019)-N(02)	-1.1(3)
C(014)-C(015)-C(019)-N(02)	-179.83(19)	N(01)-C(015)-C(019)-C(018)	177.24(19)
C(014)-C(015)-C(019)-C(018)	-1.4(3)	C(015)-N(01)-C(011)-C(012)	-1.1(3)
Mn(01)-N(01)-C(011)-C(012)	177.44(17)	C(01)-Mn(01)-C(02)-O(02)	-26(2)
C(03)-Mn(01)-C(02)-O(02)	65(2)	N(02)-Mn(01)-C(02)-O(02)	-118(2)
N(01)-Mn(01)-C(02)-O(02)	-115(2)	O(04)-Mn(01)-C(02)-O(02)	157(2)
N(01)-C(015)-C(014)-C(013)	-0.5(3)	C(019)-C(015)-C(014)-C(013)	178.0(2)
N(01)-C(015)-C(014)-C(016)	-178.7(2)	C(019)-C(015)-C(014)-C(016)	-0.1(3)
C(012)-C(013)-C(014)-C(015)	-0.9(3)	C(012)-C(013)-C(014)-C(016)	177.2(2)
C(017)-C(016)-C(014)-C(015)	1.2(3)	C(017)-C(016)-C(014)-C(013)	-176.8(2)
C(014)-C(013)-C(012)-C(011)	1.4(3)	N(01)-C(011)-C(012)-C(013)	-0.4(4)
O(3)-S(1)-C(1)-F(3)	66.2(2)	O(1)-S(1)-C(1)-F(3)	-172.51(18)
O(2)-S(1)-C(1)-F(3)	-52.2(2)	O(3)-S(1)-C(1)-F(2)	-55.8(2)
O(1)-S(1)-C(1)-F(2)	65.48(19)	O(2)-S(1)-C(1)-F(2)	-174.23(16)
O(3)-S(1)-C(1)-F(1)	-174.68(18)	O(1)-S(1)-C(1)-F(1)	-53.4(2)
O(2)-S(1)-C(1)-F(1)	66.94(19)	C(014)-C(016)-C(017)-C(018)	-0.7(4)
C(019)-C(018)-C(017)-C(016)	-0.8(4)	C(020)-C(018)-C(017)-C(016)	178.3(2)
C(019)-N(02)-C(022)-C(021)	-0.6(3)	Mn(01)-N(02)-C(022)-C(021)	-179.91(17)
C(019)-C(018)-C(020)-C(021)	-0.9(3)	C(017)-C(018)-C(020)-C(021)	179.9(2)
C(018)-C(020)-C(021)-C(022)	0.2(4)	N(02)-C(022)-C(021)-C(020)	0.6(4)
C(03)-Mn(01)-N(01)-C(011)	-5.9(2)		

Table B.6: Hydrogen bond distances (Å) and angles (°) for *fac*-[Re(Phen)(CO)$_3$(H$_2$O)][CF$_3$SO$_3$].

D-H…A	d (D-H)	d (H…A)	d (D…A)	D-H…A angle
O(04)-H(1A)...O(3)#1	0.859(17)	1.887(19)	2.709(3)	160(3)
O(04)-H(1B)...O(2)	0.861(18)	1.917(19)	2.745(3)	161(3)
C(013)-H(013)...O(02)#2	0.93	2.56	3.203(3)	126.7

C(016)-H(016)...O(1)#3	0.93	2.51	3.305(3)	144.1
C(022)-H(022)...F(1)#4	0.93	2.46	3.205(3)	136.9
C(020)-H(020)...F(3)#5	0.93	2.39	3.143(3)	137.8

Symmetry codes, transformations used to generate equivalent atoms:
#1 -x,-y+1,-z+1 #2 x+1,-y+1/2,z+1/2 #3 x,y-1,z #4 x-1,-y+1/2,z-1/2 #5 -x,-y,-z+1

Table B.7: Atomic coordinates (x 10^4) and equivalent isotropic displacement parameters (Å^2 x 10^3) for *fac*-[Re(Bipy)$(CO)_3(H_2O)$][CF_3SO_3]. U(eq) is defined as one third of the trace of the orthogonalized U^{ij} tensor.

	x	y	z	U(eq)
Mn(01)	6114(1)	2755(1)	8632(1)	21(1)
O(04)	5725(5)	3509(4)	9495(2)	38(1)
N(01)	7918(4)	1966(4)	9565(2)	22(1)
O(02)	7219(6)	5479(4)	8490(2)	56(1)
N(02)	5315(4)	954(4)	8812(2)	23(1)
O(01)	6885(6)	1571(5)	7513(3)	61(1)
C(016)	6264(4)	177(4)	9422(2)	22(1)
C(017)	5866(5)	-1086(5)	9599(3)	27(1)
C(013)	10172(5)	781(5)	10890(3)	31(1)
C(015)	7718(4)	771(4)	9862(2)	21(1)
C(020)	3948(5)	510(5)	8396(3)	30(1)
C(019)	3491(5)	-735(5)	8547(3)	31(1)
C(02)	6850(6)	4411(5)	8566(3)	34(1)
C(03)	4448(5)	3296(5)	7792(3)	36(1)
C(01)	6590(6)	2013(5)	7955(3)	33(1)
C(014)	8826(5)	168(5)	10532(2)	26(1)
C(018)	4466(5)	-1548(5)	9150(3)	31(1)
C(011)	9235(5)	2536(5)	9913(3)	28(1)
C(012)	10386(5)	1976(5)	10571(3)	31(1)
O(03)	3449(4)	3611(4)	7223(3)	57(1)
S(1)	11790(3)	839(2)	13956(1)	67(1)
C(1)	10711(6)	-380(6)	13209(3)	35(1)
F(3)	9435(9)	-17(13)	13118(7)	76(4)
F(5)	10331(8)	-104(15)	12469(7)	32(2)
F(2)	10954(11)	-1627(11)	13381(8)	42(2)
O(5)	12521(13)	1559(12)	13752(5)	66(1)
O(4)	11662(10)	2170(8)	13753(5)	38(1)
F(4)	9484(10)	-877(13)	13140(5)	68(3)
F(6)	10820(20)	-11(19)	12595(9)	104(6)
F(1)	11572(14)	-1536(14)	13399(8)	80(4)
O(1)	10352(11)	1850(11)	13627(9)	100(4)
O(3)	13249(11)	296(11)	14057(9)	100(4)
O(2)	11868(6)	363(5)	14634(2)	66(1)

Table B.8: Bond distances (Å) and angles (°) for *fac*-[Re(Bipy)$(CO)_3(H_2O)$][CF_3SO_3].

Bond	Bond Distance	Bond Angle	Angle
Mn(01)-C(01)	1.792(5)	C(01)-Mn(01)-C(03)	86.9(2)
Mn(01)-C(03)	1.805(5)	C(01)-Mn(01)-C(02)	90.4(2)
Mn(01)-C(02)	1.813(5)	C(03)-Mn(01)-C(02)	86.8(2)
Mn(01)-N(01)	2.040(4)	C(01)-Mn(01)-N(01)	91.85(19)
Mn(01)-N(02)	2.042(4)	C(03)-Mn(01)-N(01)	174.77(19)
Mn(01)-O(04)	2.068(4)	C(02)-Mn(01)-N(01)	98.3(2)
O(04)-H(1B)	0.84(2)	C(01)-Mn(01)-N(02)	94.8(2)

O(04)-H(1A)	0.84(2)	C(03)-Mn(01)-N(02)	95.67(19)
N(01)-C(011)	1.340(6)	C(02)-Mn(01)-N(02)	174.32(18)
N(01)-C(015)	1.356(6)	N(01)-Mn(01)-N(02)	79.36(15)
O(02)-C(02)	1.139(6)	C(01)-Mn(01)-O(04)	174.6(2)
N(02)-C(020)	1.342(6)	C(03)-Mn(01)-O(04)	98.3(2)
N(02)-C(016)	1.352(5)	C(02)-Mn(01)-O(04)	91.06(19)
O(01)-C(01)	1.143(6)	N(01)-Mn(01)-O(04)	82.81(15)
C(016)-C(017)	1.391(6)	N(02)-Mn(01)-O(04)	83.54(15)
C(016)-C(015)	1.469(6)	Mn(01)-O(04)-H(1B)	108(5)
C(017)-C(018)	1.381(7)	Mn(01)-O(04)-H(1A)	125(7)
C(017)-H(016)	0.9300	H(1B)-O(04)-H(1A)	99(3)
C(013)-C(014)	1.381(7)	C(011)-N(01)-C(015)	118.4(4)
C(013)-C(012)	1.383(8)	C(011)-N(01)-Mn(01)	126.3(3)
C(013)-H(013)	0.9300	C(015)-N(01)-Mn(01)	115.2(3)
C(015)-C(014)	1.390(6)	C(020)-N(02)-C(016)	118.5(4)
C(020)-C(019)	1.382(7)	C(020)-N(02)-Mn(01)	125.9(3)
C(020)-H(020)	0.9300	C(016)-N(02)-Mn(01)	115.6(3)
C(019)-C(018)	1.374(7)	N(02)-C(016)-C(017)	121.4(4)
C(019)-H(019)	0.9300	N(02)-C(016)-C(015)	114.7(4)
C(03)-O(03)	1.142(6)	C(017)-C(016)-C(015)	123.9(4)
C(014)-H(014)	0.9300	C(018)-C(017)-C(016)	119.3(4)
C(018)-H(017)	0.9300	C(018)-C(017)-H(016)	120.3
C(011)-C(012)	1.381(7)	C(016)-C(017)-H(016)	120.3
C(011)-H(011)	0.9300	C(014)-C(013)-C(012)	119.2(4)
C(012)-H(012)	0.9300	C(014)-C(013)-H(013)	120.4
S(1)-O(5)	1.249(11)	C(012)-C(013)-H(013)	120.4
S(1)-O(4)	1.332(7)	N(01)-C(015)-C(014)	121.6(4)
S(1)-O(2)	1.374(5)	N(01)-C(015)-C(016)	114.9(4)
S(1)-O(3)	1.559(10)	C(014)-C(015)-C(016)	123.5(4)
S(1)-O(1)	1.656(9)	N(02)-C(020)-C(019)	122.6(4)
S(1)-C(1)	1.789(6)	N(02)-C(020)-H(020)	118.7
C(1)-F(2)	1.242(12)	C(019)-C(020)-H(020)	118.7
C(1)-F(6)	1.317(15)	C(018)-C(019)-C(020)	119.0(4)
C(1)-F(3)	1.330(11)	C(018)-C(019)-H(019)	120.5
C(1)-F(5)	1.331(13)	C(020)-C(019)-H(019)	120.5
C(1)-F(4)	1.336(9)	O(02)-C(02)-Mn(01)	175.3(6)
C(1)-F(1)	1.373(12)	O(03)-C(03)-Mn(01)	174.1(6)
O(5)-O(4)	1.090(14)	O(01)-C(01)-Mn(01)	178.3(5)
		C(013)-C(014)-C(015)	119.2(4)
		C(013)-C(014)-H(014)	120.4
		C(015)-C(014)-H(014)	120.4
		C(019)-C(018)-C(017)	119.2(4)
		C(019)-C(018)-H(017)	120.4
		C(017)-C(018)-H(017)	120.4
		N(01)-C(011)-C(012)	122.8(5)
		N(01)-C(011)-H(011)	118.6
		C(012)-C(011)-H(011)	118.6
		C(011)-C(012)-C(013)	118.8(4)
		C(011)-C(012)-H(012)	120.6
		C(013)-C(012)-H(012)	120.6
		O(5)-S(1)-O(4)	49.8(6)
		O(5)-S(1)-O(2)	138.6(5)
		O(4)-S(1)-O(2)	124.2(4)
		O(5)-S(1)-O(3)	59.1(8)
		O(4)-S(1)-O(3)	108.1(6)

		O(2)-S(1)-O(3)	100.7(7)
		O(5)-S(1)-O(1)	98.7(8)
		O(4)-S(1)-O(1)	51.4(6)
		O(2)-S(1)-O(1)	100.3(6)
		O(3)-S(1)-O(1)	157.1(8)
		O(5)-S(1)-C(1)	110.6(5)
		O(4)-S(1)-C(1)	117.3(4)
		O(2)-S(1)-C(1)	106.5(3)
		O(3)-S(1)-C(1)	94.6(5)
		O(1)-S(1)-C(1)	88.3(5)
		F(2)-C(1)-F(6)	114.4(11)
		F(2)-C(1)-F(3)	110.7(8)
		F(6)-C(1)-F(3)	110.7(11)
		F(2)-C(1)-F(5)	113.8(10)
		F(6)-C(1)-F(5)	20.1(10)
		F(3)-C(1)-F(5)	93.5(8)
		F(2)-C(1)-F(4)	75.1(7)
		F(6)-C(1)-F(4)	121.9(10)
		F(3)-C(1)-F(4)	36.3(6)
		F(5)-C(1)-F(4)	101.9(7)
		F(2)-C(1)-F(1)	28.1(6)
		F(6)-C(1)-F(1)	97.0(11)
		F(3)-C(1)-F(1)	138.8(10)
		F(5)-C(1)-F(1)	105.3(9)
		F(4)-C(1)-F(1)	103.1(9)
		F(2)-C(1)-S(1)	116.7(7)
		F(6)-C(1)-S(1)	105.3(9)
		F(3)-C(1)-S(1)	97.9(6)
		F(5)-C(1)-S(1)	119.5(7)
		F(4)-C(1)-S(1)	121.3(6)
		F(1)-C(1)-S(1)	103.7(7)
		O(4)-O(5)-S(1)	69.0(8)
		O(5)-O(4)-S(1)	61.1(7)

Table B.9: Anisotropic displacement parameters ($Å^2$ x 10^3) for *fac*-[Re(Bipy)$(CO)_3$$(H_2O)$][$CF_3SO_3$]. The Anisotropic displacement factor exponent takes the form: $-2\pi^2(h2a^{*2}U^{11} + \ldots + 2hka^*b^*U^{12})$.

	U11	U22	U33	U23	U13	U12
Mn(01)	23(1)	17(1)	24(1)	-1(1)	11(1)	-2(1)
O(04)	60(2)	22(2)	48(2)	7(1)	39(2)	11(2)
N(01)	21(2)	24(2)	23(2)	-6(1)	12(1)	-3(1)
O(02)	97(4)	39(2)	41(2)	-10(2)	41(2)	-38(2)
N(02)	22(2)	19(2)	25(2)	-1(1)	9(1)	-2(1)
O(01)	115(4)	44(2)	46(2)	2(2)	57(3)	17(3)
C(016)	22(2)	21(2)	21(2)	-1(2)	9(2)	1(2)
C(017)	32(2)	22(2)	24(2)	2(2)	12(2)	0(2)
C(013)	22(2)	42(3)	22(2)	-8(2)	7(2)	7(2)
C(015)	21(2)	22(2)	21(2)	-4(2)	10(2)	2(2)
C(020)	22(2)	27(2)	31(2)	4(2)	7(2)	-2(2)
C(019)	24(2)	31(2)	32(2)	-3(2)	10(2)	-9(2)
C(02)	48(3)	32(2)	26(2)	-7(2)	21(2)	-14(2)
C(03)	33(2)	20(2)	46(3)	7(2)	13(2)	1(2)
C(01)	44(3)	25(2)	27(2)	2(2)	15(2)	1(2)
C(014)	26(2)	29(2)	22(2)	-3(2)	10(2)	4(2)
C(018)	40(3)	23(2)	31(2)	-2(2)	19(2)	-10(2)

C(011)	25(2)	29(2)	31(2)	-10(2)	15(2)	-6(2)
C(012)	20(2)	38(3)	32(2)	-16(2)	10(2)	-4(2)
O(03)	41(2)	39(2)	57(3)	20(2)	-1(2)	9(2)
S(1)	119(2)	33(1)	64(1)	-13(1)	56(1)	-35(1)
C(1)	35(3)	43(3)	29(2)	5(2)	17(2)	7(2)
F(3)	13(3)	77(7)	94(8)	-26(7)	-7(4)	-5(4)
F(5)	17(3)	52(6)	17(3)	2(3)	1(2)	3(3)
F(2)	47(6)	23(4)	58(5)	0(3)	28(5)	-13(4)
O(5)	90(3)	60(3)	31(2)	1(2)	18(2)	-23(2)
O(4)	60(2)	22(2)	48(2)	7(1)	39(2)	11(2)
F(4)	51(5)	100(8)	47(4)	-3(5)	19(4)	-43(6)
F(6)	228(18)	63(7)	81(10)	-13(8)	122(12)	-26(12)
F(1)	102(10)	62(8)	54(5)	-6(5)	21(7)	53(7)
O(1)	52(4)	44(4)	180(10)	-22(5)	39(5)	6(3)
O(3)	52(4)	44(4)	180(10)	-22(5)	39(5)	6(3)
O(2)	90(3)	60(3)	31(2)	1(2)	18(2)	-23(2)

Table B.10: Hydrogen coordinates (x 10^4) and isotropic displacement parameters ($Å^2$ x 10^3) for *fac*-[Re(Bipy)$(CO)_3(H_2O)][CF_3SO_3]$.

	x	y	z	U(eq)
H(016)	6536	-1614	10016	32
H(013)	10926	396	11340	37
H(020)	3281	1061	7990	36
H(019)	2537	-1018	8244	38
H(014)	8664	-638	10736	31
H(017)	4187	-2399	9254	37
H(011)	9380	3344	9703	33
H(012)	11289	2394	10797	38
H(1B)	4870(30)	3780(70)	9280(40)	60(20)
H(1A)	6130(70)	4210(60)	9770(50)	130(40)

Table B.11: Torsion angles (°) for *fac*-[Re(Bipy)$(CO)_3(H_2O)][CF_3SO_3]$.

Torsion Angle	Angle	Torsion Angle	Angle
C(01)-Mn(01)-N(01)-C(011)	84.0(4)	C(03)-Mn(01)-N(01)-C(011)	161(2)
N(02)-Mn(01)-N(01)-C(011)	178.6(4)	O(04)-Mn(01)-N(01)-C(011)	-96.7(4)
C(01)-Mn(01)-N(01)-C(015)	-98.2(3)	C(03)-Mn(01)-N(01)-C(015)	-22(2)
C(02)-Mn(01)-N(01)-C(015)	171.1(3)	N(02)-Mn(01)-N(01)-C(015)	-3.7(3)
O(04)-Mn(01)-N(01)-C(015)	81.1(3)	C(01)-Mn(01)-N(02)-C(020)	-89.3(4)
C(03)-Mn(01)-N(02)-C(020)	-1.9(4)	C(02)-Mn(01)-N(02)-C(020)	114(2)
N(01)-Mn(01)-N(02)-C(020)	179.7(4)	O(04)-Mn(01)-N(02)-C(020)	95.8(4)
C(01)-Mn(01)-N(02)-C(016)	92.5(3)	C(03)-Mn(01)-N(02)-C(016)	179.9(3)
C(02)-Mn(01)-N(02)-C(016)	-64(2)	N(01)-Mn(01)-N(02)-C(016)	1.6(3)
O(04)-Mn(01)-N(02)-C(016)	-82.3(3)	C(020)-N(02)-C(016)-C(017)	3.0(6)
Mn(01)-N(02)-C(016)-C(017)	-178.7(3)	C(020)-N(02)-C(016)-C(015)	-177.7(4)
Mn(01)-N(02)-C(016)-C(015)	0.6(5)	N(02)-C(016)-C(017)-C(018)	-1.0(7)
C(015)-C(016)-C(017)-C(018)	179.7(4)	C(011)-N(01)-C(015)-C(014)	2.7(6)
Mn(01)-N(01)-C(015)-C(014)	-175.3(3)	C(011)-N(01)-C(015)-C(016)	-177.0(4)
Mn(01)-N(01)-C(015)-C(016)	5.1(4)	N(02)-C(016)-C(015)-N(01)	-3.8(5)
C(017)-C(016)-C(015)-N(01)	175.6(4)	N(02)-C(016)-C(015)-C(014)	176.6(4)
C(017)-C(016)-C(015)-C(014)	-4.0(7)	C(016)-N(02)-C(020)-C(019)	-2.8(7)
Mn(01)-N(02)-C(020)-C(019)	179.1(4)	N(02)-C(020)-C(019)-C(018)	0.6(8)
C(01)-Mn(01)-C(02)-O(02)	101(5)	C(03)-Mn(01)-C(02)-O(02)	14(5)
N(01)-Mn(01)-C(02)-O(02)	-167(5)	N(02)-Mn(01)-C(02)-O(02)	-102(5)

O(04)-Mn(01)-C(02)-O(02)	-84(5)	C(01)-Mn(01)-C(03)-O(03)	-13(4)
C(02)-Mn(01)-C(03)-O(03)	78(4)	N(01)-Mn(01)-C(03)-O(03)	-90(5)
N(02)-Mn(01)-C(03)-O(03)	-107(4)	O(04)-Mn(01)-C(03)-O(03)	168(4)
C(03)-Mn(01)-C(01)-O(01)	50(18)	C(02)-Mn(01)-C(01)-O(01)	-37(18)
N(01)-Mn(01)-C(01)-O(01)	-135(18)	N(02)-Mn(01)-C(01)-O(01)	145(18)
O(04)-Mn(01)-C(01)-O(01)	-143(17)	C(012)-C(013)-C(014)-C(015)	-0.3(6)
N(01)-C(015)-C(014)-C(013)	-1.8(6)	C(016)-C(015)-C(014)-C(013)	177.8(4)
C(020)-C(019)-C(018)-C(017)	1.4(7)	C(016)-C(017)-C(018)-C(019)	-1.2(7)
C(015)-N(01)-C(011)-C(012)	-1.5(6)	Mn(01)-N(01)-C(011)-C(012)	176.2(3)
N(01)-C(011)-C(012)-C(013)	-0.5(7)	C(014)-C(013)-C(012)-C(011)	1.4(7)
O(5)-S(1)-C(1)-F(2)	117.8(9)	O(4)-S(1)-C(1)-F(2)	172.2(7)
O(2)-S(1)-C(1)-F(2)	-43.4(7)	O(3)-S(1)-C(1)-F(2)	59.2(8)
O(1)-S(1)-C(1)-F(2)	-143.6(8)	O(5)-S(1)-C(1)-F(6)	-10.2(11)
O(4)-S(1)-C(1)-F(6)	44.2(11)	O(2)-S(1)-C(1)-F(6)	-171.4(10)
O(3)-S(1)-C(1)-F(6)	-68.8(11)	O(1)-S(1)-C(1)-F(6)	88.4(11)
O(5)-S(1)-C(1)-F(3)	-124.2(10)	O(4)-S(1)-C(1)-F(3)	-69.8(8)
O(2)-S(1)-C(1)-F(3)	74.6(8)	O(3)-S(1)-C(1)-F(3)	177.1(9)
O(1)-S(1)-C(1)-F(3)	-25.6(9)	O(5)-S(1)-C(1)-F(5)	-25.7(9)
O(4)-S(1)-C(1)-F(5)	28.8(8)	O(2)-S(1)-C(1)-F(5)	173.2(7)
O(3)-S(1)-C(1)-F(5)	-84.3(9)	O(1)-S(1)-C(1)-F(5)	73.0(8)
O(5)-S(1)-C(1)-F(4)	-154.1(9)	O(4)-S(1)-C(1)-F(4)	-99.6(8)
O(2)-S(1)-C(1)-F(4)	44.7(8)	O(3)-S(1)-C(1)-F(4)	147.3(9)
O(1)-S(1)-C(1)-F(4)	-55.4(9)	O(5)-S(1)-C(1)-F(1)	91.1(10)
O(4)-S(1)-C(1)-F(1)	145.5(8)	O(2)-S(1)-C(1)-F(1)	-70.1(8)
O(3)-S(1)-C(1)-F(1)	32.5(9)	O(1)-S(1)-C(1)-F(1)	-170.3(9)
O(2)-S(1)-O(5)-O(4)	-98.9(10)	O(3)-S(1)-O(5)-O(4)	-168.3(10)
O(1)-S(1)-O(5)-O(4)	17.5(8)	C(1)-S(1)-O(5)-O(4)	108.9(7)
O(2)-S(1)-O(4)-O(5)	127.8(7)	O(3)-S(1)-O(4)-O(5)	10.6(9)
O(1)-S(1)-O(4)-O(5)	-157.7(11)	C(1)-S(1)-O(4)-O(5)	-94.7(7)
C(02)-Mn(01)-N(01)-C(011)	-6.7(4)		

Table B.12: Hydrogen bond distances (Å) and angles (°) for *fac*-[Re(Bipy)(CO)$_3$(H$_2$O)][CF$_3$SO$_3$].

D-H…A	d (D-H)	d (H…A)	d (D…A)	D-H…A angle
O(04)-H(1A)...O(2)#1	0.84(2)	2.17(5)	2.895(7)	144(8)
O(04)-H(1A)...O(3)#1	0.84(2)	2.31(7)	3.035(16)	144(10)
O(04)-H(1A)...O(2)#1	0.84(2)	2.17(5)	2.895(7)	144(8)
C(013)-H(013)...O(03)#2	0.93	2.56	3.222(6)	128.4
C(012)-H(012)...O(02)#3	0.93	2.55	3.362(6)	146.0

Symmetry transformations used to generate equivalent atoms:
#1 -x+2,y+1/2,-z+5/2 #2 x+1,-y+1/2,z+1/2 #3 -x+2,-y+1,-z+2

APPENDIX C

The methanol substitution reactions between *fac*-$[Mn(Phen)(CO)_3(MeOH)]^+$ and pyridine (Py), thiourea (TU) and bromide ions (Br^-) as entering ligands were followed. Each reaction was performed at four temperatures (15.0, 25.0, 35.0 and 45.0 °C) and the manganese concentration was kept constant at 5 x 10^{-4} M throughout.

Table C.1: Temperature and [Py] dependence of the *pseudo* first-order reaction between *fac*-$[Mn(Phen)(CO)_3(MeOH)]^+$ and pyridine. [Mn] = 5 x 10^{-4} M, λ = 370 nm, MeOH.

	$10^4 k_{obs}$ (s^{-1})			
[Py] (M)	**15.0 °C**	**25.0 °C**	**35.0 °C**	**45.0 °C**
0.01	0.126±0.003	0.409±0.006	1.04±0.05	3.50±0.05
0.02	0.232±0.005	0.641±0.005	1.79±0.04	5.33±0.06
0.04	0.395±0.007	1.03±0.02	2.88±0.05	9.79±0.02
0.05	0.453±0.003	1.37±0.01	3.56±0.03	12.8±0.5
0.075	0.678±0.002	1.98±0.04	5.20±0.09	17.3±0.4
0.1	0.806±0.008	2.53±0.03	6.70±0.03	22±2

Table C.2: Temperature and [TU] dependence of the *pseudo* first-order reaction between *fac*-$[Mn(Phen)(CO)_3(MeOH)]^+$ and thiourea. [Mn] = 5 x 10^{-4} M, λ = 375 nm, MeOH.

	$10^3 k_{obs}$ (s^{-1})			
[TU] (M)	**15.0 °C**	**25.0 °C**	**35.0 °C**	**45.0 °C**
0.01	1.43±0.04	3.14±0.04	4.83±0.05	8.46±0.05
0.02	1.63±0.02	3.62±0.08	6.56±0.02	10.7±0.2
0.04	2.20±0.07	5.3±0.1	9.12±0.02	17.9±0.2
0.05	2.54±0.03	5.97±0.07	9.87±0.07	20.0±0.8
0.075	3.21±0.04	8.03±0.05	14.7±0.04	25.2±0.4
0.1	3.60±0.04	9.61±0.01	17.4±0.5	32.8±0.3

Table C.3: Temperature and [Br^-] dependence of the *pseudo* first-order reaction between *fac*-$[Mn(Phen)(CO)_3(MeOH)]^+$ and bromide ions. [Mn] = 5 x 10^{-4} M, λ = 370 nm, MeOH.

	$10^2 k_{obs}$ (s^{-1})			
[Br^-] (M)	**15.0 °C**	**25.0 °C**	**35.0 °C**	**45.0 °C**
0.01	1.2±0.1	2.83±0.03	6.25±0.04	18.4±0.3
0.02	1.4±0.3	3.17±0.05	7.8±0.1	22.4±0.6
0.04	1.771±0.008	4.3±0.1	10.0±0.7	28.1±0.3
0.05	2.04±0.06	4.50±0.06	11.9±0.4	31.3±0.7
0.075	2.6±0.2	6.008±0.009	14.6±0.5	39±1
0.1	2.9±0.1	7.25±0.04	17.9±0.7	45±2

Appendix C

The methanol substitution reactions between *fac*-[Mn (Bipy)$(CO)_3$(MeOH)]$^+$ and pyridine (Py), thiourea (TU) and bromide ions (Br^-) as entering ligands were followed. Each reaction was performed at 25.0 °C and the manganese concentration was kept constant at 5 x 10^{-4} M throughout.

Table C.4: [Py], [TU] and [Br^-] dependence of the *pseudo* first-order reaction between *fac*-[Mn(Bipy)$(CO)_3$(MeOH)]$^+$ and pyridine, thiourea and bromide ions at 25.0 °C. [Mn] = 5 x 10^{-4} M λ (Pyridine) = 370 nm , λ (Thiourea) = 365 nm , λ (Bromide) = 445 nm, MeOH.

10^3 k_{obs} (s^{-1})			
[Ligand] (M)	**[Py]**	**[TU]**	**[Br^-]**
0.01	0.0384±0.0007	1.13±0.04	12.5±0.4
0.02	0.0738±0.0005	2.27±0.05	17.1±0.6
0.04	0.116±0.004	4.33±0.01	21.5±0.4
0.05	0.153±0.003	5.34±0.06	23.2±0.8
0.075	0.233±0.006	7.56±0.06	30.3±0.3
0.1	0.301±0.002	9.76±0.02	41.1±0.2

The methanol substitution reactions between *fac*-[Mn(Pico)$(CO)_3$(MeOH)] and pyridine (Py), thiourea (TU) and bromide ions as entering ligands were followed. Each reaction was performed at four temperatures (15.0, 25.0, 35.0 and 45.0 °C) and the manganese concentration was kept constant at 3 x 10^{-3} M throughout.

Table C.1: Temperature and [Py] dependence of the *pseudo* first-order reaction between *fac*-[Mn(Pico)$(CO)_3$(MeOH)] and pyridine. [Mn] = 3 x 10^{-3} M, λ = 365 nm, MeOH.

10^2 k_{obs} (s^{-1})				
[Py] (M)	**15.0 °C**	**25.0 °C**	**35.0 °C**	**45.0 °C**
0.01	0.397±0.003	1.02±0.02	4.07±0.05	14.3±0.3
0.02	0.748±0.008	1.80±0.09	6.54±0.02	19.8±0.2
0.04	1.46±0.02	2.84±0.03	12.8±0.2	35.3±0.5
0.05	1.95±0.01	3.71±0.05	15.5±0.5	39.9±0.7
0.075	2.81±0.06	6.36±0.03	25±2	48.5±0.7
0.1	3.83±0.05	8.51±0.02	33.6±0.3	54.5±0.5

Appendix C

Table C.6: Temperature and [TU] dependence of the *pseudo* first-order reaction between *fac*-[Mn(Pico)(CO)$_3$(MeOH)] and thiourea. [Mn] = 3 x 10^{-3} M, λ = 385 nm, MeOH.

	10^{1} k_{obs} (s^{-1})			
[TU] (M)	**15.0 °C**	**25.0 °C**	**35.0 °C**	**45.0 °C**
0.01	0.281±0.003	0.700±0.005	1.78±0.05	3.8±0.1
0.02	0.462±0.004	1.09±0.04	2.54±0.03	5.4±0.2
0.04	0.813±0.007	1.97±0.07	4.20±0.02	8.7±0.1
0.05	0.981±0.007	2.80±0.03	5.85±0.05	10.6±0.3
0.075	1.42±0.02	3.47±0.04	7.5±0.8	15.5±0.2
0.1	1.91±0.06	4.57±0.05	9.6±0.4	19.0±0.3

Table C.7: Temperature and [Br$^-$] dependence of the *pseudo* first-order reaction between *fac*-[Mn(Pico)(CO)$_3$(MeOH)] and bromide ions. [Mn] = 3 x 10^{-3} M, λ = 415 nm, MeOH.

	10^{2} k_{obs} (s^{-1})			
[Br$^-$] (M)	**15.0 °C**	**25.0 °C**	**35.0 °C**	**45.0 °C**
0.01	0.898±0.003	2.2±0.1	5.8±0.1	20.3±0.2
0.02	1.03±0.05	3.0±0.1	7.1±0.2	22.1±0.3
0.04	1.38±0.02	4.1±0.2	8.9±0.1	28.6±0.4
0.05	1.54±0.06	4.056±0.009	10.1±0.3	32.8±0.4
0.075	2.11±0.05	5.9±0.1	13.1±0.5	39.2±0.7
0.1	2.44±0.06	6.4±0.3	16.1±0.4	45.5±0.4

The methanol substitution reaction between *fac*-[Mn(2,4-Quin)(CO)$_3$(MeOH)] and pyridine (Py) and thiourea (TU) as entering ligands was followed. Each reaction was performed at 25.0 °C and the manganese concentration was kept constant at 2.5 x 10^{-4} M throughout.

Table C.8: [Py] and [TU] dependence of the *pseudo* first-order reaction between *fac*-[Mn(2,4-Quin)(CO)$_3$(MeOH)] and pyridine and thiourea at 25.0 °C. [Mn] = 2.5 x 10^{-4} M, λ (pyridine) = 380 nm and λ (thiourea) = 395 nm, MeOH.

	10^{1} k_{obs} (s^{-1})	
[Ligand] (M)	**[Py]**	**[TU]**
0.01	0.71±0.02	3.14±0.06
0.02	1.17±0.05	4.66±0.04
0.04	2.36±0.03	6.7±0.1
0.05	2.57±0.03	7.1±0.1
0.075	3.94±0.01	9.2±0.2
0.1	4.67±0.05	10.1±0.1

1 BACKGROUND & AIM

1.1. Background

Manganese is found as a free element in nature with an atomic number of 25 on the periodic table. It was discovered in 1774 by J.G. Grahn.[1] The metal is mostly used in alloys such as steel. It is one of the most abundant elements in the earth's crust and its most stable isotope is ^{52}Mn. Other radioisotopes of manganese exist but their half-lives are generally less than an hour or even less than a minute.[2]

Manganese compounds are widely used in catalysis with one of its main uses being the synthesis of manganese complexes of corroles. These are used as catalysts in epoxidation, cyclopropanation, asymmetric sulfoxination, aziridination and oxygen atom transfer reactions. The oxidation state of these manganese corroles ranges from +3 to +6.[3]

Manganese is also widely used as a catalyst in water oxidation to form hydrogen by water splitting. Manganese Schiff base complexes are synthesized and used as catalysts in order to evolve oxygen. Manganese is a cheap and environmentally friendly product since it's used in nature to oxidize water.[4]

Recently some work has been reported on the use of manganese in MEMRI. In this work reported by Topping *et al*., Mn^{2+} is used as a contrast agent *in vivo* that is used to reduce the T1 relaxation times.[5] A study on mice has shown that manganese can accumulate in the brain for as long as three months and this may cause central nervous system diseases.[6] In other biological studies, manganese superoxide dismutase (MnSOD) which is an antioxidant enzyme is used in the suppression of tumors.[7] Also,

---

[1] Emsley, J., An A-Z Guide to the Elements, *Oxford University Press*, 2nd Ed., 2011.
[2] Audi, G., Wapstra, A.H., Thibault, C., Blachot, J., Bersillon, O., *Nuclear Physics A*, **729**, 2003, 3.
[3] Liu, H., Mahmood, M.H.R., Qui, S., Chang, C., *Coord. Chem. Rev*., **257**, 2013, 1306.
[4] Najafpout, M.M., Allakhverdiev, S.I., *Int. J. Hydrogen Energy.,* **37**, 2012, 8753.
[5] Topping, G.J., Schaffer, P., Hoehr, C., Ruth, T.J., Sossi, V., *Med. Phys*. **40**, 2013, 042502-1.
[6] Gallez, B., Baudelet, C., Adline, J., Geurts, M., Delzenne, N., *Chem. Res. Toxicol.*, **10**, 1997, 360.
[7] Belikova, N.A., Glumac, A., Rafikov. R., Jiang, J., Greenberger, J.S., Kagan, V.E., Bayir, H., *FEBS Lett*. **583**, 2009, 3437.

MnSOD has the important ability to protect against oxidative stress and injury to cells and tissues caused by radiation.[7,8]

Although not much has been investigated for manganese in radiopharmaceuticals, the manganese triad is famous for the work in radiochemistry, with a wide range of radiopharmaceuticals synthesized from technetium. ^{99m}Tc is the radionuclide mostly used for brain, kidney, heart and liver imaging.[9] Rhenium is used as a model for technetium because of its similarity in chemical properties. A few studies have proven its use as radiopharmaceutical in which ^{188}Re and ^{186}Re was used in therapy.[10] The *fac*-$[M(CO)_3]^+$ (M = Mn, Re, Tc) core has been used by research groups, because of the stability of this core. Most of the reported studies are on *fac*-$[Re(CO)_3]^+$ and *fac*-$[Tc(CO)_3]^+$ type complexes.[11,12] Water substitution and water exchange reactions have been performed by Helm[13] and it was found that Mn (I) reacts faster than Tc (I) which in turn reacts faster than Re (I).[14]

1.2. Aim

One of the main objectives of this study was to synthesize and characterize Mn (I) tricarbonyl complexes and to investigate the solution *versus* solid state differences. The stepwise aims of this study are summarized below:

- Synthesis of new Mn (I) tricarbonyl complexes. A wide range of bidentate ligand systems will be used. As N,N'-bidentate ligands, 1,10-phenanthroline (Phen) and 2,2'-bipyridine (Bipy) were used while picolinic acid (Pico) and quinoline-2,4-dicarboxylic acid (2,4-Quin) were used as N,O-bidentate ligands. 3-Hydroxyflavone (Flav) was used as an O,O'-bidentate ligand.
- Characterize these complexes by single crystal X-ray crystallography, IR, ^{1}H NMR and ^{13}C NMR.
- Determination of the mechanism of the methanol substitution reactions between *fac*-$[Mn(Phen)(CO)_3(MeOH)]^+$ and pyridine, thiourea and bromide ions, between *fac*-$[Mn(Bipy)(CO)_3(MeOH)]$ and *fac*-$[Mn(Pico)(CO)_3(MeOH)]$ and pyridine, thiourea and bromide ions and between *fac*-$[Mn(I2,4\text{-}Quin)(CO)_3(MeOH)]$ and

[8] Whittaker, M.M., Whittaker, J.W., *Arch. Biochem. Biophys*., **491**, 2009, 69.
[9] Jürgens, S., Herrmann, W.A., Kühn, F.E., *J. Organo. Chem*., **30**, 2013, 1.
[10] Kothari, K., Pillai, M.R.A., Unni, P.R., Shimpi, H.H., Noronha, O.P.D., Samuel, A.M., *Appl. Radiat. Isot*., 1999, 51.
[11] Schutte, M., Kemp, G., Visser, H.G., Roodt, A., *Inorg. Chem.,* **50**,2011,12486.
[12] Alberto, R., Schibli, R., Waibel, R., Abram, E., Schubiger, A.P., *Coord. Chem. Rev*. **190-192**, 1999, pg 901.
[13] Helm, L., *Coord. Chem. Rev.,* **252**, 2008, 2346.
[14] Grundler, P.V., Helm, L., Alberto, R., Merbach, A.E., *Inorg. Chem.,* **45**, 2006, 10378.

pyridine and thiourea by means of a kinetic and temperature study, and isolation and characterization of the final products.

2 LITERATURE STUDY

2.1 A Brief History of Manganese

Manganese was discovered in 1774. The name manganese is derived from the Latin word 'magnes' which means magnet. Most of the ores rich in manganese are found in South Africa and India. Manganese plays an important role in steel alloys. It is often added to steel to make hard steel that is shock resistant. Manganese permanganate is the most common chemical compound used in laboratories and is used as an indicator for acidic solutions.[1] Manganese in its biological role is found in an metalloenzyme known as Mangnaese superoxide dismutase (MnSOD). This metalloenzyme is found in mitochondria and is essential for the survival of all aerobic organisms in bacteria and human beings. The superoxide dismutase family also consists of copper zinc SOD, copper SOD and iron SOD.[2]

2.2 Manganese in Catalysis

Manganese is commonly used as a catalyst or in various catalytic cycles. Manganese corroles are used in epoxidation, assymetric sulfoxidation, hydroxylation, azirdination and atom transfer reactions; this is where it displays catalytic activity the most.[3] A corrole is an 18-π electron tetrapyrrolic macrocycle that contains a direct pyrrole-pyrrole link. Corroles resemble porphyrins, corrin and corrolazine. Their most important property is the presence of three protons in their inner core, which stabilizes metals in different oxidation states. Manganese corroles (Figure 2.1) may be applied in catalysis, ion-selective electrodes, Langmuir-Blodgett films, single-chain magnets and medicinal research. As stated earlier manganese corroles dispay catalytic activity in various chemical reactions, one of it being epoxidation of olefins. In the catalysed epoxidation of styrene, a Mn(III) corrole is used. The epoxidation proceeds *via* fast oxygen transfer to form an (oxo)manganese (V) corrole. When the manganese corroles have

---

[1] Stwertka, A., *A Guide To The Elements* 2nd Ed., Oxford University Press, 2002,87.
[2] Haikarainen, T., Frioux, C., Zhnag, L., Li, D., Papageorgiou, A.C., *Biochim. Biophys. Acta*, **1844**, 2014, 422.
[3] Ng, N., Mahmood, M.H.R., Liu, H., Yeung, L., Chang, C., *Chin. Chem. Lett*., 2004.

electronegative substituents, oxidation of electron rich alcohols to carbonyl compounds may be achieved at mild and room temperatures. [4]

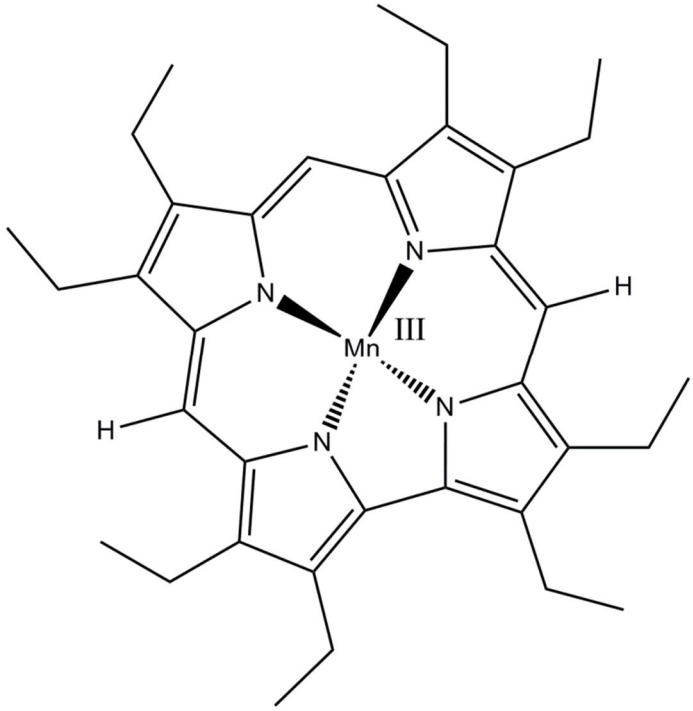

Figure 2.1: A typical Manganese (III) corrole used in catalysis.

The water oxidizing complex of Photosystem II, an artificial photosynthetic system, is the only system that is used to catalyse water oxidation. The complex used in water oxidation is Mn_4O_5Ca and is housed in a protein environment that controls reaction coordinates, proton movement and water excess. Only a few manganese complexes have been discovered that can act as catalysts for oxygen evolution. It has been reported that manganese Schiff base complexes were observed to oxidize water in the presence of cerium (IV). Electron withdrawing substituents on the ligand enhances the reactivity of the manganese complexes towards oxygen evolution when the heterogeneous water oxidation by bidentate manganese Schiff base complexes are in the presence of Ce(V).[5] Shimazaki *et al*. reported on the oxidation of a dimanganese complex of dimeric tetraarylporphyrin that is linked by a 1,2-phenylene bridge. They proposed that a Mn(V)O specie would be the result if a dimanganese (III) tetraarylporphyrin was oxidized. It was reported that oxygen was freed once the Mn(V)O complex was oxidized with meta-chloroperoxybenzoic acid and triflouromethanesulfonic acid was added.

[4] Liu, H., Mahmood, M.H.R., Qui, S., Chang, C., *Coord. Chem. Rev*., **257**, 2013, 1306.
[5] Najafpout, M.M., Allakhverdiev, S.I., *Int. J. Hydrogen Energy.,* **37**, 2012, 8753.

The use of manganese oxides that have calcium ions incorporated, can improve the oxidation activity of manganese oxides. In the calcium manganese oxides, the amorphous oxides showed the best oxidation results.[5]

2.3 The Manganese Triad in Radiopharmacy

The manganese triad consists of technetium, manganese and rhenium. Due to the radiopharmaceutical properties of technetium, studies have been done on the triad in terms of cancer imaging and treatment. Technetium is the most widely used metal of the three while rhenium acts as a model for the technetium complexes already in use in radiopharmacy.

2.3.1 Radioisotopes of Mn, Tc and Re

Radioisotopes or radionuclides, are used to make a variety of radiopharmaceuticals. The radioisotope is coupled to a stable compound that is localized in organs or diseased states. For the radioisotope to be used in nuclear medicine it should possess the following properties:[6]

- Minimum emission,
- photon energy between 50 and 500 keV,
- physical half-life greater than the time required to prepare material for injection,
- effective half-life longer than examination time,
- suitable chemical form and reactivity,
- low toxicity and
- stability or near-stability of the product.

Manganese has 25 radioisotopes but only three highly stable radioisotopes namely: ^{53}Mn with a half-life of 3.7 million years, ^{54}Mn with a half-life of 312.3 days and ^{52}Mn with a half-life of 5.591 days. The rest of the radioisotopes have half-lives less than 3 hours with the most having half-lives less than a minute.[7]

Technetium has three stable radioisotopes: ^{98}Tc with a half-life of 4.2 million years, ^{97}Tc with a half-life of 2.6 million years and ^{99}Tc with a half-life of 211.1 thousand years. There are 33 other characterized radioisotopes with half-lives less than an hour with the exception of ^{93}Tc, ^{94}Tc, ^{95}Tc and ^{96}Tc which have half-lives less than five days.

[6] Mettler, F.A., Guiberteau, M.J., Essentials of Nuclear Medicine Imaging, *Elsevier Inc*., 5th Ed., 2006, 6.
[7] Audi, G., Wapstra, A.H., Thibault, C., Blachot, J., Bersillon, O., *Nuclear Physics A*, **729**, 2003, 3.

Rhenium has two naturally occurring isotopes, ^{185}Re which is stable and ^{187}Re which is unstable and has a half-life of 41.2×10^9 years. There are 33 other unstable isotopes of which five have very long half-lives. ^{183}Re has a half-life of 70 days, ^{184}Re with a half-life of 38 days, ^{186}Re with a half-life of 3.71866 days, ^{182}Re with a half-life of 64 hours , ^{189}Re with a half-life of 24.3 hours as well as ^{188}Re with a half-life of 17 hours.

2.3.2 Manganese

Manganese has not been utilized frequently in radiopharmaceuticals due to the fact that it can be neurotoxic in some instances. An excess of manganese may cause diseases such as the Creutzfeldt-Jakob disease where the manganese competes for the copper binding site of the antioxidant prion and this could lead to the loss of functioning and delirious effects of the nervous system.[8] In a study of the accumulation of manganese in the brain, it was determined that Mn^{2+} can remain in the brain for as long as 3 months after exposure.[9] The manganese may be used as a model for Re (I) and Tc (I) compounds, but this has not been investigated yet.

2.3.3 Manganese-Enhanced Magnetic Resonance Imaging

Manganese-enhanced magnetic resonance imaging (MEMRI) is used in preclinical investigations because manganese can reduce the relaxation time constant T_1 of tissue water, resulting in positive contrast enhancement in T_1-weighted images.[10] This characteristic of manganese was reported and published by Paul Lauterbur in 1973.[11] MEMRI has been widely used to trace specific neuronal connections in the brain, to study cortical activity, in localization of cortical lesions in rodent models with brain disorders and to investigate the epileptogenic processes in epilepsy models. MEMRI is also used as a highly sensitive *in vivo* technique for tracking cortical cytoarchitectonics in normal brain and translational models of brain diseases. There are three major applications of MEMRI:[12]

- The use of Mn^{2+} as a contrast agent for better definition of the tissue architecture,
- the use of Mn^{2+} as a biological calcium analogue for the study of the increases in the brain or cardiac functions and

[8] Arndt, A., Borella, M.I., Espósito, B.P., Chemosphere, **96**, 2014, 46.
[9] Gallez, B., Baudelet, C., Adline, J., Geurts, M., Delzenne, N., *Chem. Res. Toxicol.*, **10**, 1997, 360.
[10] Moroni, R.F., Zucca, I., Inverardi, F., Mastropietro, A., Regondi, M.C., Spreafico, R., Frassoni, C., *Nueroscience*, 192, 2011, 564.
[11] Lauterbur, P.C., *Nature*, **242**, 1973, 190.
[12] Koretsky, A.P., Silva, A.C., NMR *Biomed*., **17** , 2004, 527.

- the exploitation of the fact that once inside the cells in a specific region of the brain, the Mn^{2+} moves along the appropriate neuronal pathways in an anterograde direction.

2.3.4 Manganese Isotopes and Cascade Background

Manganese has three positron-emitting isotopes that have half-lives suitable for use as PET tracers. ^{52}Mn has a half-life of 5.591 days, ^{52m}Mn has a half-life of 21.1 minutes and ^{51}Mn has a half-life of 46.2 minutes. ^{52}Mn is chosen for its low positron energy of 244.6 keV and a tissue range of 0.62 mm which is comparable to ^{18}F (250 keV, 0.62 mm). ^{51}Mn and ^{52m}Mn have larger positron ranges and this may blur smaller image details. The long half-life of ^{52}Mn makes it useful for tracers that are being compared with MEMRI, which shows signal enhancement due to retention of administered Mn days and weeks afterwards. The long half-life also gives enough time for the separation of manganese from the chromium foil in which it is produced.

^{52}Mn has 19 possible gamma emission energies of which two or three may occur with high probability in cascade with positron emission and detected by PET systems, in coincidence with positron annihilation photons. The cascade gamma energies of ^{52}Mn are well separated from 511 keV as this allows the PET energy window to be set to exclude many of the events. A summary of the gamma emission energies of ^{52}Mn are given in Table 2.1.

Table 2.1: Gamma emission energies of ^{52}Mn.

Emission	Probability per decay (%)	Gamma energy (keV)
2 × annihilation	29.6	511.0
Gamma	90.0	744.2
Gamma	94.5	935.5
Gamma	100	1434

2.3.5 Uses of ^{52}Mn in MEMRI and PET

In MEMRI, Mn^{2+} is used *in vivo* as a contrast agent that is used to reduce T1 relaxation times; it accumulates in areas of neuronal activity by uptake through voltage-gated calcium channels. The ^{52}Mn radionuclide is expected to possess the same biological mechanisms *in vivo* as those of the nonradioactive manganese in MEMRI imaging. This means similar systems can be studied with PET as a way to validate the MEMRI

results. ^{52}Mn has been used in a study of manganese absorption in humans, dogs and rats but has not been reported for use in PET imaging. PET imaging using ^{52}Mn has an advantage over MEMRI since it may be administered with mass orders that have lower magnitude than that required for MEMRI without any induced pharmacological effects. Large doses of manganese are injected during animal studies but the dosage is lethal and if injected into the blood stream, it may have long-term toxic effects. Since PET can detect tracer accumulation within the bone, it means that ^{52}Mn can be a potential tracer for investigating bone growth or repair over long times.[13]

2.3.6 Manganese Superoxide Dismutase

Manganese superoxide dismutase (MnSOD) is an antioxidant enzyme that can catalyse the superoxide radicals' conversion to hydrogen peroxide and molecular oxygen. The MnSOD gene may be considered as a potential tumour suppressor.[14] MnSOD is part of the SOD family which includes copper and zinc-containing superoxide dismutase and extracellular superoxide dismutase. In the SOD family, MnSOD is the only enzyme that is necessary for the survival of life in the aerobic environment under physiological conditions.[15] MnSOD plays a crucial role in the protection against oxidative stress.[16] Mitochondrial damage realized through superoxide dependant pathways has a serious role in radiation injury to cells and tissues. The MnSOD provides a line of defence against the overproduction of superoxide in mitochondria. The use of MnSOD as treatment has improved the survival of mice who were exposed to total body irradiation.[17]

2.3.7 Manganese in Breast Cancer Therapy

Breast cancer is one of the most common cancers in women worldwide.[18] It is believed that breast cancer is hereditary, hormonal, reproductive and environmental factors have an important role in its development and progression. The overexpression effects of superoxide dismutase (SOD) have been studied for the effective treatment of breast cancer and other cancers. When adenoviral manganese superoxide dismutase (AdMnSOD) is overexpressed, the breast cell doubling time was reduced to a lesser

[13] Topping, G.J., Schaffer, P., Hoehr, C., Ruth, T.J., Sossi, V., Med. Phys. **40**, 2013, 042502-1.
[14] Urano, M., Kuroda, M., Reynolds, R., Oberley, T.D., St. Clair, D.K., *Cancer Res,* **55**, 1995, 2490.
[15] Dhar, S.K., St. Clair, D.K., *Free Radical Biol. Med*., **52**, 2012, 2209.
[16] Whittaker, M.M., Whittaker, J.W., *Arch. Biochem. Biophys*., **491**, 2009, 69.
[17] Belikova, N.A., Glumac, A., Rafikov. R., Jiang, J., Greenberger, J.S., Kagan, V.E., Bayir, H., *FEBS Lett*. **583**, 2009, 3437.
[18] Eras-Erdogan, N., Akbas, E., Senli, H., Kul, S., Çolak, T., Mutation Res., **680**, 2009, 7.

extent in all cell lines This suggested that the MnSOD gene is viable for the possible treatment of human breast cancer. [19]

2.3.8 Technetium and Rhenium

Techentium-99m is considered as the "workhorse" in the radiopharmaceutical industry. It is a β^- emitting fission product formed in nuclear reactors. There are three major advantages to ^{99m}Tc:

- It emits γ-energy of about 140 keV which makes it possible to penetrate tumor tissue while simultaneously giving off low radiation dose,
- it has a reasonable half-life of 6 hours which ensure enough medical imaging intervals and
- it is readily available at low costs from $^{99}Mo/^{99m}Tc$ generators.

Technitium-99m was first introduced in 1965 for clinical application. The parent isotope ^{99}Mo is processed as molybdate $[^{99}MoO_4]^{2-}$ and loaded onto an alumina chromatography column. ^{99m}Tc is isolated as pertechnetate $[^{99m}TcO_4]^-$ after elution with a 0.5 M saline solution.[20] The production of ^{99m}Tc is illustrated in Figure 2.2.

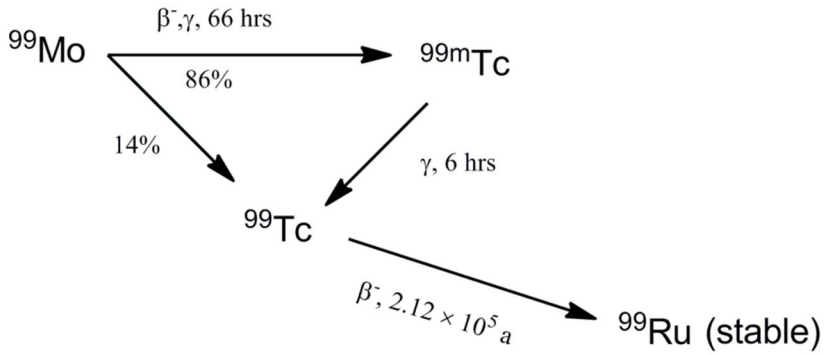

Figure 2.2: Schematic illustration of the production of ^{99m}Tc.

The rhenium β^- emitting radionuclides, ^{188}Re and ^{186}Re, have half-lives of 16.9 hrs and 89.2 hrs respectively. These radionuclides can be isolated from a ^{188}W generator system and both allow an effective energy transfer to cancer tissue. ^{188}Re is the most favoured radionuclide due to its more convenient half-life. Both rhenium and technetium are organ specific and thus the demands on chemical structure and *in vivo* behaviour can vary.

[19] Weydert, C.J., Waugh, T.A., Ritchie, J.M., Iyer, K.S., Smith, J.L., Li, L., Spitz, D.R., Oberley, L.W., Free Radical Biol. Med., 41, 2006, 226.
[20] Jürgens, S., Herrmann, W.A., Kühn, F.E., *J. Organo. Chem*., **30**, 2013, 1.

2.4 Selected Kinetic Studies of Manganese and Related Work

Much attention has been given to aqua tricarbonyl complexes of the Group 7 elements, due to the stability of the *fac*-$[M(CO)_3]^+$ core. The tricarbonyl complexes are not directly practical for radiopharmaceuticals but they are precursors for the aqueous uptake of biconjugate complexes. Therefore their kinetic behaviour is very interesting since it can help in the determination of the preparation, uptake, and the clearance of the radiopharmaceutical agents.[21]

Grundler *et al*.[36] reported that the water exchange of *fac*-$[Mn(CO)_3(H_2O)_3]^+$ was fast enough to produce a line broadening signal of bound water in ^{17}O NMR. The equation for this reaction is as follows:

$$fac\text{-}[Mn(CO)_3(H_2O)_3]^+ + 3H_2{}^*O \rightleftarrows fac\text{-}[Mn(CO)_3(H_2{}^*O)_3]^+ + 3H_2O \qquad \text{Eq. 1}$$

When the slow exchange conditions are satisfied, the observed transverse relaxation rate ($1/T_{2obs}$) has two contributions, the water exchange process and the ^{17}O quadropolar relation ($1/T_{2Q}$). This relation rate is given by:

$$\frac{1}{T_{2obs}} = \frac{1}{\tau_{obs}} + \frac{1}{T_{2Q}} \qquad \text{Eq. 2}$$

τ_{obs} is the mean residence time of a water molecule in the first coordination sphere of the triaqua ion while its inverse, $1/\tau_{obs}$ is equal to the first-order rate constant for the water exchange, k_{obs}, of a particular water molecule. If the complex undergoes hydrolysis, then the k_{obs} will be as in equation 3. k_{ex} is the water exchange rate of the triaqua ion and k_2 of the hydrolysed complex.

$$k_{obs} = k_{ex} + k_2/[H^+] \qquad \text{Eq. 3}$$

Grundler also stated that the poor stability of the complex gave problems especially at high temperatures and lower acidities. The *fac*-$[Mn(CO)_3(H_2O)_3]^+$ complex decomposed to form an Mn^{2+} aqua ion. This did not affect the line width of the bound water. The

[21] Grundler, P.V., Helm, L., Alberto, R., Merbach, A.E., *Inorg. Chem.,* **45**, 2006, 10378.

acidity of the complex was found to be decreasing as it decomposed, giving the equation 4:

$$fac\text{-}[Mn(CO)_3(H_2O)_3]^+ + H^+ \rightarrow Mn(aq)^{2+} + \tfrac{1}{2}H_2 + 3CO \qquad \text{Eq. 4}$$

Table 2.2 shows the results obtained in the study

Table 2.2: Data from the water exchange kinetics.[21]

	K_{ex}^{298} (s^{-1})	ΔH_{ex} ($kJ.mol^{-1}$)	ΔS_{ex} ($J.mol^{-1}.K^{-1}$)	ΔV_{ex} ($cm^3.mol^{-1}$)	Mechanism
fac-$[Mn(CO)_3(H_2O)_3]^+$	23	72.5	+24.4	+7.1	I_d
fac-$[Re(CO)_3(H_2O)_3]^+$	5.4×10^{-3}	90.3	+14.5		I_d
fac-$[^{99m}Tc(CO)_3(H_2O)_3]^+$	0.49	78.3	+11.7	+3.8	I_d

The same water exchange experiment was performed by Helm and the results were confirmed the results in that study. Helm studied the ligand exchange of *fac*-$[Mn(CO)_3(H_2O)_3]^+$ complexes using ^{17}O NMR. He also showed that the rhenium complex are almost three orders of magnitude slower than the technetium complex. The water exchange rate for *fac*-$[Mn(CO)_3(H_2O)_3]^+$ is 23 s^{-1} with $\Delta H^{\dagger}$ = 72.5 $kJ.mol^{-1}$ and $\Delta S^{\dagger}$ = +24.4 $J.K^{-1}.mol^{-1}$, and an I_d mechanism was predicted. For *fac*-$[Tc(CO)_3(H_2O)_3]^+$, the water exchange rate is given as 0.49 s^{-1}, $\Delta H^{\dagger}$ = 78.3 $kJ.mol^{-1}$ and $\Delta S^{\dagger}$ = +11.7 $J.K^{-1}.mol^{-1}$. The results for *fac*-$[Re(CO)_3(H_2O)_3]^+$, gave the water exchange rate as 6.3×10^{-4} s^{-1}, $\Delta H^{\dagger}$ = 90.3 $kJ.mol^{-1}$ and $\Delta S^{\dagger}$ = +14.5 $J.K^{-1}.mol^{-1}$. Both the mechanisms for the technetium and rhenium compounds were predicted as interchange dissociative, I_d.[22]

2.5 Water Substitution Kinetics of *fac*-$[Mn(CO)_3(H_2O)_3]^+$

Water molecules of *fac*-$[Mn(CO)_3(H_2O)_3]^+$ are found to be easily substituted with other ligands. Grundler *et al*.[37] used acetronitrile, dimethyl sulphide as monodentate ligands for the exchange experiment by ^1H NMR. They reported that an increase in temperature led to the broadening of the lines of free and bound ligands. The

[22] Helm, L., *Coord. Chem. Rev.,* **252**, 2008, 2346.

substitution reaction is given by equation 5 and equation 6 defines the equilibrium and rate constants.

$$M + L \rightleftharpoons ML + H_2O \qquad \text{Eq. 5}$$

$$K_{f,l} = \frac{[ML]}{[M][L]} = \frac{k_{f,l}}{k_{r,l}} \qquad \text{Eq. 6}$$

where M is *fac*-$[Mn(CO)_3(H_2O)_3]^+$ and ML is *fac*-$[MnL(CO)_3(H_2O)_2]^+$.

Table 2.3: The kinetic data for *fac*-$[M(CO)_3(H_2O)_3]^+$ reactions with CH_3CN.

	fac-$[Mn(CO)_3(H_2O)_3]^+$	*fac*-$[Tc(CO)_3(H_2O)_3]^+$	*fac*-$[Re(CO)_3(H_2O)_3]^+$
K_l^{298}	4.5 ± 0.2	2.9 ± 0.1	4.8 ± 0.5
$\Delta H_{f,l}$ (kJ.mol^{-1})	-13.8 ± 1	-0.7 ± 0.8	-12.3 ± 1
$\Delta S_{f,l}$ (J.mol^{-1}.K^{-1})	-33.8± 5	+6.5 ± 3	-28.4 ± 4
$k_{f,l}^{298} \times 10^3$ (M^{-1}.s^{-1})	1750 ± 400	39.9 ± 1	0.76 ± 0.04
$k_i'^{298} \times 10^3$ (s^{-1})[c]	29000	665	13

[c] $k_i' = (k_{f,l}f)/(K_{os}n_c)$ with *f* as probability factor 12.

The kinetic data for the reaction between *fac*-$[M(CO)_3(H_2O)_3]^+$ and CH_3CN is presented in Table 2.3 while the data for the reaction with DMS is given in Table 2.4.

Table 2.4: The kinetic data for *fac*-$[M(CO)_3(H_2O)_3]^+$ reactions with DMS.

	fac-$[Mn(CO)_3(H_2O)_3]^+$	*fac*-$[Tc(CO)_3(H_2O)_3]^+$	*fac*-$[Re(CO)_3(H_2O)_3]^+$
K_l^{298}	25.2 ± 0.5	14.9 ± 0.1	8.3 ± 0.1
$\Delta H_{f,l}$ (kJ.mol^{-1})	-15.0 ± 0.7	-6.8 ± 0.3	
$\Delta S_{f,l}$ (J.mol^{-1}.K^{-1})	-23.3 ± 2	-0.3 ± 0.9	
$k_{f,l}^{298} \times 10^3$ (M^{-1}.s^{-1})	5340 ± 2000	60.8 ± 0.8	1.18 ± 0.06
$k_i'^{298} \times 10^3$ (s^{-1})[c]	89000	1010	20

In this investigation it was demonstrated that the water exchange and complex formation with soft and hard donors on group 7 tricarbonyl triaqua complexes has a small dependence on the nature of the entering ligand but is strongly dependent on the metal centre. An overall comparison of the work showed that the manganese water exchange rates were faster than the technetium rates which were again faster than the

rhenium rates. The mechanism showed a dissociative pathway and the transition state of the manganese was always positive.

Overall, very little work has been done in investigating the reactivity of *fac*-$[Mn(CO)^3]^+$ complexes towards substitution, opening the door for studies like this. These complexes could easily be used as models for Re (I) and Tc (I) tricarbonyl complexes.

2.6 History of Radiopharmaceuticals

Cancer is a disease or group of diseases where there is an uncontrollable growth and spread of abnormal cells. Death may be the result if the growth is not controlled. Both internal and external factors may lead to cancer. Table 2.5 lists these factors.[23]

Table 2.5: Factors that cause cancer growth.

Internal factors	External factors
Inherited mutations	Tobacco
Hormones	Chemicals
Immune conditions	Radiation
Mutations that occur from metabolism	Infectious organisms

The development of many cancers occurs over the years by multiple steps and the factors named above may act together to initiate carcinogenesis. Cancer is normally treated with surgery, radiation, chemotherapy, hormones and immunotherapy. The International Agency for Research and Cancer (IARC) reported the following cancer statistics:

- 12.7 million new cancer cases were reported in 2008 of which 5.6 million occurred in economically developed countries and 7.1 million occurred in economically developing countries.
- A total of 7.6 million deaths were reported in 2008 of which 28 million occurred in economically developed countries and 4.8 million occurred in economically developing countries.
- Cases are expected to increase by 2030, with an increase to 21.4 million cases globally and the death rate is expected to increase to 13.2 million cases per year.

[23] American Cancer Society, Global Cancer Facts and Figures 2nd Ed., 2011.

Radiopharmaceuticals are drugs that have been designed for *in vivo* applications. They have a radionuclide that is part of their composition and are administrated for diagnosis or the treatment of diseases in patients.[24,25] Besides the radionuclide, radiopharmaceuticals have a certain molecular structure; this is what determines the fate of the radiopharmaceutical administered in terms of where in the body it is delivered.

2.6.1. Radionuclides

A key part in the field of nuclear medicine is what is known as radionuclides. Some of these include ^{99m}Tc, ^{18}F and ^{131}I. The nuclear properties and the potential clinical applications are considered when the radionuclide is chosen. A target-specific radionuclide depends on receptor based radiopharmaceuticals for its delivery. Finding an appropriate radionuclide for radiotherapy depends on factors that include tumor uptake and retention, blood clearance, rate of radiation delivery, half-life and specific activity of the radionuclide, and the feasibility of large-scale production of the radionuclide. The selection of a radionuclide for a given targeting biomolecule is target-specific; in tumor radiotherapy it depends on availability and quality. The chosen radionuclide must have high specific activity since the tumor receptor sites are limited in number. This means the trace metal contaminants must be minimized in order to not have competition for receptor binding.[26] Some of the radionuclides that are used in radiotherapy are listed in Table 2.6.

[24] Morais, M., Paulo, A., Gano, L., Santos, I., Correia, J.D.G., *J. Organo. Chem*., **744**, 2013, 125.
[25] Wadsak, W., Mitterhauser, M., *Eur. J. Radiol*., **73**, 2010, 461.
[26] Liu, S., Adv. Drug. Deliv.Rev., **60**, 2008, 1347.

Table 2.6: Some of the radionuclides used in radiotherapy.

Nuclide	Half-life (days)	Energy (MeV)	Max Range (mm)	Gamma (keV)	Source
^{67}Cu	2.58	0.575	1.8	185 (40%)	Accelerator
^{90}Y	2.66	2.27	12.0	-	Generator
^{153}Sm	1.95	0.80	3.0	103 (28%)	Reactor
^{166}Ho	1.1	1.6	8.0	81 (6.3%)	Reactor or generator
^{177}Lu	6.7	0.497	1.5	208 (28%)	Reactor
^{186}Re	3.7	1.02	5.0	137 (9%)	Accelerator or reactor
^{188}Re	0.71	2.12	11.0	155 (15%)	Reactor generator

2.6.2 Radiolabeling and Bifunctional Chelates

Most of the clinically relevant radionuclides are metals. The radiometals used to label peptide-based radiopharmaceuticals are divided into four parts which are:

- The peptide that acts as a target-specific vector,
- the spacer,
- the bifunctional chelator and
- the radiometal.

The bifunctional chelate (BFC) consists of a chelating moiety to complex the radiometal and a functional group for attaching the peptide or spacer. The spacer can be a separator between the BFC and the peptide as a way to prevent the steric influence of the chelator on the binding affinity of the receptor. The spacer is dependent on the pharmacokinetic requirements of the radiopharmaceutical because this is a hydrophilicity influencer and can enhance the pharmacokinetics.[27]

[27] Fani, M., Maecke, H.R., *Eur. J. Nucl. Mol. Imaging*., **39**, 2012, S11.

2.7 PET and SPECT

Emission tomography (ET) is a form of medical imaging that is based on the tracer principle that was developed by George de Hevesy in the early 1900s. ET can be divided into two main techniques: Positron emission tomography (PET) and single-photon emission computed tomography. Radiopharmaceuticals in ET are designed to act as markers to yield valuable diagnostic information.[28]

2.7.1 Positron Emission Tomography

Positron emission spectroscopy is the generation of images based on how positron emitters are distributed *in vivo*. Gamma rays go through what is known as positron decay. PET relies on the detection of the gamma rays by detectors which are in coincidence that surround the patient. PET relies on the annihilation of positrons. These positrons travel through human tissue and release kinetic energy until it reaches thermal energies and interact with electrons. This leads to the formation of a hydrogen-like orbiting pair called positronium which is unstable and decays into a pair of anti-parallel 511-keV photons. An advantage of PET is its high sensitivity and the results of the sensitivity are as follows:[29]

- The signal-to-noise ratio is improved and therefore improving image quality,
- with an increase in sensitivity, then there is a possibility to acquire shorter scans and
- since shorter scans can be acquired due to this sensitivity, multiple scans can be performed on a patient at different fields of view.

PET radionuclides are signallers attached to a vehicle molecule and are positron emitting. The most widely used PET nuclides have short lives and have limited availability.[2] In Table 2.7 some of the radionuclides used in PET is listed. The selection of PET radionuclides depends on the following consideration:

- Radionuclide availability,
- radionuclide physical characteristics,
- radiochemical issues and
- radiopharmacological issues.

[28] Wernick, M.N., Aarsvold, J.N., Emission Tomography: The Fundamentals of PET and SPECT, *Elsevier Academic Press*, 2004, 179.
[29] Rahmin, A., Zaidi, H., *Nucl. Med. Comm.,* **29**, 2008, 193.

Table 2.7: Radionuclides used in PET.

Radionuclide	Half-life (hours)	Decay mode	$E_{\beta+}$ (keV)	Production mode
^{18}F	1.83	β^+ (97%)	634 (97%)	Cyclotron
		EC (3%)		
^{68}Ga	1.13	β^+ (89%)	1899 (88%)	$^{68}Ge/^{68}Ga$ generator
		EC (11%)		
^{64}Cu	12.7	β^+ (19%)	656 (18%)	Cyclotron
		β^- (40%)		
		EC (41)		
^{86}Y	14.7	β^+ (33%)	1221 (12%)	Cyclotron
		EC (66%)		
^{124}I	99.6	β^+ (23%)	3160 (24%)	Cyclotron
		EC (77%)	2556 (25%)	

2.7.2 Single-Photon Emission Computed Tomography

Single-photon emission computed tomography (SPECT) involves the use of radiopharmaceuticals labelled with a single-photon emitter. A gamma-ray photon is emitted with every radioactive decay event. These gamma-rays are imaged using a collimator which is a thick sheet of a heavy material. Certain rays travel in one direction and these rays are selected by the collimator in order to form an image of the radiopharmaceutical distribution. The other gamma-rays travelling in a different direction are blocked by the channel walls or missed by the collimator entirely. A scintillator is used to detect the gamma-rays.[5]

SPECT diagnostic radionuclides are often gamma-emitting isotopes. These generator-produced radiometals prove to be ideal since the daughter radionuclide can be easily separated from the parent isotope by ionic chromatography. The most widely used isotope in SPECT is ^{99m}Tc due to its low cost and optimal nuclear properties. ^{111}In is useful for gamma and SPECT imaging.[3] Table 2.8 lists some of the SPECT radionuclides in use.

Table 2.8: Radionuclides used in SPECT.

Radionuclide	Half-life (hours)	Decay mode	E_γ(keV)	Production mode
^{99m}Tc	6.02	IT (100%),γ	141 (91%)	Cyclotron
^{111}In	67.9	Auger,γ	171 (90%)	^{68}Ge/^{68}Ga generator
		EC (100%)	245 (94%)	
^{67}Ga	78.26	EC (100%)	93 (39%)	Cyclotron
		Auger, γ	185 (21%)	
^{123}I	13.2	EC (100%), γ	159 (84%)	Cyclotron

2.8 Radiopharmaceutical Imaging Agents with Tc

Technetium complexes account for the majority of the radiopharmaceuticals used for imaging. ^{99m}Tc is mainly used due to its impressive nuclear properties, low cost and availability from commercial Mo^{99}/Tc^{99m} generators. Technetium radiopharmaceuticals, especially those in clinical use, have a $[Tc^{99m}(O)]^{3+}$ core and are known as either perfusion agents or target-specific radiopharmaceuticals. In perfusion agents the biological distribution of the radiopharmaceuticals is determined by blood flow while in target-specific radiopharmaceuticals it is determined by the ligand-target interactions.[5] Radiopharmaceuticals need to possess the following properties in order to be applicable:

- Low molecular weight,
- moderate lipophilicity,
- neutral charge and
- high specificity and selectivity for one receptor.

These properties are important in order for the molecules to pass the brain-blood-barrier (BBB).

2.8.1 'First-generation' Radiopharmaceuticals

First generation radiopharmaceuticals are perfusion agents that have a ligand system that is biologically inactive without the metal centre. These are referred to as *de novo* compounds. The first generation radiopharmaceuticals are prepared using 'instant kits' and the addition of permetallate before *in vivo* injection. The field where these first

generation radiopharmaceuticals are administered depends on their physiochemical properties such as hydrophilicity, charge and the size of the complex. These physical properties are what determine the biological distribution between tissues. The three most widely applied technetium radiopharmaceuticals are Tc-HMPAO, Tc-MAG_3 and Tc-Sestamibi.[25]

2.8.1.1 Brain Imaging

^{99m}Tc coordination chemistry plays a role in perfusion agents and as well as the labelling of central nervous system receptor ligands. The Tc-HMPAO radiopharmaceutical is a technetium complex that is used in brain imaging (Figure 2.3). It contains a hexamethylpropyleneamineoxime (HMPAO) ligand and a $[Tc(O)]^{3+}$ core. It has the ability to be taken up by the brain and be retained there for long hours by intracellular conversion. Tc-HMPAO is lipophilic and is able to pass the blood brain barrier (BBB) and has been developed to measure brain perfusion in strokes and dementia.[30]

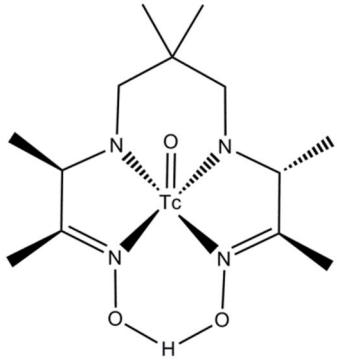

Figure 2.3: Illustration of Tc-HMPAO.

Another example of a brain imaging agent is [^{99m}TcO(ECD)]. It is highly lipophilic and is also known as Neurolite. The structure of Neurolite is given in Figure 2.4.

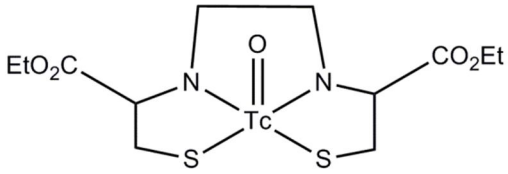

Figure 2.4: Illustration of Neurolite.

[30] Jurrison, S., Berning, D., Jia, W., Ma, D., *Chem. Rev.*, **93**, 1993, 1137.

2.8.1.2 Kidney Imaging

A well investigated field is the imaging of the kidney. The agents used are complexes of aminoacetic acids that are bound to technetium. Tc-MAG_3 is a renal imaging agent that is injected and its passage through the kidneys are monitored. This complex has good *in vivo* characteristics and has no chiral centre.[26] An illustration of Tc-MAG_3 is given in Figure 2.5.

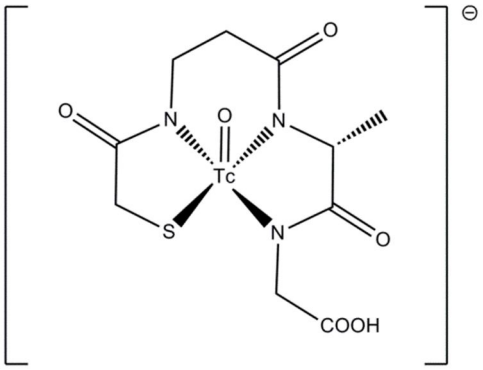

Figure 2.5: Illustration of Tc-Mag_3.

2.8.1.3 Heart Imaging

Imaging agents used for the heart are lipophilic and unipositively charged complexes. A successful agent is ^{99m}Tc-sestamibi (Figure 2.6), which is also known as cardiolite and is a myocardial perfusion imaging agent with a cationic octahedral orientation. Cardiolite is used to evaluate the normal and abnormal myocardium in patients with suspected myocardial infarction. Tc-Sestamibi was also used for tumor imaging as well as lung cancer detection in its early stages of research.[6]

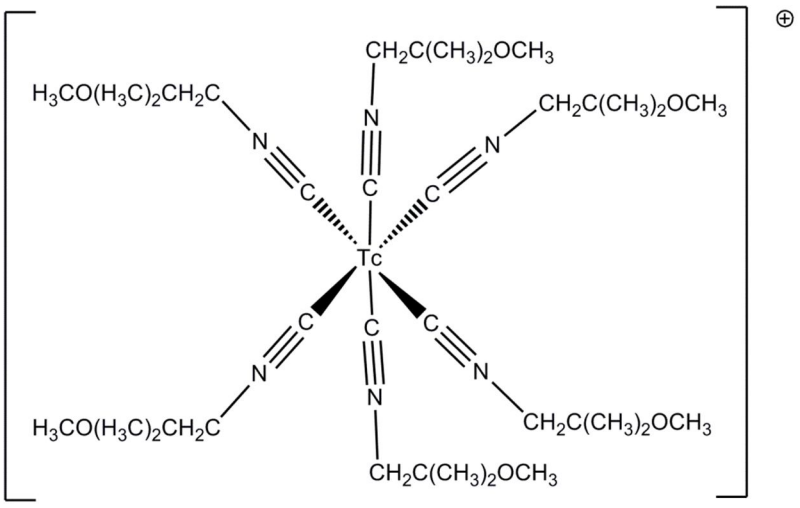

Figure 2.6: Illustration of Tc-Sestamibi.

$[^{99m}Tc(DMPE)_2Cl_2]^+$ (Figure 2.7) is a technetium complex that was developed for heart imaging but was found to undergo reduction *in vivo*, losing its positive charge and this causes the complex to be washed out of the heart and accumulate in the liver.

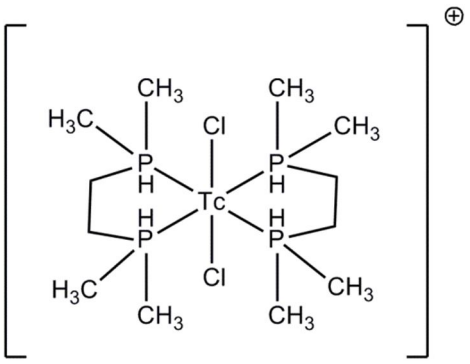

Figure 2.7: Illustration of $[^{99m}Tc(DMPE)_2Cl_2]^+$.

Another heart imaging agent is ^{99m}Tc-NOET, this technetium complex is neutral and is commercially available. The structure of ^{99m}Tc-NOET is given in Figure 2.8.

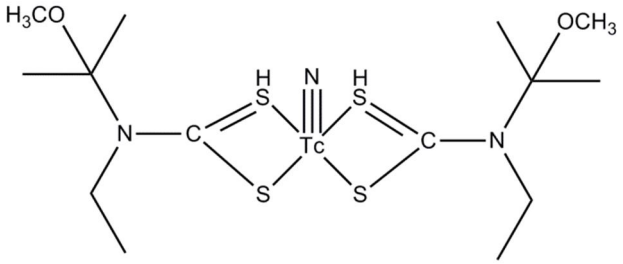

Figure 2.8: Illustration of ^{99m}Tc-NOET.

2.8.2 'Second Generation' Radiopharmaceuticals

The 'first generation' radiopharmaceuticals are used as precursors for the synthesis of 'second generation' radiopharmaceuticals. The preparation is carried out *via* bifunctional chelators (BFC). 'Second generation' radiopharmaceuticals are target-specific which means they bind to a specific receptor. The three most common BFCs used are diethylenetriaminepentacetic acid (DTPA), 1,4,7,10-tetraazacyclododecane-1,4,7,10-tetraacetic acid (DOTA) and 3,6,10,13,15,18-hexaazabicyclo[6,6,4] octadecane (SAR). The functions of the ligands are covalent binding to a radioactive precursor and the conjugation to a biovector. Examples of biovectors are peptides, proteins or pharmacophores. One of the challenges in the preparation of the 'second generation' radiopharmaceuticals is binding the radioactive precursor tightly while trying

not to change the *in vivo* behaviour of the biovector. The radiopharmaceutical biodistribution can be influenced by the use of a biovector and chelated metal center linker.[4] Figure 2.9 illustrates the bifunctional chelates used in second generation radiopharmaceuticals.

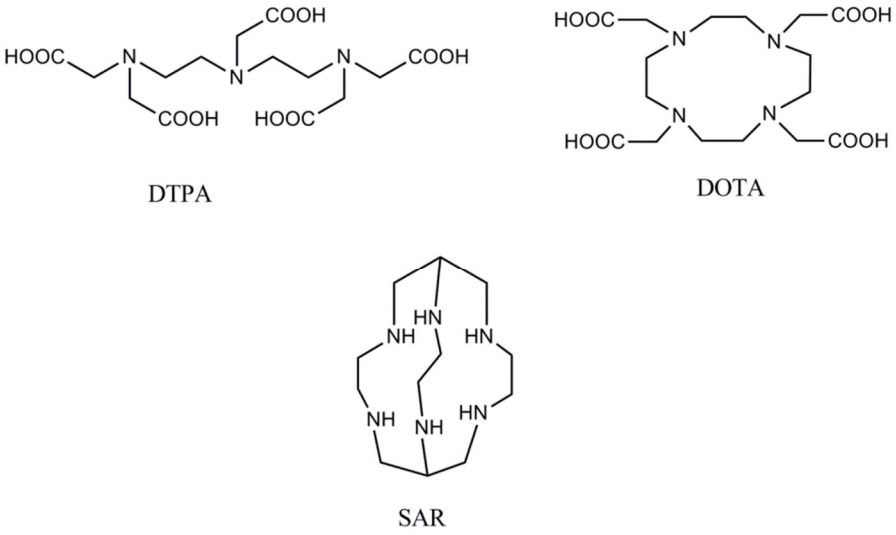

Figure 2.9: Illustration of the bifunctional chelates used in second generation radiopharmaceuticals.

2.8.3 Multidrug Resistance (MRD1) Targeting Molecules

The resistance of chemotherapeutic agents by tumors is a pathological state known as multidrug resistance. It is known as one of the primary reasons for cancer treatment failure in patients. MDR is characterized using the overexpression of P-glycoprotein (Pgp), which is a transmembrane pump that transports cytotoxic materials out of the cells. MDR has been known to affect a wide range of compounds that are lipophilic and monocationic at physiologic pH. MDR modulators have been developed in order to block the actions of Pgp by re-establishing the cytotoxic effects of chemotherapeutic agents in tumor cells. This is done by administering them simultaneously. The three ^{99m}Tc myocardial perfusion agents (^{99m}Tc-sestamibi,^{99m}Tc-tetrofosmin and ^{99m}Tc-furifosmin) are all lipophilic monocations that have been evaluated for the potential use in diagnosing and monitoring multidrug resistance. ^{99m}Tc-furifosmin has shown higher effectiveness in transporting the MDR substrates. [31]

[31] Jurrison, S.S., Lydon, J.D., *Chem. Rev.,* **99**, 1999, 2205.

2.8.4 Labeling with ^{99m}Tc

The type of approach used for ^{99m}Tc-labeling depends on the biomolecule and the purpose of the study. Peptides can be labelled with ^{99m}Tc using an approach known as post-conjugation labelling. The strategy of the approach consists of:

- The preparation of the bifunctional chelator-peptide conjugate,
- the addition of a buffer, reducing agent and supporting ligand,
- lyophilisation and
- addition of the generator eluate ($^{99m}TcO_4^-$).

The BFC's with a very high attraction and selectivity to technetium in any of its oxidation states are used for high specific activity to be achieved. The Tc-labelled BFC peptide must be stable thermodynamically and be kinetically inert in order to survive the physiological conditions. Three different types of labelling will be discussed in the next few paragraphs.

2.8.4.1 Direct Labeling

In direct labeling, a reducing agent is used to convert the disulphide linkages into free thiols that can bind strongly to the technetium. This is a relatively easy approach but only applies to antibodies or antibody fragments because the small biomolecules do not possess any disulphide bonds.

2.8.4.2 Pre-labeling

The pre-labeling approach is a successful approach used in labelling antibodies and their fragments with ^{99m}Tc. It involves the formation of a ^{99m}Tc-BFC chelate and a separate step of the conjugation of the chelate to a biomolecule (BM). The targeting biomolecule in this approach is not exposed to harsh conditions in the chelation step and the pre-labeling approach is useful in demonstrating the proof of the concept in a short period of time before extensive efforts in the BFC-BM conjugate preparation (Figure 2.10). The disadvantage is that it is too complex and time consuming for routine clinical use and the kit formulation development is difficult.

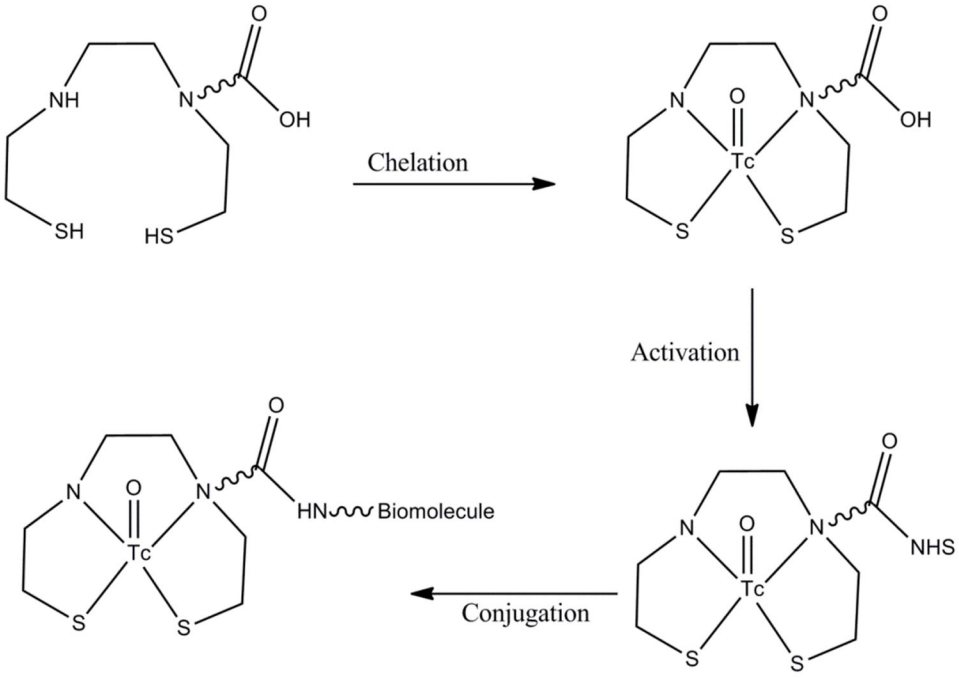

Figure 2.10: The bifunctional chelates used in Pre-labeling.

2.8.4.3 Post-labeling

The post-labeling approach is an indirect method in which a BFC is first attached to the biomolecule to form a BFC-biomolecule conjugate. Radiolabeling is accomplished by the direct reduction of [$^{99m}TcO_4^-$] in the presence of enough BFC-biomolecule conjugate or by ligand exchange with an intermediate ^{99m}Tc complex (Figure 2.11). This is the most practical approach used for kit formulation and mostly used for the development of commercial products.

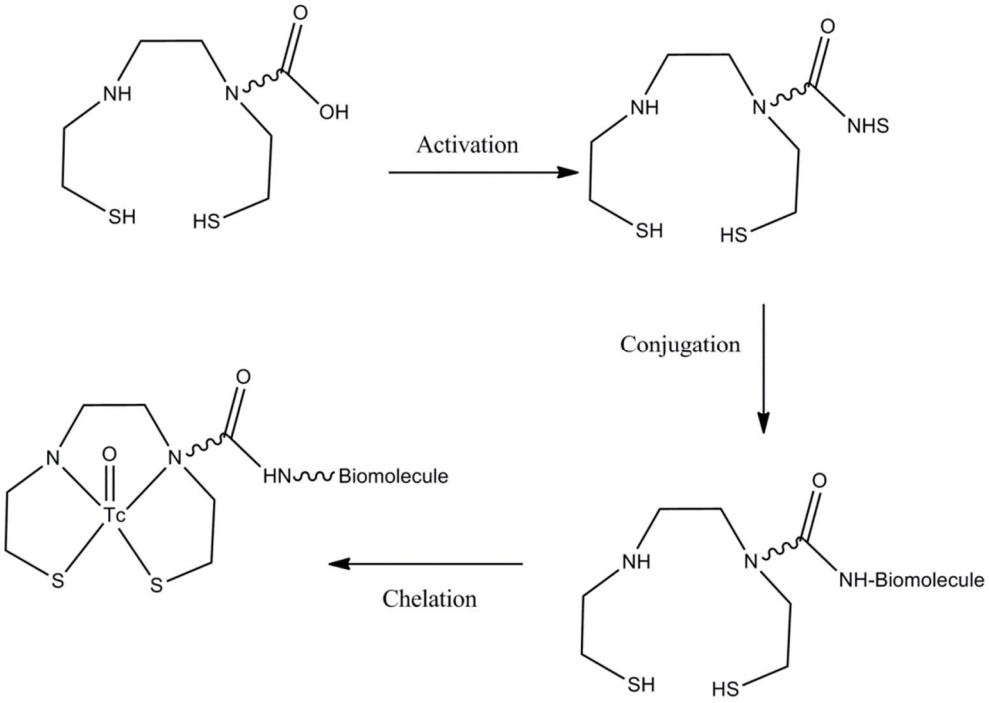

Figure 2.11: The bifunctional chelates used in post-labeling.

2.9 Rhenium Radiopharmaceuticals

The two widely used rhenium radionuclides for targeted therapy are ^{186}Re and ^{188}Re. ^{186}Re has a half-life of 90 hours while ^{188}Re has a half-life of 17 hours and both can be prepared in nuclear reactors that have adequate specific activities by using enriched targets. Rhenium possesses the same chemical properties as technetium as they are both in the same group on the periodic table. Rhenium radiopharmaceuticals are analogous to technetium pharmaceuticals but the rhenium complexes are more difficult to prepare.[32]

2.9.1 ^{188}Re-HEDP

^{188}Re-1,1-hydroxyethylidene-diphosphonate (^{188}Re-HEDP) was recognized as a potential radiotherapeutic agent in bone metastases treatment in the late 1980s. In one of its studies of disseminated prostate cancer, it was discovered it had pain improvement properties.[33] It has also been used as a bone seeking agent and its palliation properties were once again observed in bone metastases.[17]

[32] Kothari, K., Pillai, M.R.A., Unni, P.R., Shimpi, H.H., Noronha, O.P.D., Samuel, A.M., *Appl. Radiat. Isot*., 1999, 51.
[33] Goyal, J., Antonarakis, E.S., *Cancer Lett*., **323**, 2012, 135.

2.9.2 ^{188}Re(V)-DMSA

^{188}Re(V)-DMSA has been studied as a diagnostic and therapeutic agent.[34] It is synthesized by a simple kit method and in its preliminary studies, it showed an uptake for bone metastases and is therefore an excellent agent for the treatment of bone pain caused by bone lesions.[35] Dimercaptosuccinic acid (DMSA) can exist in two diastereoisomeric forms, *meso* and *racemic (rac)*. The meso-2,3-DMSA isomer has been approved by the Food and Drug Administration (FDA) for lead intoxication treatment, while the racemic isomer has not been studied much as a radiopharmaceutical; it is very soluble in water, strongly acidic solutions and organic solvents.

[34]Park, J., Lee, T., Choi, T., Cheon, G., Choi, C., Awh, O., *Nucl. Med. Biol.,* **34**, 2007, 1029.
[35] Garćia-Salinas, L., Ferro-Flores, G., Arteaga-Murphy, C., Pedraza-López, M., Hernández-Gutiérrez, S., Azorín-Nieto, J., *Appl. Rad. Iso.,* **54**, 2001, 413.

3 THE SYNTHESIS OF MANGANESE (I) COMPLEXES

3.1 Introduction

The environment around a metal is one of the important aspects in the design of radiopharmaceuticals.[1] Various studies have been performed on the elements in the manganese triad. Technetium (I) and rhenium (I) triaqua tricabonyl complexes became important precursors in the design of potential radiopharmaceuticals and are currently under development. In literature rhenium (I) complexes are observed to be two orders of magnitude slower than technetium (I) and four orders of magnitude slower than manganese (I) complexes in kinetic experiments.[2,3] Usón *et. a.l.*[11] reported on the isomerization of tricarbonyl and dicarbonyl manganese (I) complexes and it was found that the isomerization of neutral complexes differ from the cationic complexes. In the case of cationic complexes, the isomerization is from *fac* - *mer* and does not form other isomers. For the neutral complexes, *cis* isomers are formed. These complexes isomerise from *fac* to *mer* then *cis* compounds.

In this study a comparison between the reactivity of rhenium (I) tricarbonyl aqua complexes and manganese (I) tricarbonyl aqua complexes is made. Up to date about two Mn (I) aqua complexes with N,N'-bidentate ligands have been synthesized and are reported on the Cambridge Structural Database (CSD).[4] The first structure *fac*-$[Mn(CO_3)(N,N,N',N'\text{-}1,1,4,4\text{-}(CH_3)_4en)(H_2O)]$ is reported by Horn *et al.*[5] and consists of three facial carbonyl ligands, a substituted ethylene diamine ligand and the aqua ligand octahedrally spaced around the Mn (I) core. The second structure *fac*-$[Mn(CO)_3(N=C(CH_3)dmpz\text{-}k^2N,N)(H_2O)]$[6] by Anton *et. al* has three *facial* carbonyl ligands an aqua ligand and a N,N'-bidentate ligand coordinated to the Mn (I) core to complete the octahedral arrangement.

---

[1] Alberto, R., *Eur. J. Inorg. Chem.*, 2009, 21.
[2] Helm, L., *Coord. Chem. Rev.*, **252**, 2008, 2346.
[3] Prinz, U., Koelle, U., Ulrich, S., Merbach, A.E., Maas, O., Hegetschweiler, K., *Inorg. Chem.*, **43**, 2004, 2387.
[4] Cambridge Structural Database (CSD), Version 5.34, Nov 2012 update. Allen F.H., *Acta Cryst.*, **B58**, 2002, 380. Date Accessed : October 2013.
[5] Horn, E., Horiuchi, A., *Z. Kristallogr., New Cryst. Struct.*, **216**, 2001, 73.
[6] Antón, N., Arroyo, M., Gómez-Iglesias, P., Miguel, D., Villafañe, F., *J. Organomet. Chem.*, **693**, 2008, 3074.

Several Mn (I) tricarbonyl structures have been reported with other ligand systems, other than the aqua ligand) in the 6th position, namely:

- *fac*-[$Mn(CO)_3$(Bipy) (η^1-pyS)][7],
- *fac*-[$Mn(CO)_3$(Bipy)Cl][8],
- *fac*-[$Mn(CO)_3$(Phen)(tert-butyl iso)][9] and
- *fac*-[$Mn(CO)_3$(Phen)(CF_3SO_3)].[10]

The crystal structures of these complexes will be discussed in Chapter 4 and will be compared to the stuctures reported here.

Usón *et al*.[11] reported several tricarbonyl and dicarbonyl complexes of manganese (I) using various ligands of which *fac*-[$Mn(CO)_3(C_3H_6O)_3$] is one of the important complexes for this study. This work extends on the work by Usón *et al.* by the addition of bidentate ligands and exchanging the acetone ligand with water and methanol.

A comparison with rhenium (I) aqua complexes will be conducted with complexes synthesised by G. Kemp[12] (*fac*-[$Re(CO)_3$(Bipy)H_2O], *fac*-[$Re(CO)_3$(Phen)H_2O] and *fac*-[$Re(CO)_3$(Pico)H_2O]) and those synthesised by Schutte *et al*.[13] (*fac*-[$Re(CO)_3$(2,4-Quin)H_2O] and *fac*-[$Re(CO)_3$(Flav)H_2O]). The ligand systems used in this study is illustrated in Scheme 3.1.

In this chapter, the synthesis and characterization of Mn (I) tricarbonyl aqua complexes are discussed. Four types of characterization methods were used: IR, NMR, UV-vis and XRD. The aim of the study is to see the effect that N,N'-,N,O- and O,O'-bidentate ligands have on the *fac*-$[Mn(CO)_3]^+$ core.

---

[7] Ara, G., Kabir, S.E., Kundu, K., Malik, K.M.A., *J. Chem. Cryst*., **33**, 2003 851.
[8] Horn, E., Snow, M.R., Tiekink, E.R.T., *Acta Cryst*. **C43**, 792, 1987.
[9] Valín, M.L., Moreiras, D., Solans, X., Font-Altaba, M., García-Alonso, F.J., *Acta Cryst*. **C42**, 1986, 417.
[10] Pereira, C., Ferreira, H.G., Schultz, M.S., Milanez J., Izidoro M, Leme P.C., Santos, R.H.A., Gambardella, M.T.P., Castellano, E.E., Lima-Neto, B.S., Carlos, R.M., *Inorg. Chim. Acta*. **358**, 2005 3735.
[11] Usón, R., Riera, V., Gimeno, J., Laguna, M., Gamasa, M.P., *J. Chem. Soc. Dalton Trans.*, 996, 1979.
[12] Kemp, G., PhD dissertation, University of Johannesburg, 2006.
[13] Schutte, M., Kemp, G., Visser, H.G., Roodt, A., *Inorg. Chem*., **50(24)**, 2011, 12486.

Scheme 3.1: Illustration of the N,N'-, N,O- and O,O'-bidentate ligands used in this study

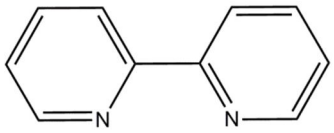

2,2'-Bipyridyl (Bipy)

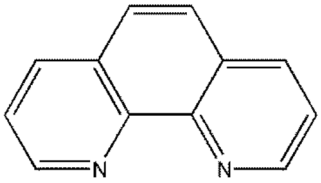

1,10-Phenanthroline (Phen)

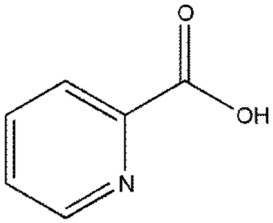

Picolinic acid (Pico)

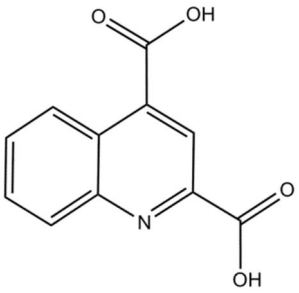

Quinoline-2,4-dicarboxylic acid (2,4-Quin)

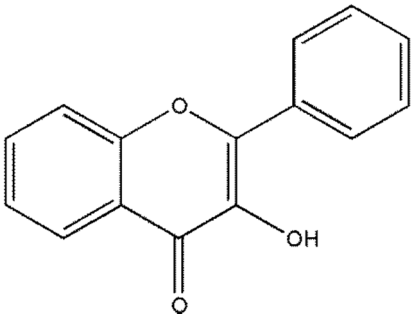

3-Hydroxyflavone (Flav)

3.2 Apparatus and Chemicals Used

The reagents used for synthesis and characterization were purchased from Sigma-Aldrich, South Africa, unless stated otherwise. These reagents were used as purchased. Quinoline-2,4-dicarboxylic acid was purchased from Merck, South Africa, and methanol-d_4 and acetone-d_6 were purchased from Cambridge Isotope Laboratories, Inc. All UV-vis measurements were collected using a Varian Cary 50 Conc UV-Visible spectrophotometer, equipped with a Julabo F12-mV temperature cell regulator (accurate within 0.1°C) in a 1.000 ± 0.001 cm quartz cuvette cell. The NMR spectra were obtained on a Bruker Avance II 600 MHz and Bruker DVX 300 MHz spectrometers. The chemical shifts are reported in ppm relative to TMS using methanol-d_4 (3.31 ppm and 4.71 ppm, 49.15 ppm), acetone-d_6 (2.05 ppm, 29.92 ppm and 206.68 ppm) and DMSO-d_6 (2.54 ppm, 40.45 ppm). All infrared spectra were

recorded on a Bruker Tensor 27 Standard System spectrophotometer with a laser range of 4000 – 370 cm^{-1}.

3.3 Synthesis

All procedures were performed in the dark while all the N,O-bidentate complexes were synthesized under nitrogen gas. It is assumed that the aqua complexes form methanol complexes when dissolved in methanol.[14,15] The carbonyl peaks for these complexes are not reported because of the long relaxation times as well as the low solubility of the complexes, however, the presence of the carbonyl ligands are clear in all the IR spectra. Also, the triflate anion is not always detected.

3.3.1. Synthesis of *fac*-[$Mn(CO)_3(Bipy)(H_2O)][CF_3SO_3$]

$Mn(CO)_5Br$ (0.2753 g, 1 mmol) was dissolved in 20 mL acetone. $AgCF_3SO_3$ (0.3110 g, 1.2 mmol) dissolved in 20 mL acetone was added to the mixture and stirred for 45 hours at room temperature. A precipitate (AgBr) formed; it was filtered off and weighed (0.0468 g, 0.25 mmol). The yellow solution was dried under vacuum and a yellow oil formed. 2,2'-Bipyridyl (0.1760g, 1.1 mmol) was dissolved in 10 mL water and was added to the yellow oil and the reaction was refluxed for 24 hours at 110 °C. The dark orange solution was then cooled down to room temperature and left to stand to form crystals. Orange-red cuboidal crystals were obtained.

UV/vis: λ_{max} = 395 nm, ε = 1460 M^{-1} cm^{-1}.

IR (KBr, cm^{-1}): υ_{CO}= 2040, 1933.

^{1}H NMR (300 MHz, Acetone-d_6): δ = 9.45 (dd, 2H, *J* = 16.1Hz, 5.4Hz), 8.76 (dd, 2H, *J* = 8.1 Hz, 1.2 Hz), 8.46 (tt, 2H, *J* = 8.2 Hz, 5.1 Hz), 7.93 (tt, 2H, *J* = 8.2 Hz, 5.1 Hz).

^{13}C NMR (151 MHz, Acetone-d_6): δ = 125.05, 129.15, 142.22, 155.90, 157.91.

Yield: 0.060 g, 22%.

3.3.2. Synthesis of *fac*-[$Mn(CO)_3(Bipy)(MeOH)][CF_3SO_3$]

fac-$[Mn(CO)_3(Bipy)H_2O][CF_3SO_3]$ was dissolved in methanol (10 mL) and the solution was stirred for 10 minutes at room temperature. The solution was dried and a yellow precipitate formed.

UV/vis: λ_{max} = 402 nm, ε = 1140 M^{-1} cm^{-1}.

IR (KBr, cm^{-1}): υ_{CO}= 2038, 1941.

---

[14] Brink, A., Visser, H. G., Roodt, A., *J. Coord. Chem.,* **64**, 2011, 122.
[15] Grundler, P. V., Salignac, B., Cayemittes, S., Alberto, R., Merbach, A. E., *Inorg. Chem.*, **43**, 2004, 865.

^{1}H NMR (600 MHz, Acetone-d_6): δ = 9.75 (dd, 2H, *J* = 16.1Hz, 5.4Hz), 8.99 (dd, 2H, *J* = 8.1 Hz, 1.2 Hz), 8.35 (tt, 2H, *J* = 8.2 Hz, 5.1 Hz), 8.23 (tt, 2H, *J* = 8.2 Hz, 5.1 Hz), 3.78 (s, 3H).

^{13}C NMR (151 MHz, Acetone-d_6): δ = 126.43, 127.63, 130.26, 139.51, 155.03.

3.3.3. Synthesis of *fac*-[Mn(CO)$_3$(Bipy)(Br)]

fac-[Mn(CO)$_3$(Bipy)H$_2$O][CF_3SO_3] was dissolved in a 0.2 M solution of NaBr in methanol and the solution was stirred overnight at room temperature. The solution was dried and an orange precipitate formed.

UV/vis: λ_{max} = 445 nm, ε = 461 M^{-1} cm^{-1}.

IR (KBr, cm^{-1}): υ_{CO}= 2025, 1894.

^{1}H NMR (600 MHz, Acetone-d_6): δ = 9.65 (dd, 2H, *J* = 8.0 Hz, 1.1 Hz), 8.83 (dd, 2H, *J* = 8.1 Hz, 1.2 Hz), 8.26 (tt, 2H, *J* = 5.1 Hz, 8.2 Hz), 8.11 (tt, 2H, *J* = 5.1 Hz, 8.2 Hz).

^{13}C NMR (151 MHz, Acetone-d_6): δ = 125.62, 127.24, 130.26, 137.75, 154.25.

3.3.4. Synthesis of *fac*-[Mn(CO)$_3$(Bipy)(Py)][CF_3SO_3]

fac-[Mn(CO)$_3$(Bipy)H$_2$O][CF_3SO_3] was dissolved in a few drops pyridine and the solution was stirred overnight at room temperature. The solution was dried and an orange yellow precipitate formed.

UV/vis: λ_{max} = 370 nm, ε = 626 M^{-1} cm^{-1}.

IR (KBr, cm^{-1}): υ_{CO}= 2023, 1924.

^{1}H NMR (600 MHz, Acetone-d_6): δ = 10.02 (dd, 2H, *J* = 5.1 Hz, 1.2 Hz), 9.02 (dd, 2H, *J* = 8.1 Hz, 1.2 Hz), 8.58 (tt, 2H, *J* = 6.5 Hz, 8.2 Hz), 8.35 (tt, 2H, *J* = 8.2 Hz, 5.1 Hz), 8.32 (t, 1H, J = 9.6 Hz), 7.83 (tt, 2H, *J* = 7.6 Hz, 1.5 Hz), 7.33 (tt, 2H, *J* = 7.5 Hz, 6.6 Hz).

^{13}C NMR (151 MHz, Acetone-d_6): δ = 126.17, 127.09, 127.78, 130.51, 139.46, 146.33, 152.57, 155.23.

3.3.5. Synthesis of *fac*-[Mn(CO)$_3$(Bipy)(TU)][CF_3SO_3]

fac-[Mn(CO)$_3$(Bipy)H$_2$O][CF_3SO_3] was dissolved in a 0.2 M solution of thiourea in methanol and the solution was stirred overnight at room temperature. The solution was dried and an yellow precipitate formed.

UV/vis: λ_{max} = 365 nm, ε = 538 M^{-1} cm^{-1}.

IR (KBr, cm^{-1}): υ_{CO}= 2030, 1925.

^{1}H NMR (600 MHz, Acetone-d_6): δ = 9.65 (dd, 2H, *J* = 5.0 Hz, 1.0 Hz), 8.94 (dd, 2H, *J* = 27.3 Hz, 13.6 Hz), 8.35 (tt, 2H, *J* = 6 Hz, 7.2 Hz), 8.20 (tt, 2H, *J* = 21.7 Hz, 10.9 Hz), 6.91 (s, 4H).

^{13}C NMR (151 MHz, Acetone-d_6): δ = 126.34, 127.61, 130.56, 138.49, 146.21, 154.12, 181.04, 185.55.

3.3.6. Synthesis of *fac*-[Mn(CO)$_3$(Phen)(H$_2$O)][CF$_3$SO$_3$]

$Mn(CO)_5Br$ (0.2753 g, 1 mmol) was dissolved in 20 mL acetone. $AgCF_3SO_3$ (0.3113 g, 1.2 mmol) dissolved in 20 mL acetone was added to the mixture and stirred for 45 hours at room temperature. A yellow solution with a grey precipitate formed. AgBr was filtered off and the precipitate was weighed (0.0450 g, 0.23 mmol). The filtrate was dried under vacuum and a yellow oil formed. 1,10'-Phenanthroline (0.1810 g, 1 mmol) was dissolved in 10 mL water and added to the yellow oil and the reaction mixture was refluxed for 24 hours at 110°C. The dark orange solution was then cooled down to room temperature and left to stand to form crystals. Orange needle-like crystals were obtained.

UV/vis: λ_{max} = 396 nm, ε = 1148 M^{-1} cm^{-1}.

IR (KBr,cm^{-1}): 2041, 1940.

^{1}H NMR (300 MHz, Acetone-d_6): δ = 9.70 (dd, 2H, *J* = 5.1 Hz,1.3Hz), 8.91 (dd, 2H, *J* = 8.3 Hz,1.3 Hz), 8.26 (d, 2H, *J* = 4.7 Hz), 8.15 (dd, 2H, *J* = *8*.3 Hz, 5.1 Hz).

^{13}C NMR (151 MHz, Acetone-d_6): δ = 126.04, 127.34, 130.40, 139.21, 146.77, 154.44.

Yield: 0.0712 g**,** 26%.

3.3.7. Synthesis of *fac*-[Mn(CO)$_3$(Phen)(MeOH)][CF$_3$SO$_3$]

fac-$[Mn(CO)_3(Phen)(H_2O)][CF_3SO_3]$ was dissolved in methanol (10 mL of a 0.5 × 10^{-3} M solution) and the solution was stirred overnight at room temperature. The solution was dried and a yellow-orange precipitate was formed.

UV/vis: λ_{max} = 405 nm, ε = 2000 M^{-1} cm^{-1}.

IR (KBr, cm^{-1}): υ_{CO}= 2025,1894 .

^{1}H NMR (600 MHz, Acetone-d_6): δ = 9.80 (dd, 2 H,*J* = 2.8 Hz,2.1Hz), 9.03 (dd, 2H, *J* = 8.2 Hz,1.3 Hz), 8.39 (d, 2H, *J* = 7.1 Hz), 8.27 (dd, 2H, *J* = *8*.2 Hz, 5.1 Hz), 3.80 (s, 3H).

^{13}C NMR (151 MHz, Acetone-d_6): 126.43, 127.59, 130.31, 139.47, 147.43, 155.03.

3.3.8. Synthesis of *fac*-[Mn(CO)$_3$(Phen)(Br)]

fac-[Mn(CO)$_3$(Phen)(H$_2$O)][CF$_3$SO$_3$] was dissolved in a 0.2 M solution of NaBr in methanol and the solution was stirred overnight at room temperature. The solution was dried and an orange precipitate formed.

UV/vis: λ_{max} = 370 nm, ε = 584 M^{-1} cm^{-1}.

IR (KBr, cm^{-1}): υ_{CO}= 2017, 1907.

^{1}H NMR (600 MHz, Acetone-*d$_6$*): δ = 9.67 (dd, 2H, *J* = 4.0 Hz), 8.85 (dd, 2H, *J* = 7.1Hz), 8.28 (dd, 2H, J = 8.2 Hz, 5.1 Hz), 8.13 (dd, 2H, *J* = *8*.1 Hz, 5.1 Hz).

^{13}C NMR (151 MHz, Acetone-*d$_6$*): δ = 125.44, 126.38, 130.77, 141.41, 148.23, 155.47.

3.3.9. Synthesis of *fac*-[Mn(CO)$_3$(Phen)(Py)][CF$_3$SO$_3$]

fac-[Mn(CO)$_3$(Phen)(H$_2$O)][CF$_3$SO$_3$] was dissolved in a few drops of pyridine and the solution was stirred overnight at room temperature. The solution was dried and a yellow precipitate formed.

UV/vis: λ_{max} = 370 nm, ε = 707 M^{-1} cm^{-1}.

IR (KBr, cm^{-1}): υ_{CO}= 2025, 1932.

^{1}H NMR (300 MHz, Acetone-*d$_6$*): δ = 10.05 (dd, 2 H), 9.06 (dd, 2H, *J* = 6.5 Hz), 8.59 (d, 2H, *J* = 24.3 Hz), 8.31 (dd, 2H, *J* = 46.5 Hz), 8.61 (d, 2H, *J* = 24.3 Hz), 7.80 (d, 1H, *J* = 37.8 Hz), 7.35 (s, 2H).

^{13}C NMR (151 MHz, Acetone-*d$_6$*): δ = 126.21, 127.26, 127.78, 127.93, 139.51, 145.56, 145.69, 152.72, 155.35.

3.3.10. Synthesis of *fac*-[Mn(CO)$_3$(Phen)(TU)][CF$_3$SO$_3$]

fac-[Mn(CO)$_3$(Phen)(H$_2$O)][CF$_3$SO$_3$] was dissolved in a 0.2 M solution of thiourea in methanol and the solution was stirred overnight at room temperature. The solution was dried and a yellow precipitate formed.

UV/vis: λ_{max} = 375 nm, ε = 712 M^{-1} cm^{-1}.

IR (KBr, cm^{-1}): υ_{CO}= 2030, 1940, 1920.

^{1}H NMR (300 MHz, Acetone-*d$_6$*): δ = 9.63 (dd, 2 H,*J* = 17.6 Hz), 8.93 (dd, 2H, *J* = 25.1 Hz), 8.33 (d, 2H, *J* = 29.8 Hz), 8.19 (dd, 2H, *J* = 57.8 Hz, 28.9 Hz), 6.92 (s, 4H).

^{13}C NMR (151 MHz, Acetone-*d$_6$*): δ = 126.34, 127.61, 130.26, 138.49, 146.20, 154.12, 185.59.

3.3.11. Synthesis of *fac*-[$Mn(CO)_3(Pico)(H_2O)$]

$Mn(CO)_5Br$ (0.2741 g, 0.997 mmol) was dissolved in 20 mL acetone. $AgCF_3SO_3$ (0.3112 g, 1.2 mmol) dissolved in 20 mL acetone was added to the mixture and refluxed at 60°C for 1 hour. The precipitate (AgBr) was filtered off and weighed (0.0467 g, 0.25 mmol). The yellow solution was then dried under vacuum to form a yellow oil. Picolinic acid (0.1230 g, 0.995 mmol) dissolved in 10 mL water was added to the yellow oil and refluxed at 110°C for 24 hours under nitrogen. The bright yellow solution was dried under vacuum to form a yellow precipitate.

UV/vis: λ_{max} = 385 nm, ε = 47.6 M^{-1} cm^{-1}.

IR (KBr,cm^{-1}): 2034, 1934, 1912.

^{1}H NMR (300 MHz, Acetone-d_6): δ = 9.21(d, 1H, *J* = 8.2 Hz), 8.60 (d, 1H, *J* = 8.2 Hz), 8.02 (t, 1H, *J* = 9.6 Hz), 7.50 (t, 1H, *J* = 9.6 Hz).

^{13}C NMR (151 MHz, Acetone-d_6): δ = 119.23, 121.83, 125.64, 128.14, 139.93, 152.70, 208.70, 209.08.

Yield: 0.0986g, 35%.

3.3.12. Synthesis of *fac*-[$Mn(CO)_3(Pico)(MeOH)$]

fac-[$Mn(CO)_3(Pico)(H_2O)$] was dissolved in methanol (10 mL of a 0.5 × 10^{-3} M solution) and the solution stirred overnight at room temperature. The solution was dried and a yellow-orange precipitate was the result.

UV/vis: λ_{max} = 387 nm, ε = 105 M^{-1} cm^{-1}.

IR (KBr,cm^{-1}): 2028, 1931, 1907.

^{1}H NMR (300 MHz, Acetone-d_6): δ = 9.28 (d, 1H, *J* = 8.4 Hz), 8.66 (d, 1H, *J* = 8.4 Hz), 8.11 (t, 1H, *J* = 9.5 Hz), 7.77 (t, 1H, *J* = 9.5 Hz), 3.81 (s, 3H).

^{13}C NMR (151 MHz, Acetone-d_6): δ = 131.20, 125.75, 126.01, 129.88, 141.11, 153.01.

3.3.13. Synthesis of *fac*-[$Mn(CO)_3(Pico)(TU)$]

fac-[$Mn(CO)_3(Pico)(H_2O)$] was dissolved in a 0.2 M solution of thiourea in methanol and the solution was stirred overnight at room temperature. The solution was dried and an orange yellow precipitate formed.

UV/vis: λ_{max} = 385 nm, ε = 51 M^{-1} cm^{-1}.

IR (KBr,cm^{-1}): 2025, 1928, 1901.

^{1}H NMR (300 MHz, Acetone-d_6): δ = 9.08 (d, 1H, *J* = 8.1 Hz), 8.44 (d, 1H, *J* = 8.1 Hz), 8.09 (t, 1H, *J* = 9.2 Hz), 7.91 (t, 1H, *J* = 9.3 Hz), 7.18 (s, 4H).

^{13}C NMR (151 MHz, Acetone-d_6): δ = 130.88, 124.90, 125.81, 130.05, 140.71, 152.87, 185.04.

3.3.14. Synthesis of *fac*-[Mn(CO)$_3$(Pico)(Br)][Na]

fac-[Mn(CO)$_3$(Pico)(H$_2$O)] was dissolved in a 0.2 M solution of NaBr in methanol and the solution was stirred overnight at room temperature. The solution was dried and an orange precipitate formed.

UV/vis: λ_{max} = 415 nm, ε = 48 M^{-1} cm^{-1}.

IR (KBr,cm^{-1}): 2030, 1930, 1909.

^{1}H NMR (600 MHz, DMSO-d_6): δ = 9.11 (d, 1H, *J* = 8.4 Hz), 8.53 (d, 1H, *J* = 8.4 Hz), 8.00 (t, 1H, *J* = 9.5 Hz), 7.82 (t, 1H, *J* = 9.5 Hz).

^{13}C NMR (151 MHz, DMSO-d_6): δ = 130.78, 126.05, 126.09, 128.97, 140.89, 154.21.

3.3.15. Synthesis of *fac*-[Mn(CO)$_3$(Pico)(Py)]

fac-[Mn(CO)$_3$(Pico)(H$_2$O)] was dissolved in a few drops of pyridine and the solution was stirred overnight at room temperature. The solution was dried and an orange yellow precipitate formed.

UV/vis: λ_{max} = 365 nm, ε = 44 M^{-1} cm^{-1}.

IR (KBr,cm^{-1}): 2023, 1929, 1903.

^{1}H NMR (600 MHz, DMSO-d_6): 9.22 (d, 1H, *J* = 8.2 Hz), 8.61 (d, 2H, *J* = 6.3 Hz), 8.48 (d, 1H, *J* = 8.1 Hz), 8.04 (t, 1H, *J* = 9.6 Hz), 7.75 (t, 1H, *J* = 9.6 Hz), 7.59 (dt, 1H, *J* = 6.3 Hz, 3.1 Hz), 7.48 (s, 2H).

^{13}C NMR (151 MHz, DMSO-d_6): δ = 131.20, 125.75, 126.01, 126.54, 129.88, 138.56, 141.11, 145.21, 153.01.

3.3.16. Synthesis of [Mn(CO)$_3$(2,4-Quin)(H$_2$O)]

Mn(CO)$_5$Br (0.2740 g, 0.997 mmol) was dissolved in 20 mL acetone. A solution of $AgCF_3SO_3$ (0.3111 g, 1.2 mmol) dissolved in 20 mL acetone was added to the mixture and refluxed at 60°C for 1 hour. The precipitate (AgBr) was filtered off and the yellow solution was then dried under vacuum to form a yellow oil. Quinoline-2,4-dicarboxylic acid (0.2175 g, 1 mmol) dissolved in 10 mL water was added to the oil and refluxed at 110 °C for 24 hours under nitrogen. An orange-red precipitate was formed as the product and it was dried and weighed.

UV/vis: λ_{max} = 392 nm, ε = 4405 M^{-1} cm^{-1}.

IR (KBr,cm^{-1}): 2034, 1940, 1903.

^{1}H NMR (600 MHz, Acetone-d_6): δ = 9.13 (d, 1H, *J* = 8.7Hz), 8.97 (d, 1H, *J* = 8.6 Hz), 8.25 (t, 1H, *J* = 18 Hz), 8.01 (t, 1H, *J* = 18 Hz), 7.45 (s,1H).

^{13}C NMR (151 MHz, Acetone-d_6): δ = 121.81, 126.84, 128.45, 130.58, 132.15, 139.15, 148.83, 151.62, 175.00.

Yield: 0.1130g, 30%.

3.3.17. Synthesis of *fac*-[Mn(CO)$_3$(2,4-Quin)(MeOH)]

fac-[Mn(CO)$_3$(2,4-Quin)(H$_2$O)] was dissolved in methanol (10 mL of a 0.5 × 10^{-3} M solution) and the solution stirred overnight at room temperature. The solution was dried and a dark orange precipitate was the result.

UV/vis: λ_{max} = 398 nm, ε = 1792 M^{-1} cm^{-1}.

IR (KBr, cm^{-1}): υ_{CO}= 2037, 1907.

^{1}H NMR (600 MHz, Acetone-d_6): δ = 9.20 (d, 1H, *J* = 8.6Hz), 8.87 (d, 1H, *J* = 8.6 Hz), 8.25 (t, 1H, *J* = 18.2 Hz), 8.13 (t, 1H, *J* = 18.2 Hz), 7.52 (s, 1H), 3.81 (s, 3H).

^{13}C NMR (151 MHz, Acetone-d_6): δ = 123.86, 125.85, 130.65, 131.53, 132.89, 140.26, 149.03, 152.55, 178.02.

3.3.18. Synthesis of *fac*-[Mn(CO)$_3$(2,4-Quin)(TU)]

fac-[Mn(CO)$_3$(2,4-Quin)(H$_2$O)] was dissolved in a 0.2 M solution of thiourea in methanol and the solution was stirred overnight at room temperature. The solution was dried and an orange precipitate formed.

UV/vis: λ_{max} = 395 nm, ε = 1252 M^{-1} cm^{-1}.

IR (KBr, cm^{-1}): υ_{CO}= 2027, 1910.

^{1}H NMR (600 MHz, Methanol-d_4): δ = 8.90 (d, 1H, *J* = 8.6Hz), 8.53 (d, 1H, *J* = 8.6Hz), 8.05 (t, 1H, *J* = 18.2 Hz), 7.91 (s, 1H), 7.61 (t, 1H, *J* = 18.2 Hz), 7.15 (s, 4H).

^{13}C NMR (151 MHz, Methanol-d_4): δ = 121.31, 127.08, 127.70, 129.73, 131.56, 149.15, 153.02, 181.86, 183.97.

3.3.19. Synthesis of *fac*-[Mn(CO)$_3$(2,4-Quin)(Py)]

fac-[Mn(CO)$_3$(2,4-Quin)(H$_2$O)] was dissolved in a few drops of pyridine and the solution was stirred overnight at room temperature. The solution was dried and an orange precipitate formed.

UV/vis: λ_{max} = 380 nm, ε = 1480 M^{-1} cm^{-1}.

IR (KBr, cm^{-1}): υ_{CO}= 2024, 1906.

^{1}H NMR (600 MHz, Methanol-d_4): δ = 9.23 (d, 1H, *J* = 8.6Hz), 9.02 (d,1H, *J* = 8.6Hz), 8.96 (t, 1H, *J* = 25.1 Hz), 8.60 (t, 1H, *J* = 9.7 Hz), 8.25 (s, 1H), 8.12 (m, 2H), 8.01(t, 2H, *J* = 9.6 Hz), 7.66 (s, 2H).

^{13}C NMR (151 MHz, Methanol-d_4): δ = 123.90, 126.88, 127.82, 130.55, 131.60, 132.65, 139.55, 145.42, 145.49, 148.83, 153.68, 176.44.

3.3.20. Synthesis of *fac*-[Mn(CO)$_3$(Flav)(H$_2$O)]

$Mn(CO)_5Br$ (0.2851 g, 1.03 mmol) was dissolved in 20 mL acetone. $AgCF_3SO_3$ (0.3112 g,1.2 mmol) dissolved in 20mL acetone was added to the mixture and refluxed at 60°C for 1 hour. The precipitate (AgBr) was filtered off and the yellow solution was then dried under vacuum to form a yellow oil. 3-Hydroxyflavone (0.2382 g,0.999 mmol) dissolved in 10 mL water was added to the oil and refluxed at 110°C for 24 hours under nitrogen. Orange precipitate formed as the product and was dried and weighed.

UV/vis: λ_{max} = 414 nm, ε = 2200 M^{-1} cm^{-1}.

IR (KBr,cm^{-1}): 2038, 2025, 1949, 1921, 1905.

^{13}C NMR (151 MHz, Acetone-d_6): δ = 118.31, 119.52, 123.69, 124.50, 126.68, 128.36, 129.04, 130.05, 132.80, 133.80, 138.80.

Yield: 0.0987g, 34%.

3.4 Discussion

The main objective of the study was to synthesise Mn (I) tricarbonyl aqua complexes. The syntheses of the complexes was straight forward although certain precautions had to be taken to avoid decomposition. The N,O- and O,O'- bidentate complexes had to be synthesised under N_2 gas and in dark conditions. All the Mn complexes were kept in the dark after synthesis because they are light sensitive.

The *fac*-$Mn(CO)_3(C_3H_6O)_3$ complex was synthesised by removing Br^- using $AgCF_3SO_3$ in acetone. This was adapted from the synthesis by Usón *et al*.[4] This triaqua triacetone complex was added to the ligand dissolved in water to form the different complexes. IR and NMR spectroscopy was used as confirmation of the successful synthesis.

In Table 3.1 the different ν_{CO} stretching frequencies of the Mn (I) and Re (I) tricarbonyl complexes with N,N'-, N,O' and O,O' bidentate ligands are reported. IR spectroscopy is not the only tool that can be used for analysis but it is efficient since it provides a good fingerprint. In this study IR spectroscopy is used for the distinctive stretching frequencies of the carbonyl peaks.

Table 3.1 Infrared stretching frequencies of selected tricarbonyl complexes of Mn (I) and Re (I).

Complex	υ_{CO}	Ref
***fac*-[Mn(Bipy)(CO)$_3$(H$_2$O)]$^+$**	2040 1933	**a**
***fac*-[Mn(Phen)(CO)$_3$(H$_2$O)]$^+$**	2041 1940	**a**
***fac*-[Mn(Pico)(CO)$_3$(H$_2$O)]**	2034 1934 1912	**a**
***fac*-[Mn(2,4-Quin)(CO)$_3$(H$_2$O)]**	2034 1940 1903	**a**
***fac*-[Mn(Flav)(CO)$_3$H$_2$O]**	2038 2025 1949 1921 1905	**a**
***fac*-[Mn(Bipy)(CO)$_3$(MeOH)]$^+$**	2038 1941	**a**
***fac*-[Mn(Bipy)(CO)$_3$(Py)]$^+$**	2023 1924	**a**
***fac*-[Mn(Bipy)(CO)$_3$(TU)]$^+$**	2030 1925	**a**
***fac*-[Mn(Bipy)(CO)$_3$(Br)]**	2025 1894	**a**
***fac*-[Mn(Phen)(CO)$_3$(MeOH)]$^+$**	2025 1894	**a**
***fac*-[Mn(Phen)(CO)$_3$(Py)]$^+$**	2017 1907	**a**
***fac*-[Mn(Phen)(CO)$_3$(TU)]$^+$**	2030 1940 1920	**a**
***fac*-[Mn(Phen)(CO)$_3$(Br)]**	2017 1907	**a**
***fac*-[Mn(2,4-Quin)(CO)$_3$(MeOH)]**	2037 1907	**a**
***fac*-[Mn(2,4-Quin)(CO)$_3$(Py)]**	2024 1906	**a**
***fac*-[Mn(2,4-Quin)(CO)$_3$(TU)]**	2027 1910	**a**
***fac*-[Mn(Pico)(CO)$_3$(MeOH)]**	2028 1931 1907	**a**
***fac*-[Mn(Pico)(CO)$_3$(TU)]**	2025 1928 1901	**a**
***fac*-[Mn(Pico)(CO)$_3$(Py)]**	2023 1929 1903	**a**
***fac*-[Mn(Pico)(CO)$_3$(Br)][Na]**	2026 1930 1909	**a**
***fac*-[Re(Bipy)(CO)$_3$H$_2$O]$^+$**	2008 1904 1882	**13**
***fac*-[Re(Phen)(CO)$_3$H$_2$O]$^+$**	2008 1932 1908	**13**
***fac*-[Re(Pico)(CO)$_3$H$_2$O]**	2022 1908 1874	**13**
***fac*-[Re(2,4-Quin)(CO)$_3$H$_2$O]**	2034 1936 1886	**14**
***fac*-[Re(Flav)(CO)$_3$(H$_2$O)]**	2013 1885	**14**

a = This work

It is clear that there is a difference in the stretching frequencies. First of all regarding the manganese complexes: the *fac*-[Mn(Pico)(CO)$_3$H$_2$O] and *fac*-[Mn(2,4-Quin)(CO)$_3$H$_2$O] (N,O-bidentate ligands) have lower stretching frequencies compared to *fac*-[Mn(Bipy)(CO)$_3$H$_2$O]$^+$ and *fac*-[Mn(Phen)(CO)$_3$H$_2$O]$^+$ (N,N'-bidentate ligands) that

have higher stretching frequencies. This might be due to the fact that the N,O-bidentate ligands are more electron donating than the N,N'-bidentate ligands, which leads to more π donation to the CO ligands which in turn lengthens the C-O bond that means a decrease in stretching frequency.

The values of the stretching frequencies for the aqua complexes synthesized are as follows: 2040 cm^{-1} for *fac*-$[Mn(Bipy)(CO)_3H_2O]^+$ ≥ 2041 cm^{-1} *fac*-$[Mn(Phen)(CO)_3H_2O]^+$ > 2038 cm^{-1} *fac*-$[Mn(Flav)(CO)_3H_2O]$ > 2034 cm^{-1} *fac*-$[Mn(Pico)(CO)_3H_2O]$ ≥ 2034 cm^{-1} *fac*-$[Mn(2,4\text{-}Quin)(CO)_3H_2O]$. Basically *fac*-$[Mn(Flav)(CO)_3H_2O]$ doesn't follow the trend since O,O'-bidenate ligand systems are even more electron donating than the N,O-bidentate ligands.

Secondly, a decrease in frequencies from the manganese (I) complexes to the rhenium (I) complexes is observed. This might be due to the electron density on the rhenium core that increases the π-backbonding and then lowers the stretching frequency of the carbonyls. For example *fac*-$[Mn(Bipy)(CO)_3H_2O]^+$ with vCO = 2040 cm^{-1} vs *fac*-$[Re(Bipy)(CO)_3H_2O]^+$ with vCO of 2008 cm^{-1}, *fac*-$[Mn(Phen)(CO)_3H_2O]^+$ with vCO = 2041 cm^{-1} vs *fac*-$[Re(Phen)(CO)_3H_2O]^+$ with vCO = 2008 cm^{-1}, *fac*-$[Mn(Pico)(CO)_3H_2O]$ with vCO = 2034 cm^{-1} vs *fac*-$[Re(Pico)(CO)_3H_2O]$ with vCO = 2022 cm^{-1} and *fac*-$[Mn(Flav)(CO)_3(H_2O)]$ with vCO = 2038 cm^{-1} vs *fac*-$[Re(Flav)(CO)_3(H_2O)]$ with vCO = 2013 cm^{-1}. *fac*-$[Mn(2,4\text{-}Quin)(CO)_3H_2O]$ and *fac*-$[Re(2,4\text{-}Quin)(CO)_{3(}H_2O)]$ have very similar stretching frequencies indicating that there are however some exceptions found and that this study needs to be expanded to more ligand systems and even different donor atom ligands.

Overall, the synthesis of these complexes was straightforward despite the fact that they are light sensitive. The Mn (I) complexes compare well with the Re (I) analogues in terms of stretching frequencies. A crystallographic investigation of *fac*-$[Mn(CO)_3(Bipy)(H_2O)][CF_3SO_3]$ and *fac*-$[Mn(CO)_3(Phen)(H_2O)][CF_3SO_3]$ are discussed in Chapter 4. Unfortunately we were unable to obtain crystals of the substituted compounds (kinetic end products) that were of good enough quality for X-ray diffraction.

4 CRYSTALLOGRAPHIC STUDY OF MANGANESE (I) COMPLEXES

4.1 Introduction

This chapter reports on two new manganese (I) tricarbonyl crystal structures, both containing a bidentate ligand (2,2'-bipyridyl (bipy) or 1,10-phenanthroline (phen)) and an aqua ligand in the remaining third coordination site. A search of the Cambridge Structural Database (CSD)[1] revealed that there are only two other similar structures available (with aqua ligands in one of the three positions)[8,9](Scheme 4.1), thereby highlighting the contribution of this work to the knowledge base of these structures.

The crystallographic data of the two structures is summarized in Table 4.1. A schematic representation of the general synthetic procedure of the complexes is given in Scheme 4.2. The plane formed by the two carbonyl carbons *trans* to the bidentate ligand, the N,C,C,N atoms of the bidentate ligand itself and the metal centre, will be referred to as the equatorial plane throughout the chapter.

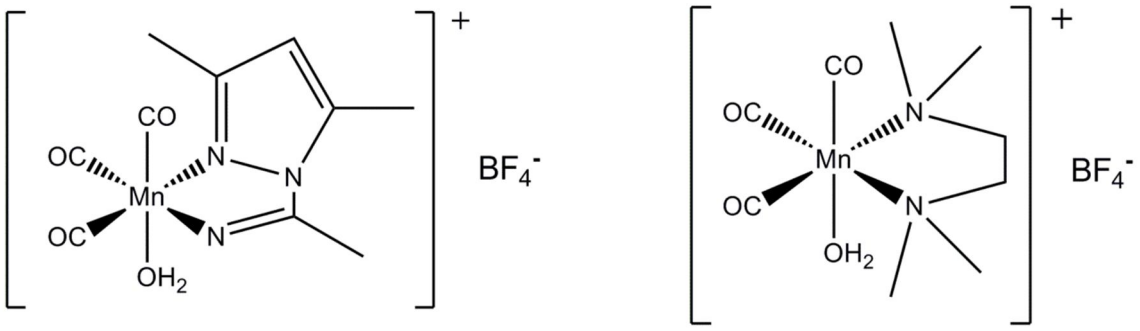

Scheme 4.1: Illustration of the two aqua complexes, *fac*-[Mn(CO_3)(N,N,N',N'-1,1,4,4-(CH_3)$_4$en)(H_2O)] and *fac*-[Mn(CO)$_3$(N=C(CH_3)dmpz-k^2N,N)(H_2O)][a] reported in literature.

a. dmpz = 3,5-dimethylpyrazole.

[1] Cambridge Structural Database (CSD), Version 5.34, Nov 2012 update. F.H. Allen, Acta Cryst., **B58**, 2002, 380. Date Accessed : October 2013.

Scheme 4.2 : An illustration of the general synthetic procedure followed in this study.

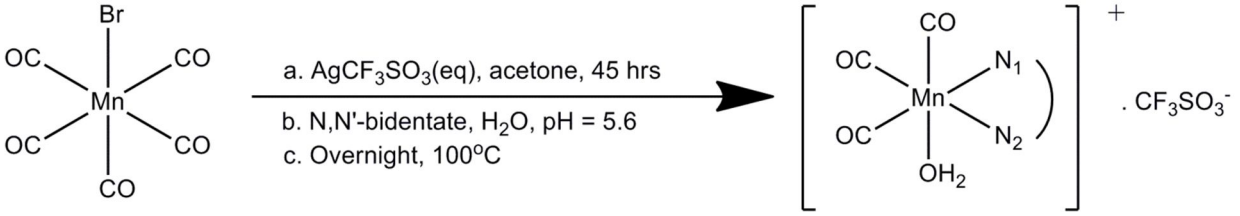

4.2 Experimental

The reflection data for the determination of the structures were collected on a Bruker X8 Apex II 4K diffractometer. The apparatus was equipped with graphite monochromated Mo Kα radiation, with a wavelength of 0.71073 Å and with ω- and φ-scans at 100 K. The cell refinement was performed with SAINT-Plus[2] and the data reduction with SAINT-Plus and XPREP[1]. The absorption corrections were obtained by the use of the multi-scan technique and SADABS[3] software package. The two structures were solved using the SIR-97[4] package and refined with SHELX-97[5] and WinGX[6]. The molecular graphics were done with DIAMOND[7]. All the structures are shown with thermal ellipsoids drawn at 50% probability level, unless otherwise stated. The aromatic hydrogen atoms are geometrically placed in idealized positions (C-H = 0.93 – 0.97 Å) and constrained to ride on their parent atoms (U_{iso} (H) = 1.2U_{eq}(C)). The water molecule's H atoms were placed from the electron density map. All the non-hydrogen atoms were anisotropically refined.

[2] Bruker, *SAINT-Plus*, Version 7.12 (including XPREP), Bruker AXS Inc., Madison, Wisconsin, USA, 2004.
[3] Bruker, *SADABS*, Version 2004/1, Bruker AXS Inc., Madison, Wisconsin, USA, 1998.
[4] Altomare, A., Burla, M.C., Camalli, M., Cascarano, G.L., Giacovazzo, C., Guagliardi, A., Moliterni, A.G.G., Polidori, G., Spagna, R., *J. Appl. Cryst.*, **32**, 1999, 837.
[5] Sheldrick, G.M., *SHELX97*, Program for refinement of crystal structures, University of Göttingen, Germany, 1997.
[6] Farrugia, L.J., *J.Appl. Cryst*., **32**, 1999, 837.
[7] Brandenburg, K., Putz, H., *DIAMOND*, Release 3.0e, Crystal Impact GbR, Bonn, Germany, 2006.

Table 4.1: Summary of the crystallographic data of *fac*-$[Mn(CO)_3(Phen)(H_2O)][CF_3SO_3]$ (1) and *fac*-$[Mn(CO)_3(Bipy)(H_2O)][CF_3SO_3]$ (2).

Crystallographic Data	(1)	(2)
Empirical Formula	$MnC_{16}H_{10}F_3N_2O_7S$	$MnC_{14}H_{10}F_3N_2O_7S$
Formula weight ($g.mol^{-1}$)	486.27	462.25
Crystal System	Monoclinic	Monoclinic
Space Group	$P2_1/c$	$P2_1/c$
a (Å)	10.220(5)	10.662(5)
b (Å)	10.514(5)	9.649(5)
c (Å)	20.068(5)	19.672(5)
α (°)	90	90
β (°)	120.009(15)	119.567(15)
γ (°)	90	90
Volume (A^3)	1867.3(14)	1760.3(13)
Z	4	4
P_{calc} ($g.cm^{-3}$)	1.730	1.744
Crystal colour	Yellow	Yellow
Crystal morphology	Needle	Cuboid
Crystal size (mm)	0.39×0.089×0.069	0.365 × 0.228 × 0.211
μ (mm^{-1})	0.892	0.941
F (000)	976.0	928.0
θ range (°)	2.32 - 27.49	2.31 - 28.00
Index ranges	$-13 \leq h \leq 13$ $-13 \leq k \leq 14$ $-26 \leq l \leq 26$	$-14 \leq h \leq 14$ $-12 \leq k \leq 12$ $-25 \leq l \leq 25$
Reflections collected	32050	23724
Unique reflections	4648	4237
Reflections with I > 2σ(I)	4686	4232
R_{int}	0.0458	0.0478
Completeness to 2 theta (°, %)	28.37, 99.1	28.00, 99.9
Data/ restraints/ parameters	4648 / 3 / 279	4232 / 5 / 289
GooF	1.025	1.066
R [I > 2σ(I)]	$R_1 = 0.0401$ $wR_2 = 0.0947$	$R_1 = 0.0744$ $wR_2 = 0.1669$
R (all data)	$R_1 = 0.0600$ $wR_2 = 0.1037$	$R_1 = 0.0852$ $wR_2 = 0.1767$
ρ_{max}, ρ_{min} ($e\ A^{-3}$)	0.584, -0.578	1.818, -2.387

4.3 Crystal Structure of *fac*-[Mn(CO)$_3$(Phen)(H$_2$O)][CF$_3$SO$_3$] (1)

The yellow needle-like crystals of **(1)** have been obtained as described in Chapter 3. Table 4.1 gives a summary of the general crystal data of **(1)**. This complex crystallizes in the monoclinic space group, $P2_1/c$. The molecular diagram of the complex, showing the numbering scheme is illustrated in Figure 4.1. Some of the bond distances and bond angles are presented in Table 4.2.

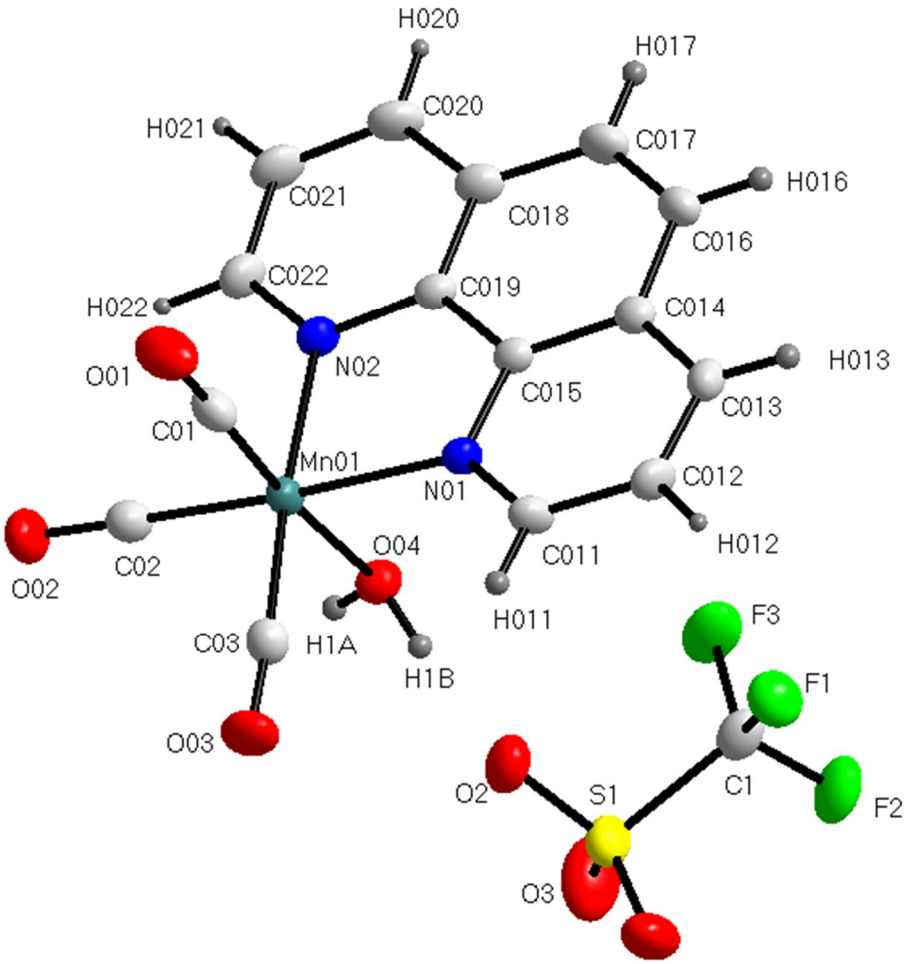

Figure 4.1: Molecular diagram showing the crystal structure and the numbering scheme of *fac*-[Mn(CO)$_3$(Phen)(H$_2$O)][CF$_3$SO$_3$] (1).

A comparison of **(1)** with the Re analogue is discussed in Paragraph 4.5. Some important bond distances and angles of **(1)** are summarized in Table 4.2.

Table 4.2: Selected bond distances and bond angles of (1).

Selected Bonds Distances (Å)			
Mn01 - C01	1.801(2)	Mn01 - N02	2.051(2)
Mn01 - C02	1.811(3)	Mn01 - N01	2.058(19)
Mn01 - C03	1.823(3)	Mn01 - O04	2.073(17)
Selected Bond Angles (°)			
C01 - Mn01 - C02	87.42(11)	C02 - Mn01 - O04	96.52(9)
C01 - Mn01 - C03	91.33(11)	C03 - Mn01 - O04	92.68(9)
C02 - Mn01 - C03	87.52(11)	N02 - Mn01 - O04	83.91(7)
C01 - Mn01 - N02	91.90(10)	N01 - Mn01 - O04	83.31(8)
C02 - Mn01 - N02	95.71(10)	C01 - Mn01 - N01	92.49(10)
C03 - Mn01 - N02	175.53(9)	C02 - Mn01 - N01	176.04(9)
N02 - Mn01 - N01	80.33(8)	C03 - Mn01 - N01	96.44(9)
C01 - Mn01 - O04	174.50(9)		

The Mn atom is octahedrally surrounded by three *facially* arranged carbonyl groups, a bidentate phenanthroline ligand and a water ligand. The Re-C bond distance for the axial carbonyl carbon atom is slightly shorter than the two equatorial carbonyl carbons, with a distance of 1.801(2) Å compared to 1.811(3) Å and 1.823(3) Å respectively. This is similar to *fac*-[$Mn(CO)_3$(N=C(CH_3)dmpz-k^2N,N)(H_2O)][7] reported by Antón *et al*.[8] where the axial Mn-C bond distance of 1.796(6) Å was reported. Horn *et al.*[9] reported *fac*-[$Mn(CO)_3$(N,N,N',N'-1,1,4,4-(CH_3)$_4$en)(H_2O)] the axial Mn-C bond with a distance of 1.779(6) Å. The Mn-O bond distance of 2.073 (17) Å of the complex reported here is slightly shorter than the two structures in literature where distances of 2.108(5) Å and 2.099(3) Å were reported. The octahedral arrangement is slightly distorted as illustrated by the C02-Mn-N01 and C03-Mn-N02 angles of 176.04(9)° and 175.53(9)° respectively, and the N02-Mn01-N01 bite angle of 80.33(8)°. The bite angles of the bidentate ligand to the metal of the complexes prepared by Antón *et al*.[8] and Horn *et al*.[9] are reported as 113.3(3)° and 83.2(2)° respectively and compares well to that reported for **(1)**.

[8] Antón, N., Arroyo, M., Gómez-Iglesias, P., Miguel, D., Villafañe, F., *J. Organomet. Chem*., **693**, 2008, 3074.
[9] Horn, E., Horiuchi, A., *Z. Kristallogr., New Cryst. Struct.*, **216**, 2001, 3074.

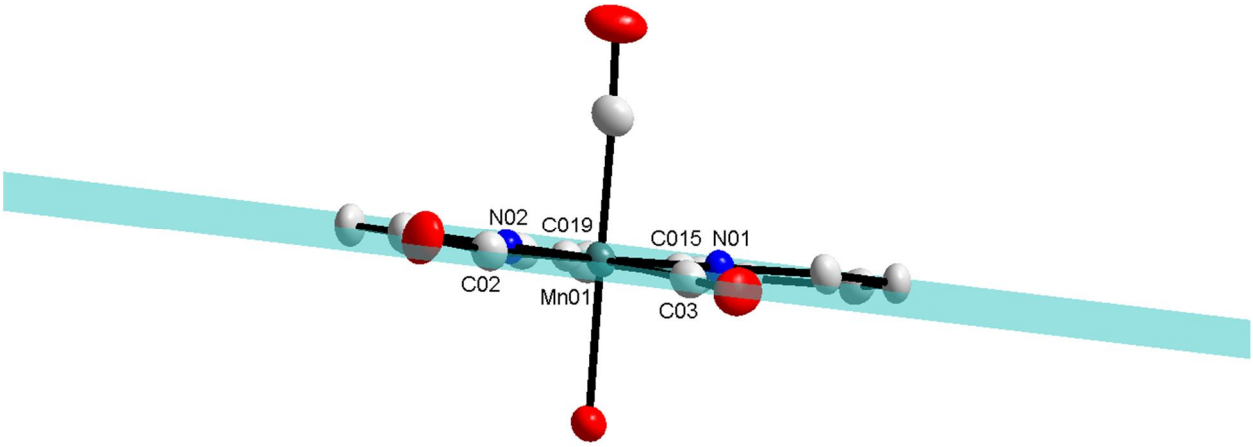

Figure 4.2: Illustration of the plane through Mn01-N01-N02-C03-C02-C015-C019 for the structure of (1).

A plane constructed through the equatorial plane (Mn01-C02-C03-N01-N02-C015-C019) shows the largest deviation of 0.0664(0.0015) Å for N01 from the plane, (rms = 0.0397) as illustrated in Figure 4.2.

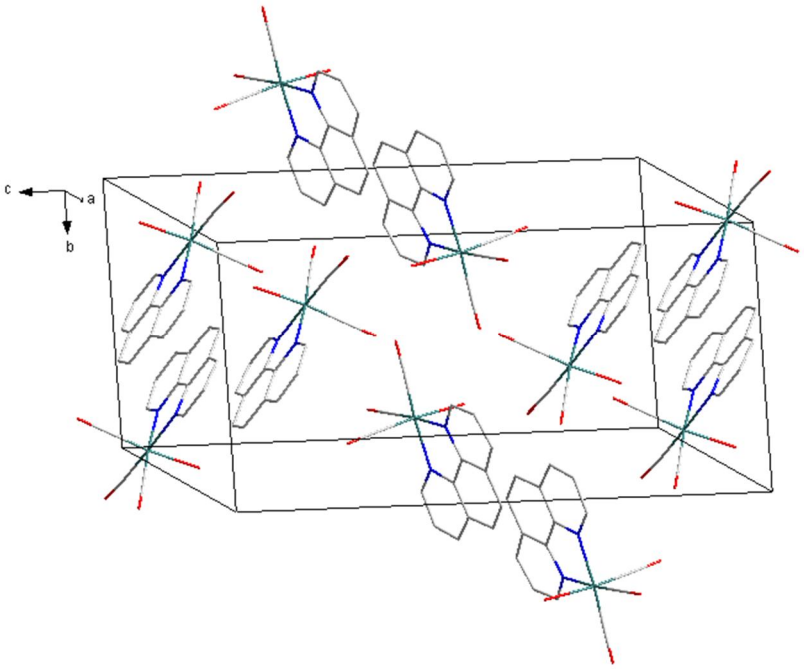

Figure 4.3: Packing of (1) in the unit cell when viewed along the bc plane.

The packing of **(1)** is illustrated in Figure 4.3. The molecules pack in a head-to-head fashion in a column-like structure when viewed along the b,c-plane.

C-H···O, O-H···O and C-H···F hydrogen bonding interactions are observed between the cations and neighbouring anions (Figure 4.4). The bond angles, distances and symmetry operations are summarized in Table 4.3.

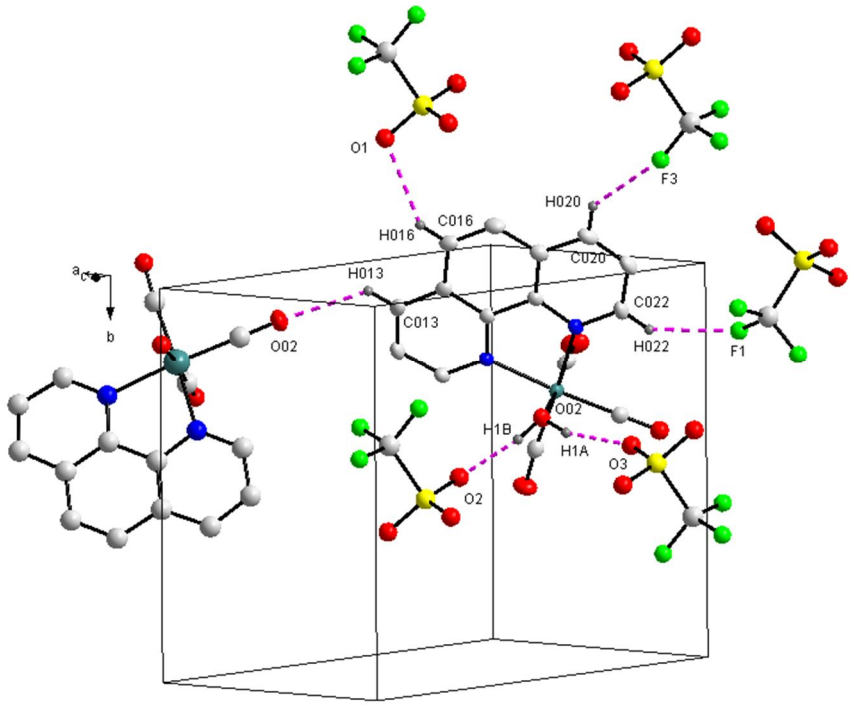

Figure 4.4: Hydrogen interactions observed in (1). Hydrogen atoms not part of the interactions are omitted for clarity.

Table 4.3: Hydrogen bond distances and angles (Å,°) of (1).

D-H···A	D(D-H) (Å)	D(H···A) (Å)	D(D···A) (Å)	D-H···A (°)
O04-H1A...O3[a]	0.859	1.887	2.709(3)	160
O04-H1B...O2	0.861	1.917	2.745(3)	161
C013-H013...O02[b]	0.930	2.560	3.203(3)	126.7
C016-H016...O1[c]	0.930	2.510	3.305(3)	144.1
C022-H022...F1[d]	0.930	2.460	3.205(3)	136.9
C020-H020...F3[e]	0.930	2.390	3.143(3)	137.8

Symmetry operations, transformations used to generate equivalent atoms:
[a] - x, 1 - y, 1 - z; [b] 1 + x, 0.5 – y, 0.5 + z; [c] x, -1 + y, z; [d] -1 + x, 0.5 – y, -0.5 + z; [e] –x, -y, 1 - z

Some π – π stacking interactions are observed in the crystal structure of **(1)**. Figure 4.5 illustrates the π – π interactions observed between the 1,10-phenanthroline ligands of neighbouring molecules with a centroid to centroid distance of 3.819(1) Å.

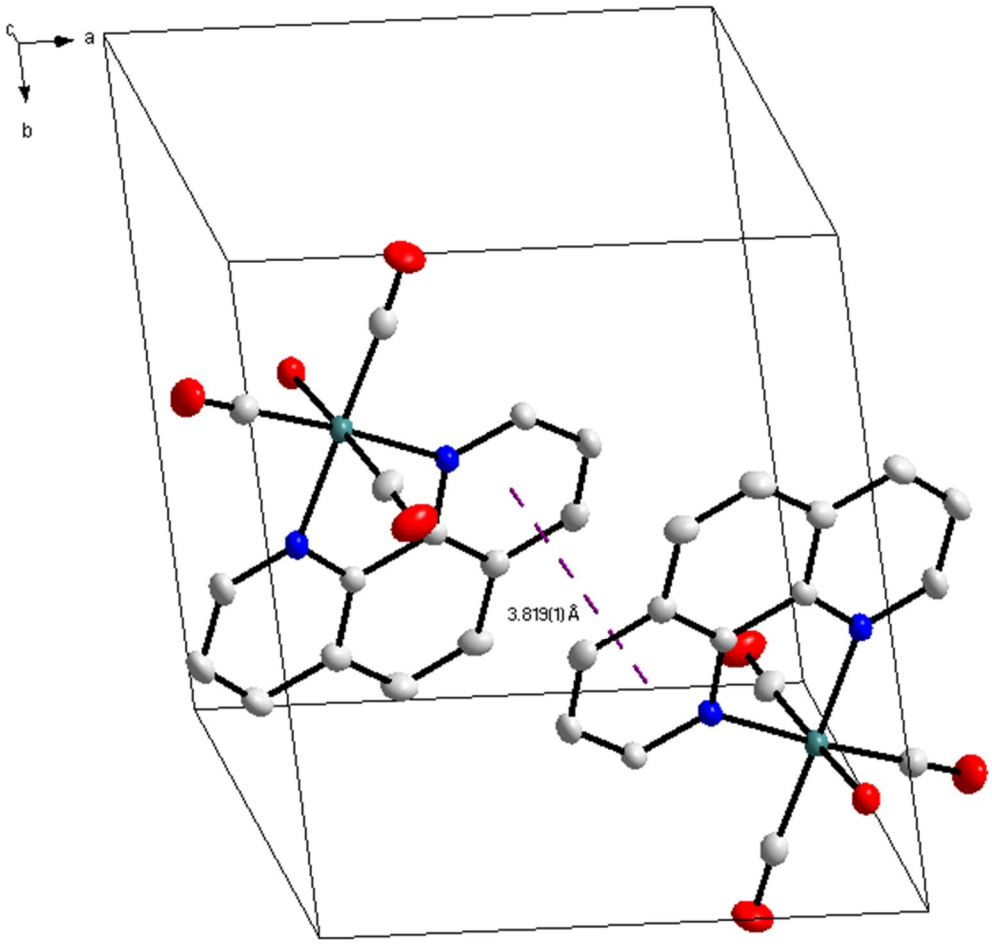

Figure 4.5: π-π Interactions observed between the phenanthroline ligands in (1). Hydrogen atoms are omitted for clarity. (Symmetry operations, transformations used to generate equivalent atoms: x, 0.5-y, -0.5+z; 1-x, 0.5+y, 0.5-z).

4.4 Crystal Structure of *fac*-[Mn(CO)$_3$(Bipy)(H$_2$O)][CF$_3$SO$_3$] (2)

The synthesis of *fac*-[Mn(CO)$_3$(Bipy)(H$_2$O)][CF$_3$SO$_3$] was described in Chapter 3. A summary of the crystal data for the yellow cuboidal crystals is given in Table 4.1. This compound crystallized in the $P2_1/c$ space group. It is a six coordinated complex with an octahedral orientation, with three *facial* carbonyl ligands, a water ligand and a bidentate bipyridyl ligand. A molecular diagram with the numbering scheme is given in Figure 4.6. Selected bond distances and bond angles of **(2)** are given in Table 4.4.

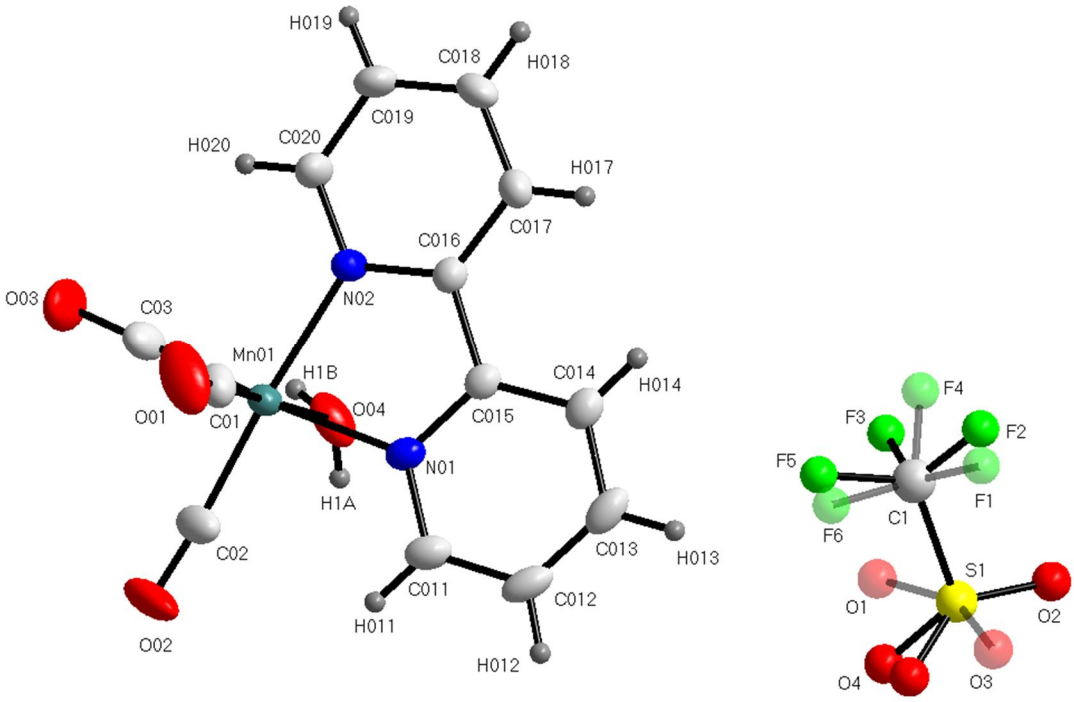

Figure 4.6: Molecular diagram of *fac*-[Mn(CO)$_3$(Bipy)(H$_2$O)][CF$_3$SO$_3$] (2) showing the numbering scheme.

Table 4.4: Selected bond distances and bond angles of (2).

Selected Bonds Distances (Å)			
Mn01 - C01	1.792(5)	Mn01 - N02	2.042(4)
Mn01 - C02	1.813(5)	Mn01 - N01	2.040(4)
Mn01 - C03	1.805(5)	Mn01 - O04	2.068(4)
Selected Bond Angles (°)			
C01 - Mn01 - C02	90.40(2)	C02 - Mn01 - O04	91.06(19)
C01 - Mn01 - C03	86.90(2)	C03 - Mn01 - O04	98.30(2)
C02 - Mn01 - C03	86.80(2)	N02 - Mn01 - O04	83.54(15)
C01 - Mn01 - N02	94.80(2)	N01 - Mn01 - O04	82.81(15)
C02 - Mn01 - N02	174.32(18)	C02 - Mn01 - N01	98.30(2)
C03 - Mn01 - N02	95.67(19)	C03 - Mn01 - N01	174.77(19)
C01 - Mn01 - N01	91.85(19)	N02 - Mn01 - N01	79.36(15)
C01 - Mn01 - O04	174.60(2)		

In the triflate anion, the three fluoride atoms are substitutionally disordered over two positions in a 0.476:0.524 ratio. Also, two of the three oxygen atoms illustrate substitutional disorder over two positions in the same ratio, 0.476:0.524. This is illustrated in Figure 4.6.

The axial Re-carbonyl carbon bond distance of 1.792(5) Å is comparable to the aqua complex, *fac*-[Mn(CO)$_3$(N=C(CH$_3$)dmpz-k^2N,N)(H$_2$O)][7], of Antón *et al.*[7] and *fac*-[Mn(CO)$_3$(N,N,N',N'-1,1,4,4-(CH$_3$)$_4$en)(H$_2$O)] of Horn *et al*.[9] with the Mn-CO distance reported as 1.796(6) Å and 1.779(6) Å respectively. The octahedral arrangement is once again slightly distorted, since the C02-Mn01-N02, C03-Mn01-N01 and C01-Mn01 O04 angles deviate from 180° with values of 174.32(18)°, 174.77(19)° and 174.60(2)° respectively and the bite angle that deviates substantially from 90°, with an angle reported as 79.36(15)°. All the other bond distances and angles of **(2)** are similar to those reported by Antón *et al*. and Horn *et al*.

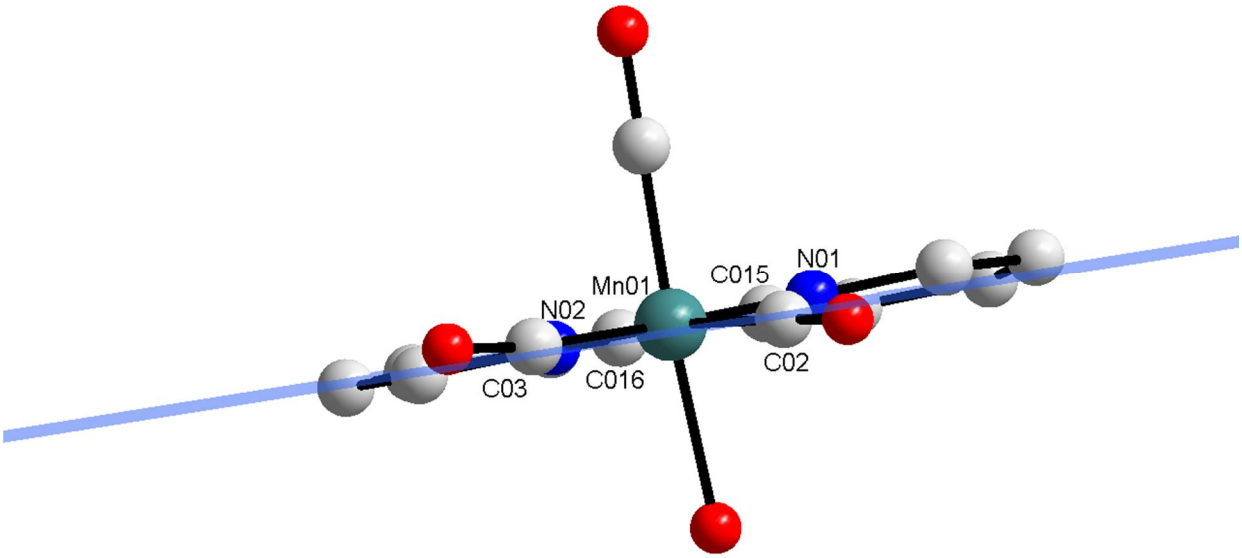

Figure 4.7: Diagram illustrating the plane through Mn01-C02-C03-N01-N02-C015-C016 for the crystal structure of (2).

Figure 4.7 illustrates the equatorial plane (Mn01-C02-C03-N01-C015-C016-N02) with the largest deviation from the plane reported as 0.0825(0.0030) Å for N01 (rms = 0.0502).

The packing of **(2)** follows a head-to-head pattern in a column-like structure when viewed along the b,c-plane (Figure 4.8).

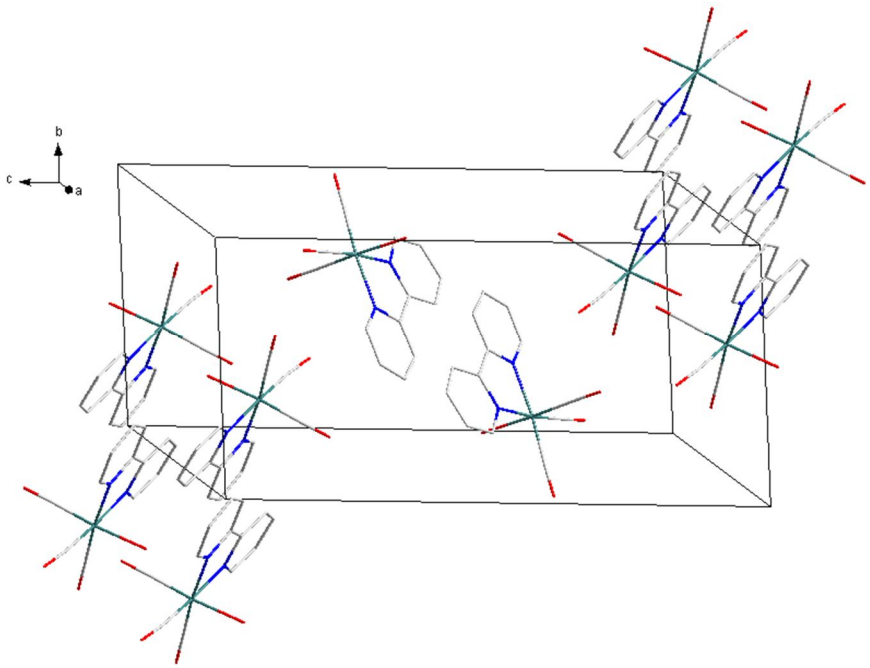

Figure 4.8: Illustration of the head-to-head packing of (2).

The O-H…O and C-H….H hydrogen interactions in **(2)** are illustrated in Figure 4.9. The hydrogen bond distances and bond angles as well as their symmetry are reported in Table 4.5.

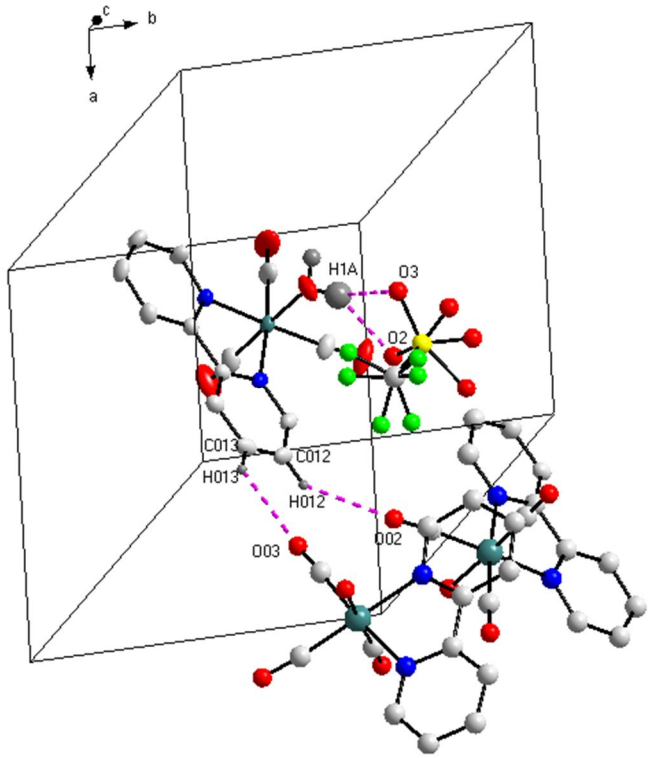

Figure 4.9: Diagram illustrating the hydrogen interactions in *fac*-[Mn(CO)$_3$(Bipy)(H$_2$O)][CF$_3$SO$_3$](2).

Table 4.5: Hydrogen bond distances and bond angles (Å,°) of (2).

D-H···A	D(D-H) (Å)	D(H···A) (Å)	D(D···A) (Å)	D-H···A (°)
O04-H1A...O3[a]	0.840	2.170	2.895(7)	144
O04-H1B...O2[a]	0.840	2.310	3.035(16)	144
C013-H013...O03[b]	0.930	2.560	3.222(6)	128.4
C012-H012...O02[c]	0.930	2.550	3.362(6)	146.0

Symmetry operations, transformations used to generate equivalent atoms:
[a] 2 - x, 0.5 + y, 2.5 - z; [b] 1 + x, 0.5 – y, 0.5 + z; [c] 2 - x, 1 - y, 2 - z

Two π-π interactions are observed between the 2,2'-bipyridyl ligands of neighbouring molecules in **(2)**. The centroid to centroid distances are reported as 3.694(1) Å and 3.914(1) Å (Figure 4.10).

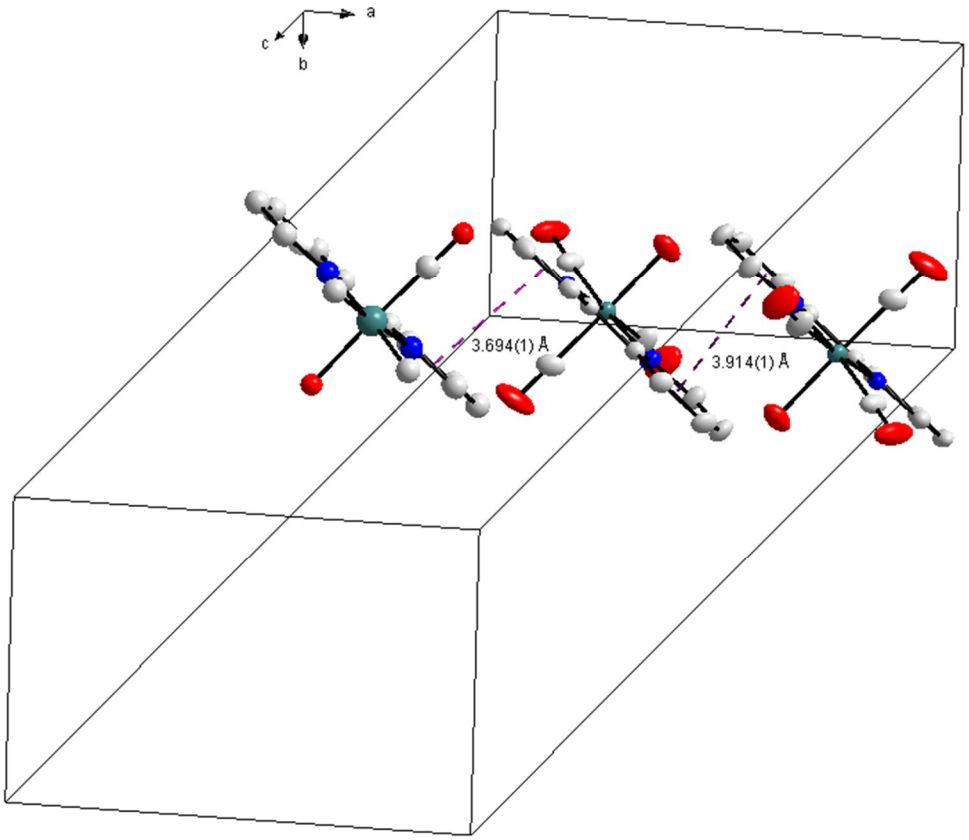

Figure 4.10: π-π Interactions observed between the ligand phenyl rings of (2). (Symmetry operations, transformations used to generate equivalent atoms: -1+x,1+y,-1+z; 1-x,1-y,1-z; x,1+y,-1+z).

4.5 Discussion

Not many Mn (I) aqua tricarbonyl crystal structures have been reported. The only two in literature and mentioned in this chapter are the pyrazolylamidino aqua complex reported by Antón *et al.*[8] and the tetramethylethylenediamine aqua complex reported by Horn *et al*.[9] Other structures with different axial ligands, other than water have been reported. Ara *et al.*[10] reported pyridine-2-thiolato complexes with the bipyridyl ligand as bidentate ligand. The structure of tricarbonyl manganese with tert-butyl isocyanide as the axial ligand was reported by Valin *et al.*[11]

Selected bond lengths and angles for **(1)** and **(2)** are summarized in Table 4.7. In Figure 4.11 a schematical representation of these reported structures are given.

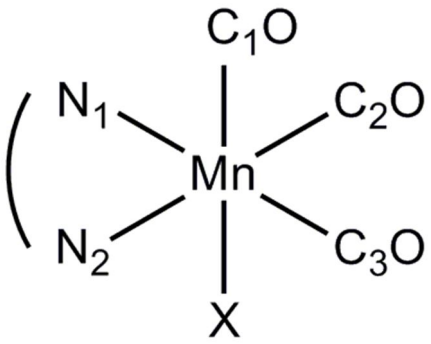

Figure 4.11: Figure showing the labelling system for the bond lengths the complexes in Table 4.6.

From Table 4.6 overall, it can be seen that the bond distances of **(1)** and **(2)** are consistent with similar complexes. The Mn-O bond distances of **(1)** and **(2)** compare well with similar structures in literature like the pyrazolylamidino aqua complex of Antón *et al.*[7] of 2.108(5) Å, the tetramethylethylenediamine aqua complex of Horn *et al*.[9] with a distance of 2.099(3) Å and the triflate structure of Pereira *et al.*[14] with a Mn-O bond distance of 2.096(4) Å. The bidentate ligand bite angles of **(1)** and **(2)** are 80.33(8)° and 79.36(15)° respectively and are more or less the same as expected due to the rigidity of these ligands. The Mn-N_1 and Mn-N_2 bond distances of 2.042(4) Å and 2.040(4) Å for the bipy ligand is comparable to the bond distances reported by Horn *et al*.[11] and that reported by Ara *et al*.[10] with distances of 2.062(3) Å and 2.051(3) Å respectively for Mn-N_1 and 2.044(3) Å and 2.052(3) Å for Mn-N_2. The Mn-N bond distances for **(2)** with the phen ligand also compare well to the structures reported by Pereira *et al*.[13] and Valin *et*

[10] Ara, G., Kabir, S.E., Kundu, K., Malik, K.M.A., *J Chem Cryst*., **33**, 2003, 851.
[11] Valín, M.L., Moreiras, D., Solans, X., Font-Altaba, M., García-Alonso, F.J., *Acta Cryst*. **C42**, 1986, 417.

al.[11] The Mn-N_1 bond distance of 2.058(2) Å compares with the bond distances reported by Pereira *et al*.[13] and Valin *et al*.[11] of 2.062(4) Å and 2.067(4) Å respectively and the Mn-N_2 bond distance of 2.051(19) Å also compared well with the bond distances of 2.053(4) Å and 2.030(4) Å of Pereira *et al*.[13] and Valin *et al*.[11] respectively.

Table 4.6: A comparison of various manganese tricarbonyl complexes.

	M-N_1 (Å)	M-N_2 (Å)	M-X (Å)	N_1-M-N_2 (°)
***fac*-[Mn(Bipy)]**[a, ‡]	2.042(4)	2.040(4)	2.068(4)	79.36(15)
***fac*-[Mn(Phen)]**[b, ‡]	2.058(2)	2.051(19)	2.073(17)	80.33(8)
***fac*-[Mn(N=C(CH_3)dmpz-k^2N,N)]**[c, 8]	2.048(4)	2.015(4)	2.108(5)	113.3(3)
***fac*-[Mn(N,N')(H_2O)]**[d, 9]	2.210(1)	2.070(1)	2.099(3)	83.20(2)
***fac*-[Mn(Bipy) (η^1-pyS)]**[*, e, 10]	2.051(3)	2.052(3)	2.372(13)	78.50(15)
***fac*-[Mn(Bipy)Cl]**[f, 12]	2.062(3)	2.044(3)	2.399(1)	78.50(1)
***fac*-[Mn(Phen)(tert-butyl iso)]**[**, g, 11]	2.067(4)	2.060(4)	1.969(6)	79.20(2)
***fac*-[Mn(Phen)(CF_3SO_3)]**[h, 13]	2.062(4)	2.053(4)	2.096(4)	79.90(2)

*** η^1-pyS = Pyridine-2-thiolato, ** tert-butyl iso = Tert-butyl isocyanide, ‡ = This work, a = *fac*-[Mn($CO)_3$(Bipy)(H_2O)], b = *fac*-[Mn($CO)_3$(Phen)(H_2O)], c = *fac*-[Mn($CO)_3$(N=C(CH_3)dmpz-k^2N,N)(H_2O)], d = *fac*-[Mn($CO)_3$(N,N,N',N'-1,1,4,4-($CH_3)_4$en)(H_2O)], e = *fac*-[Mn($CO)_3$(Bipy) (η^1-pyS)], f = *fac*-[Mn($CO)_3$(Bipy)Cl], g = *fac*-[Mn($CO)_3$(Phen)(tert-butyl iso)], h = *fac*-[Mn($CO)_3$(Phen)(CF_3SO_3)].**

From Table 4.7, it can be concluded that the manganese (I) complexes have shorter bond distances around the metal core than the corresponding rhenium complexes. This is expected since rhenium has a larger atomic mass and a larger van der Waals radius. The Mn-O distances of **(1)** and **(2)**, 2.068(4) Å and 2.073(17) Å respectively, are also significantly shorter than the Re-O distances of the *fac*-[Re($CO)_3$(Phen)(H_2O)] and *fac*-[Re($CO)_3$(Bipy)(H_2O)] structures reported by Kemp[12] with Re-O distances of 2.159(5) Å and 2.160(3) Å respectively. Schutte *et al*.[13] reported O,O'-bidentate structures of which the Re-O distance was reported as 2.188(3) Å for the *fac*-[Re($CO)_3$(Flav)(H_2O)] (Flav = Flavonol). Schutte *et al*.[14] reported on another O,O'-bidentate structure, *fac*-[Re($CO)_3$(Trop)(H_2O)], with a Re-O distance of 2.213(5) Å (Trop = Tropolone). With regards to the bite angles, the manganese complexes have larger angles than the corresponding rhenium analogues. As indicated in Table 4.6, N_1-Mn-N_2 angles are reported as 79.36(15)° and 80.33(8)° for **(1)** and **(2)** respectively. The rhenium bite angles are shorter as illustrated in Table 4.7.

[12] Kemp, G. PhD Dissertation, University of Johannesburg, 2006.
[13] Schutte, M., Kemp, G., Visser, H.G., Roodt, A. *Inorg Chem*. **50(24)**, 2011, 12486.
[14] Schutte, M., Visser, H.G., Roodt, A. *Acta Crystallogr*. **E64**, 2008, m1610.

Table 4.7: Comparison of Mn-H_2O complexes and Re-H_2O.

Complex	M-C_1 (Å)	M-C_2 (Å)	M-C_3 (Å)	M-O (Å)	X_1-M-X_2 (°)
***fac*-[Mn(CO)$_3$(Phen)]$^{+}$ ‡,a**	1.801(2)	1.823(3)	1.811(3)	2.073(17)	80.33(8)
***fac*-[Mn(CO)$_3$(Bipy)]$^{+}$ ‡,b**	1.792(5)	1.813(5)	1.805(5)	2.068(4)	79.36(15)
***fac*-[Re(CO)$_3$(Bipy)]$^{+14,c}$**	1.885(8)	1.923(7)	1.918(7)	2.159(5)	74.92(18)
***fac*-[Re(CO)$_3$(Phen)]$^{+14,d}$**	1.891(5)	1.910(5)	1.933(5)	2.160(3)	75.95(13)
***fac*-[Re(CO)$_3$(Trop)]^{16,e}**	1.890(7)	1.886(8)	1.894(8)	2.213(5)	74.82(18)
***fac*-[Re(CO)$_3$(Flav)]^{15,f}**	1.895(4)	1.897(4)	1.903(4)	2.188(3)	76.24(11)

‡ = This work, a = *fac*-[Mn(CO)$_3$(Phen)(H$_2$O)]$^{+}$, b = *fac*-[Mn(CO)$_3$(Bipy)(H$_2$O)]$^{+}$, c = *fac*-[Re(CO)$_3$(Bipy)(H$_2$O)]$^{+}$, d = *fac*-[Mn(CO)$_3$(Phen)(H$_2$O)]$^{+}$, e = *fac*-[Re(CO)$_3$(Trop)(H$_2$O)]$^{+}$, f = *fac*-[Mn(CO)$_3$(Flav)(H$_2$O)]$^{+}$.

By looking at Table 4.8 one can see that *fac*-[Mn(Bipy)(CO)$_3$(H$_2$O)]$^{+}$ and *fac*-[Mn(Phen)(CO)$_3$(H$_2$O)]$^{+}$ have stretching frequencies which are more or less the same but in the case of the rhenium(I) complexes, the *fac*-[Re(Phen)(CO)$_3$(H$_2$O)]$^{+}$ is observed to have higher stretching frequencies than [Re(Bipy)(CO)$_3$(H$_2$O)]$^{+}$. The stretching frequencies of the manganese (I) complexes are much higher than that of the rhenium(I) frequencies. Due to their metal cores the *fac*-[Mn(Bipy)(CO)$_3$(H$_2$O)]$^{+}$ has a high stretching frequency than *fac*-[Re(Bipy)(CO)$_3$(H$_2$O)]$^{+}$. Table 4.7 lists the sretching frequencies of the complexes in which the trans *fac*-[Mn(Bipy)(CO)$_3$(H$_2$O)]$^{+}$ stretching frequencies are lower than the *fac*-[Mn(Phen)(CO)$_3$(H$_2$O)]$^{+}$ stretching frequencies. This correlates with the bond distances of the trans carbonyls from the metal centre and how the trans influence affects them. This is in agreement with the Re(I) complexes as well. The trans stretching frequency of the *fac*-[Re(Bipy)(CO)$_3$(H$_2$O)]$^{+}$ complex is lower that of the *fac*-[Mn(Bipy)(CO)$_3$(H$_2$O)]$^{+}$ but their bond distances show that the *fac*-[Re(Bipy)(CO)$_3$(H$_2$O)]$^{+}$ has longer distance than the *fac*-[Mn(Bipy)(CO)$_3$(H$_2$O)]$^{+}$. The *fac*-[Re(Phen)(CO)$_3$(H$_2$O)]$^{+}$ and *fac*-[Mn(Phen)(CO)$_3$(H$_2$O)]$^{+}$ show the same trend with the *fac*-[Re(Phen)(CO)$_3$(H$_2$O)]$^{+}$ bond distance is longer than the *fac*-[Mn(Phen)(CO)$_3$(H$_2$O)]$^{+}$ even though their stretching frequency of the *fac*-[Re(Phen)(CO)$_3$(H$_2$O)]$^{+}$ is lower than the *fac*-[Mn(Phen)(CO)$_3$(H$_2$O)]$^{+}$ complex.

Table 4.8: Comparison of stretching frequencies for Mn-H_2O and Re-H_2O complexes.

Complex	υ_{CO}		
***fac*- [Mn(Bipy)(CO)$_3$(H$_2$O)]$^{+}$**	2040	1933	
***fac*- [Mn(Phen)(CO)$_3$(H$_2$O)]$^{+}$**	2041	1940	
***fac*- [Re(Bipy)(CO)$_3$(H$_2$O)]$^{+}$**	2008	1904	1882
***fac*- [Re(Phen)(CO)$_3$(H$_2$O)]$^{+}$**	2008	1932	1908

Chapter 4

X-ray crystallography is an important tool for the inorganic chemist, not only as a way to identify complexes in crystalline state, but also in chemical kinetics where it is important to identify starting materials, intermediates and final products in order to propose the intimate mechanism through which these reactions proceed. This work reported here then builds on the synthetic work discussed in Chapter 3 and with that continue into the kinetics reported in Chapter 5.

5 METHANOL SUBSTITUTION KINETICS OF MN (I) COMPLEXES

5.1 Introduction

The ligand substitution kinetics of different *fac*-$[M(CO)_3(H_2O)_3]^+$ (M = Mn, Tc, Re) type complexes have been investigated for some time.[1,2] Grundler *et al*. investigated the water exchange rate of *fac*-$[M(CO)_3(H_2O)_3]^+$ by ^{17}O NMR. During the study, they found that the rate of the reactions increase from rhenium to manganese and that the reactivity of the metal centres can be presented as follows: Re < Tc < Mn. This reaction follows a dissociative interchange mechanism with $\Delta S_{ex}^{\dagger}$ = +24.4 ± 8 $J.mol^{-1}.K^{-1}$.

Grundler *et al*. also studied the water substitution kinetics of *fac*-$[Mn(CO)_3(H_2O)_3]^+$ by ^1H NMR using acetonitrile (CH_3CN) and dimethyl sulphide (DMS) as the entering ligands. They found that the water exchange and complex formation with soft and hard donors on the tricarbonyl triaqua complexes had a small dependence on the nature of the entering ligand but were strongly dependent on the metal centre. They also suggested a dissociative interchange mechanism in spite of the high negative entropy value of $\Delta S_{ex}^{\dagger}$ = -33.8 ± 1 $J.mol^{-1}.K^{-1}$ in CH_3CN and -23.3 ± 2 $J.mol^{-1}.K^{-1}$ in DMS. It was again proved that the manganese centre is more reactive than the technetium centre which in turn is faster than the rhenium centre.

In 2008, Helm also investigated the complex formation reactions on these *fac*-$[M(CO)_3(H_2O)_3]^+$ complexes using ^{17}O NMR and adding thiourea, pyrazine and tetrahydrothiophene as ligands.[2] The results obtained from his work again showed that the reactivity of these complexes decrease as you move down the group, Mn > Tc > Re. Prinz *et al*.[3] investigated the water exchange of *fac*-$[Mn(CO)_3(H_2O)_3]^+$ using NMR and compared this to the analogous rhenium complex. In this study it was reported that the manganese complexes are four orders faster than the rhenium complexes, with the water exchange rate for Mn being 19 ± 4 s^{-1} and for Re being 6.3 × 10^{-3} s^{-1}. The

---

[1] Grundler, P.V., Helm, L., Alberto, R., Merbach, A.E., *Inorg. Chem*., **45**, 2006, 10378.
[2] Helm, L., *Coord. Chem. Rev*., **252**, 2008, 2346.
[3] Prinz, U., Koelle, U., Ulrich, S., Merbach, A.E., Maas, O., Hegetschweiler, K., *Inorg. Chem*., **43**, 2004, 2387.

formation of $[\{Mn(CO)_3\}(OH)]_4$ followed an associative interchange process with $\Delta V^{\dagger}$ = -4.5 ± 0.4 $cm^3.mol^{-1}$.

A few kinetic studies have been perfomed on the Re(I) tricarbonyl core. Kemp[4] investigated *fac*-$[Re(N,N'\text{-bid})(H_2O)]^+$ and *fac*-$[Re(N,O\text{-bid})(H_2O)]$ (N,N'-bid = N,N'-bidentate ligand, N,O-bid = N,O-bidentate ligand) type of complexes using various monodentate ligands for the substitution kinetics of the aqua ligand in the axial position. Schutte *et al*.[5] expanded on this study by introducing Re (I) complexes using O,O'-bidentate ligands and other N,O-bidentate ligands. In their study it was proven that the rhenium tricarbonyl complexes with O,O'-bidentate ligands react faster than the complexes with N,O-bidentate ligand systems. All in all, the following reactivity trend was observed: *fac*-$[Re(CO)_3(N,N'\text{-bid})(X)]^n$ < *fac*-$[Re(CO)_3(N,O\text{-bid})(X)]^n$ < *fac*-$[Re(CO)_3(O,O'\text{-bid})(X)]^n$ (with n = +1, 0 and X = H_2O and MeOH). No conclusive evidence was found for the mechanism of these complexes. It was however suggested that these reactions occur *via* an interchange mechanism, ranging from I_a for the cationic N,N'-bid complexes to I_d for the N,O-bid and O,O'-bid complexes.

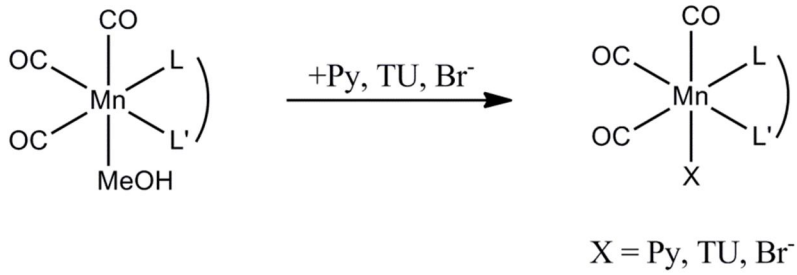

Figure 5.1: Schematic representation of the substitution reactions of *fac*-$[Mn(CO)_3(L,L'\text{-bid})(MeOH)]$ using various entering ligands.

In this study the methanol substitution kinetics of *fac*-$[Mn(CO)_3(L,L'\text{-bid})(MeOH)]^n$ type complexes, with L,L'-bid = N,N'- and N,O'-bidentate ligands, with various monodentate entering ligands are reported. Figure 5.1 shows the schematic representation of the substitution reactions while the complexes studied are illustrated in Figure 5.2.

[4] Kemp, G., PhD Thesis, University of Johannesburg, South Africa, 2006.
[5] Schutte, M., Kemp, G., Visser, H.G., Roodt, A., *Inorg. Chem*., **50**, 2011, 12486.

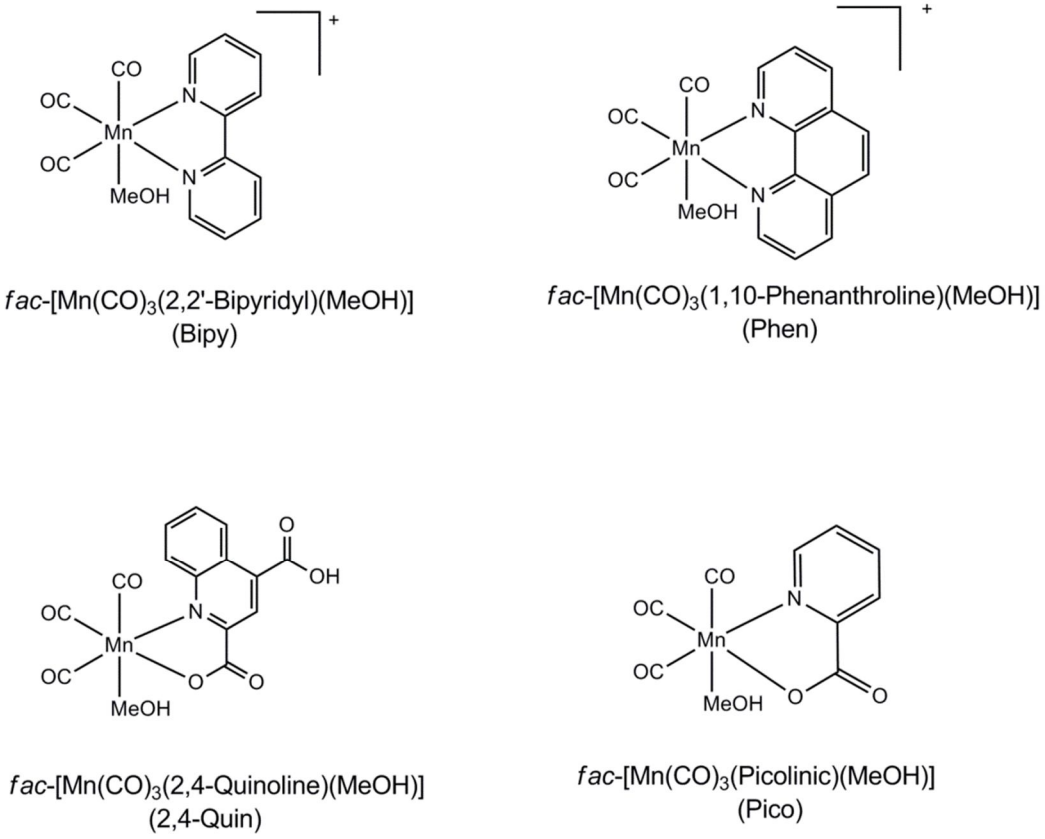

Figure 5.2: Illustration of the complexes used in the study.

5.2 Experimental

5.2.1 General Procedure

The reagents used in the procedures were all of analytical grade. A Varian Cary 50 Conc UV-visible spectrophotometer was used in order to perform the kinetic measurements and *pseudo* first-order conditions were used for all the kinetic measurements. The substitution reactions of *fac*-[$Mn(CO)_3$(Quin)(MeOH)] was performed on a stopped-flow machine. The ligands were in excess in all the reactions. Stability tests on a UV/vis spectrophotometer of all complexes and ligands confirmed that it was stable in methanol. The temperature was maintained using a circulating water bath and the temperature kept within ± 0.1°C. The programs Scientist Micromath, Version 2.01 and Microsoft Office Excel 2003 were used to fit the data. The solid lines on the data represent the least square fit of the data while the individual data points represent the actual experimental values.

5.2.2 Treatment of Data

The Beer-Lambert law is expressed by:

$$A = \varepsilon cl \qquad \text{Eq. 2}$$

After some integration and incorporation, the Beer-Lambert law yields an equation used for the evaluation of the absorbance change *versus* time in simple first-order reactions. The equation used is:

$$A_t = A_\infty - (A_\infty - A_0)e^{k_{obs}t} \qquad \text{Eq. 3}$$

The least-square fit of absorbance *vs*. time for the first order-order reaction is used to determine the *pseudo* first-order rate constant, k_{obs}. The equation was used to fit all the kinetic reactions performed in the study. All the rate constants were calculated and documented in Appendix C. The activation parameters, standard enthalpy change of activation ($\Delta H^{\dagger}$) and standard entropy change of activation ($\Delta S^{\dagger}$) were determined using the logarithmic form of the Eyring equation (Equation 3).

$$\ln\left(\frac{k}{T}\right) = \ln\left(\frac{k_B}{h}\right) - \frac{\Delta H^*}{RT} + \frac{\Delta S^*}{R} \qquad \text{Eq. 4}$$

Where plotting $\ln\left(\frac{k}{T}\right)$ vs. $\frac{1}{T}$ gives a straight line with a slope of $(-\frac{\Delta H^*}{T})$ and an intercept of $(\ln\left(\frac{k_B}{h}\right) + \frac{\Delta S^*}{R})$, where K_B is the Boltzmann constant and h is Planck's constant.

5.3 Results and Discussion

The methanol substitution reactions of *fac*-$[Mn(CO)_3(Phen)(MeOH)]^+$, *fac*-$[Mn(CO)_3(Bipy)(MeOH)]^+$, *fac*-$[Mn(CO)_3(Pico)(MeOH)]$ and *fac*-$[Mn(CO)_3(2,4\text{-}Quin)(MeOH)]$ (with Phen = 1,10-phenanthroline, Bipy = 2,2'-bipyridine, Pico = picolinic acid Quin = 2,4-quinolinic acid) by monodentate ligands (pyridine (Py), thiourea (TU) and bromide ions (Br^-)) are performed in this study. A temperature study for *fac*-$[Mn(CO)_3(Phen)(MeOH)]^+$ and *fac*-$[Mn(CO)_3(Pico)(MeOH)]$ with Py, TU and Br^- were performed while the reactions of *fac*-$[Mn(CO)_3(Bipy)(MeOH)]^+$ and *fac*-$[Mn(CO)_3(2,4\text{-}Quin)(MeOH)]$ were only monitored at 25.0 °C for comparative reasons. The manganese complexes were synthesized and the kinetic study performed to compare

the rates observed with Re (I) analogous complexes. The kinetic studies were performed in methanol as solvent since the complexes used are not soluble in water. It is assumed that the aqua complexes form the corresponding methanol substituted complexes as soon as it is dissolved in methanol for the kinetic study.[5] This was confirmed by NMR and UV/Vis studies, reported in Chapter 3. The complexes were synthesized as described in Chapter 3. The kinetic study was performed under *pseudo* first-order conditions with [L] >> *fac*-[$Mn(CO)_3$(L,L'-Bid)(MeOH)]. It was observed that the rate of the reactions increased as the concentration of the entering ligand increased. On the basis of the results the following general mechanism is predicted:

$$[Mn(CO)_3(L,L'\text{-Bid})(MeOH)]^n + L \rightleftharpoons [Mn(CO)_3(L,L'\text{-Bid})(L)]^n + MeOH$$

with L,L'-Bid = Phen, Bipy, Pico, 2,4-Quin, L = Py, TU, Br^-, and n = 0, +1. The rate of the reaction is given by:

$$\text{Rate} = k_1 \textit{fac}\text{-}[Mn(L,L'\text{-Bid})(CO)_3(MeOH)][L]^n - k_{-1} \textit{fac}\text{-}[Mn(L,lL'\text{-Bid})(CO)_3(L)]^n \qquad \text{Eq. 5}$$

where k_1 represents the forward reaction and k_{-1} represents the reverse reaction. *fac*-[$Mn(CO)_3$(L,L'-Bid)(MeOH)] is the complex and *fac*-[Mn(L,L'-Bid)$(CO)_3$(L)] is the substituted product and [L] is the entering ligand. By using the *pseudo* first-order conditions [L] >> *fac*-[$Mn(CO)_3$(L,L'-Bid)(MeOH)], Equation 5 is reduced to

$$k_{obs} = k_1[L] + k_{-1} \qquad \text{Eq. 6}$$

where k_{obs} is the observed rate constant. The equation holds for the equilibrium reactions and then the equilibrium constant is given by:

$$K_1 = \frac{k_1}{k_{-1}} \qquad \text{Eq. 7}$$

5.3.1 Substitution reactions of *fac*-$[Mn(CO)_3(Phen)(MeOH)]^+$

The reaction between *fac*-$[Mn(CO)_3(Phen)(MeOH)]^+$ and three different ligands are performed in methanol. These entering ligands are pyridine (Py), thiourea (TU) and NaBr (Br^-). The synthesis of *fac*-$[Mn(CO)_3(Phen)(MeOH)]^+$ is described in Chapter 3. The kinetic study was performed at four different temperatures namely 15.0 °C, 25.0 °C,

35.0 °C, and 45.0 °C. Initial experiments indicated that the complex was stable in methanol for several hours.

5.3.1.1 Pyridine

The reaction between *fac*-$[Mn(CO)_3(Phen)(MeOH)]^+$ and pyridine was performed in methanol at four different temperatures. In Figure 5.3 the UV/vis spectrum is illustrated showing the reaction between *fac*-$[Mn(CO)_3(Phen)(MeOH)]^+$ and pyridine (0.2 M) at 25.0 °C in methanol.

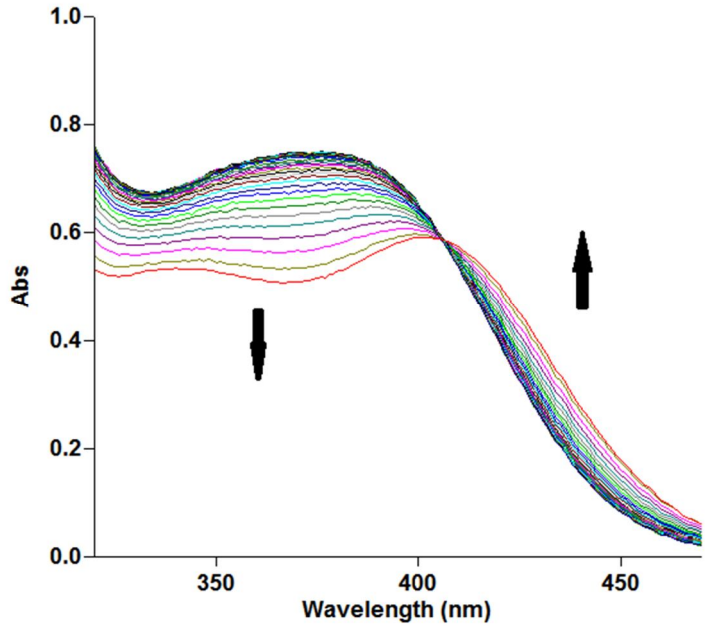

Figure 5.3: Typical UV/vis spectral change of the reaction between *fac*-$[Mn(CO)_3(Phen)(MeOH)]^+$ and pyridine (0.2 M) at 25.0 °C. [Mn] = 5 x 10^{-4} M.

The k_{obs} *vs*. [Py] data at the four different temperatures are given in Figure 5.4. In Table 5.1 the rate constants and the equilibrium constants, which were kinetically determined, are reported.

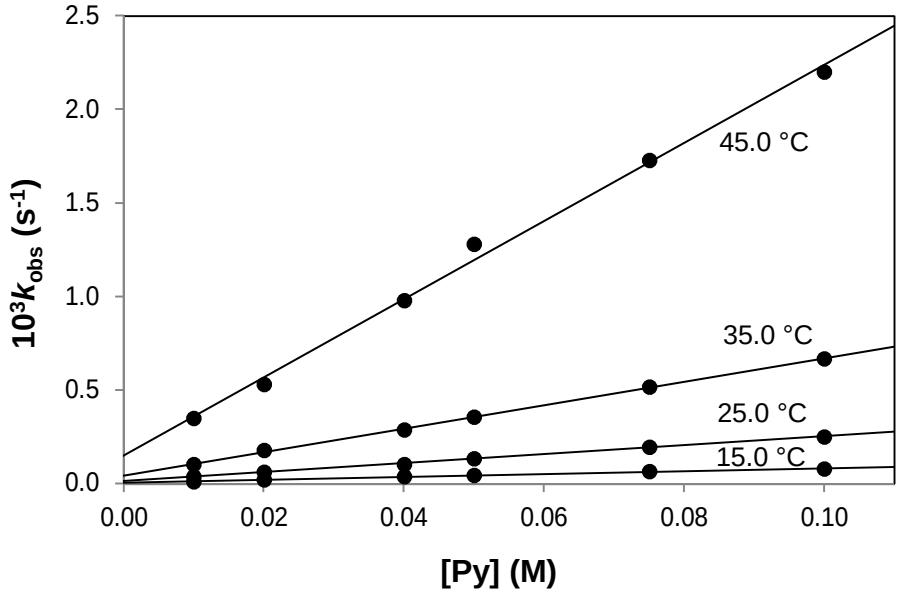

Figure 5.4: The k_{obs} *vs.* [Py] data for the reaction between *fac*-$[Mn(CO)_3(Phen)(MeOH)]^+$ and pyridine at four different temperatures. [Mn] = 5 x 10^{-4} M, λ = 370 nm.

Table 5.1: Summary of the rate constants and activation parameters obtained in the reaction between *fac*-$[Mn(CO)_3(Phen)(MeOH)]^+$ and Py at different temperatures.

	15.0 °C	**25.0 °C**	**35.0 °C**	**45.0 °C**
$10^3 k_1$ ($M^{-1}s^{-1}$)	0.76 ± 0.03	2.39 ± 0.05	6.27 ± 0.09	20.8 ± 0.6
$10^5 k_{-1}$ (s^{-1})	0.7 ± 0.2	1.5 ± 0.3	4.5 ± 0.5	15 ± 4
K_1 (M^{-1})	109 ± 31	159 ± 32	139 ± 16	139 ± 37
$\Delta H^{\dagger}$ (kJ.mol^{-1})	80432 ± 3221			
$\Delta S^{\dagger}$(J.K^{-1}.mol^{-1})	-27 ± 2			

Figure 5.5 shows the Eyring plot, from which the $\Delta H^{\dagger}$ = 80432 ± 3221 and $\Delta S^{\dagger}$ = -27 ± 2 values were obtained.

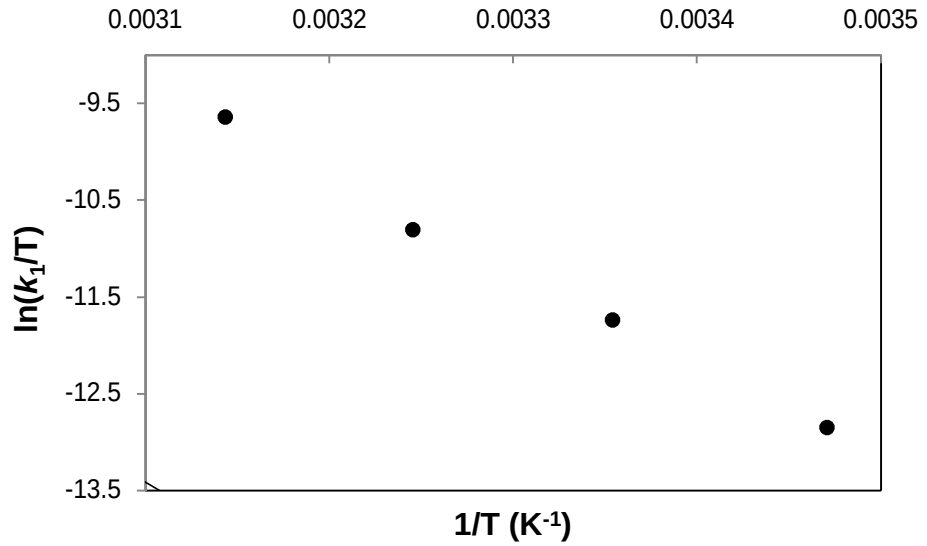

Figure 5.5: Eyring plot of ln(k_1/T) *vs.* 1/T for the reaction between *fac*-[Mn(CO)$_3$(Phen)(MeOH)]+ and Py at four different temperatures.

5.3.1.2 Thiourea

The reaction between *fac*-[Mn(CO)$_3$(Phen)(MeOH)]$^+$ and thiourea was performed using a concentration of 5 x 10^{-4} M of the manganese complex and six different thiourea concentrations ranging from 0.2 M to 0.02 M in methanol. The reaction was performed at four different temperatures: 15.0 °C, 25.0 °C, 35.0 °C and 45°C. Figure 5.6 shows a typical UV/vis spectrum of the reaction.

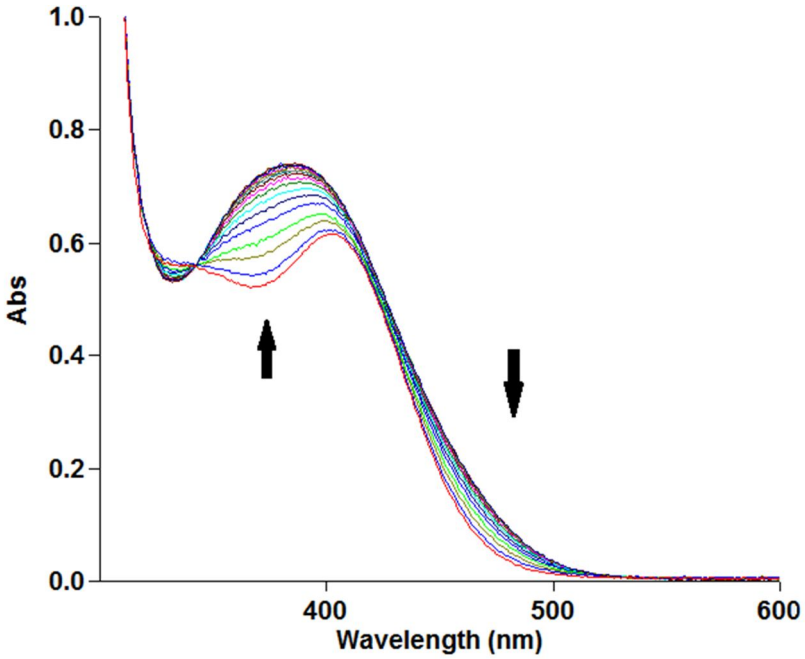

Figure 5.6: Typical UV/vis spectral change for the reaction between *fac*-[Mn(CO)$_3$(Phen)(MeOH)]$^+$ and thiourea (0.2 M) at 25.0 °C. [Mn] = 5 x 10^{-4} M.

The k_{obs} *vs*. [TU] data at four temperatures for the reaction between *fac*-$[Mn(CO)_3(Phen)(MeOH)]^+$ and thiourea are given in Figure 5.7.

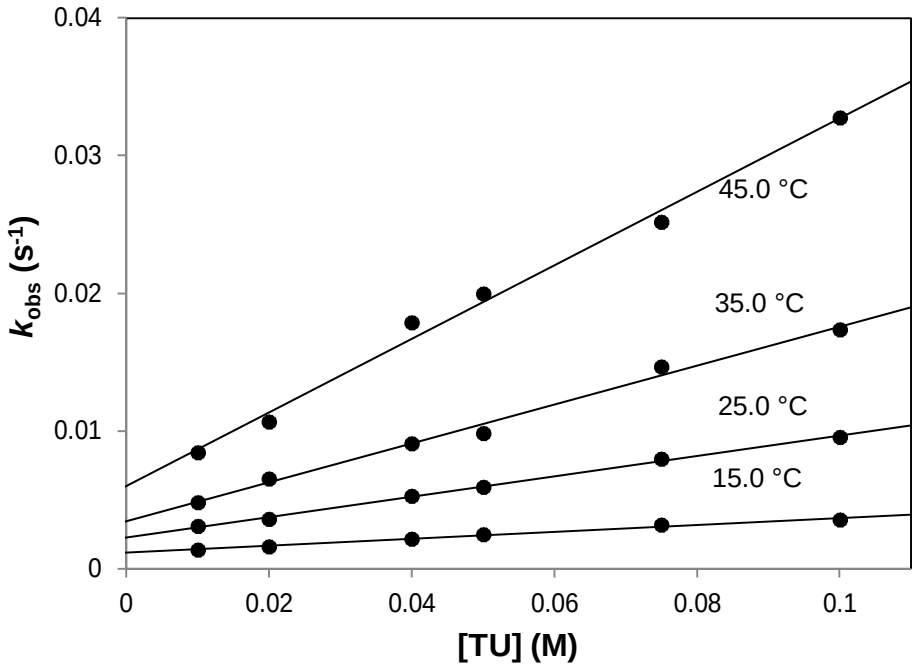

Figure 5.7: The k_{obs} *vs*. [TU] data for the reaction between *fac*-$[Mn(CO)_3(Phen)(MeOH)]^+$ and thiourea at four different temperatures. [Mn] = 5 x 10^{-4} M, λ = 375 nm.

Table 5.2: Summary of the rate constants and activation parameters obtained in the reaction between *fac*-$[Mn(CO)_3(Phen)(MeOH)]^+$ and TU at different temperatures.

	15.0 °C	**25.0 °C**	**35.0 °C**	**45.0 °C**
$10^2 k_1$ ($M^{-1}s^{-1}$)	2.5 ± 0.2	7.4 ± 0.2	14.1 ± 0.6	27 ± 1
$10^3 k_{-1}$ (s^{-1})	1.2 ± 0.1	2.3 ± 0.1	3.5 ± 0.3	6 ± 6
K_1 (M^{-1})	21 ± 2	32 ± 2	40 ± 4	45 ± 5
$\Delta H^{\dagger}$ (kJ.mol^{-1})	56994 ± 4681			
$\Delta S^{\dagger}$ (J.K^{-1}.mol^{-1})	-77 ± 15			

In Table 5.2 the rate constants and activation parameters obtained for the reaction between *fac*-$[Mn(CO)_3(Phen)(MeOH)]^+$ and [TU] at four different temperatures are given. By using the Eyring equation, the Eyring plot in Figure 5.8 is obtained and the activation paramters $\Delta H^{\dagger}$ = 56994 ± 4681 and $\Delta S^{\dagger}$ = -77 ± 15 are reported.

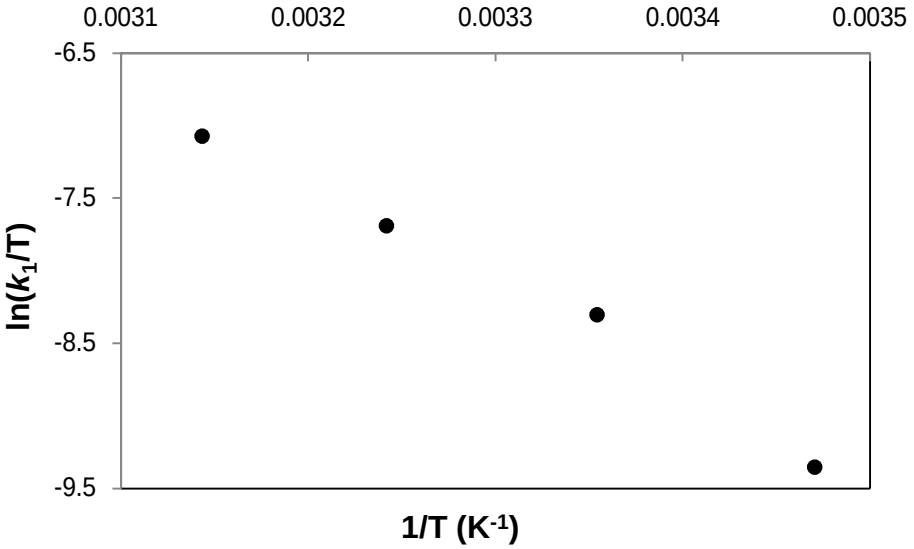

Figure 5.8: Eyring plot of ln(k_1/T) *vs.* 1/T for the reaction between *fac*-[Mn(CO)$_3$(Phen)(MeOH)]$^+$ and TU at four different temperatures.

5.3.1.3 Bromide (Br^-)

This reaction between *fac*-[Mn(CO)$_3$(Phen)(MeOH)]$^+$ and bromide ions was performed in methanol at four different temperatures, 15.0 °C, 25.0 °C, 35.0 °C and 45.0 °C. Figure 5.9 is a typical UV/vis spectrum of the reaction with bromide ions (0.2 M) at 25.0 °C in methanol.

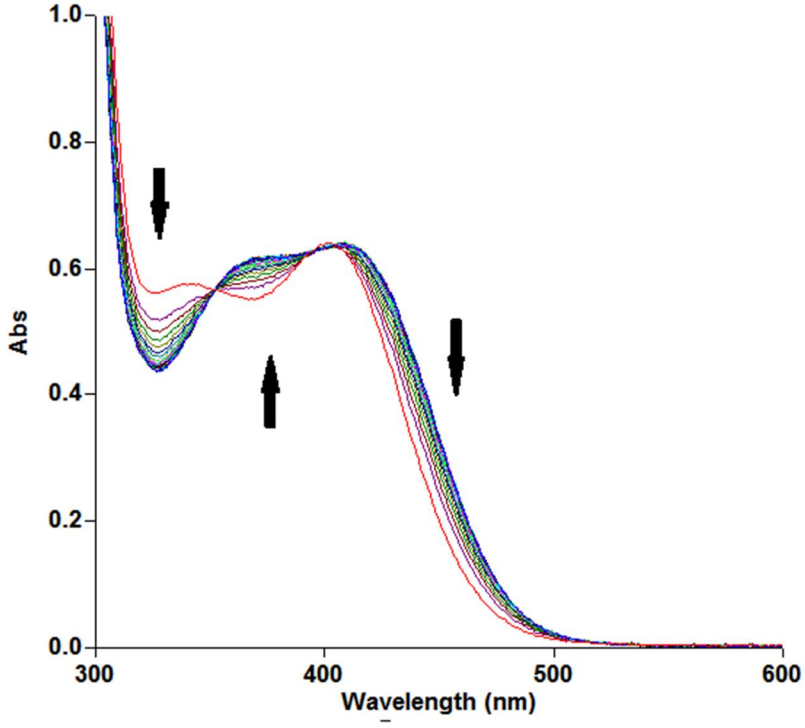

Figure 5.9: UV/vis spectral change for the reaction between *fac*-[Mn(CO)$_3$(Phen)(MeOH)]$^+$ and bromide ions (0.2 M) at 25°C, in methanol. [Mn] = 5 x 10^{-4} M.

The k_{obs} values were plotted against the six different bromide ion concentrations ranging from 0.02 M to 0.2 M. The k_{obs} *vs*. bromide ion concentration data for all the temperatures are given in Figure 5.10.

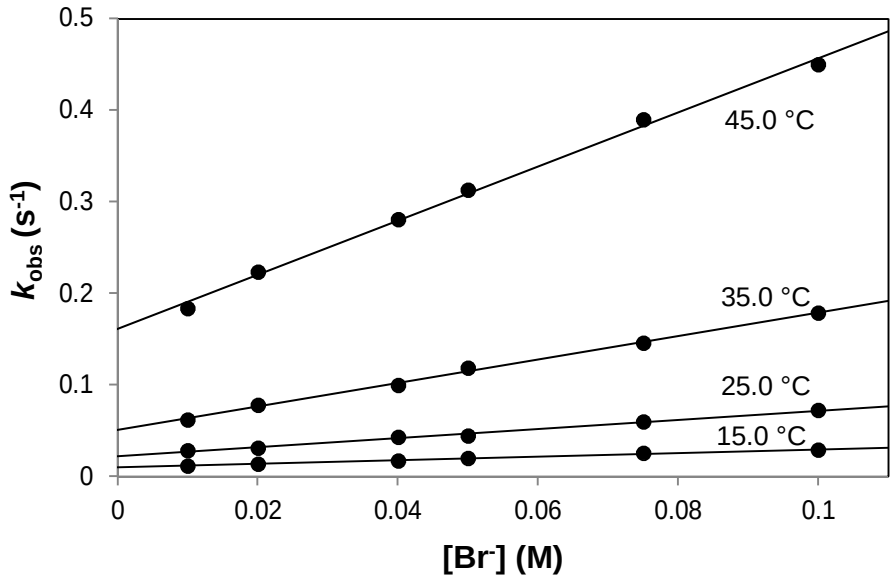

Figure 5.10: The k_{obs} *vs*. [Br^-] data for the reaction between *fac*-[$Mn(CO)_3(Phen)(MeOH)]^+$ and bromide ions at four different temperatures. [Mn] = 5 x 10^{-4} M, λ = 370 nm.

Table 5.3 lists the rate constants and activation parameters obtained for the reaction between *fac*-[$Mn(CO)_3(Phen)(MeOH)]^+$ and [Br^-] at four different temperatures. The Eyring plot is given in Figure 5.11. The activation parameters obtained were: $\Delta H^{\dagger}$ = 66657 ± 646 and $\Delta S^{\dagger}$ = -27 ± 2.

Table 5.3: Summary of the rate constants and activation parameters obtained in the reaction between *fac*-[$Mn(CO)_3(Phen)(MeOH)]^+$ and Br^- at different temperatures.

	15.0 °C	**25.0 °C**	**35.0 °C**	**45.0 °C**
k_1 ($M^{-1}s^{-1}$)	0.196 ± 0.009	0.50 ± 0.02	1.28 ± 0.03	2.95 ± 0.05
k_{-1} (s^{-1})	0.0102 ± 0.0006	0.022 ± 0.001	0.051 ± 0.002	0.16 ± 0.01
K_1 (M^{-1})	19 ± 1	23 ± 1	25 ± 18	18 ± 1
$\Delta H^{\dagger}$ (kJ.mol^{-1})	66657 ± 646			
$\Delta S^{\dagger}$ (J.K^{-1}.mol^{-1})	-27 ± 2			

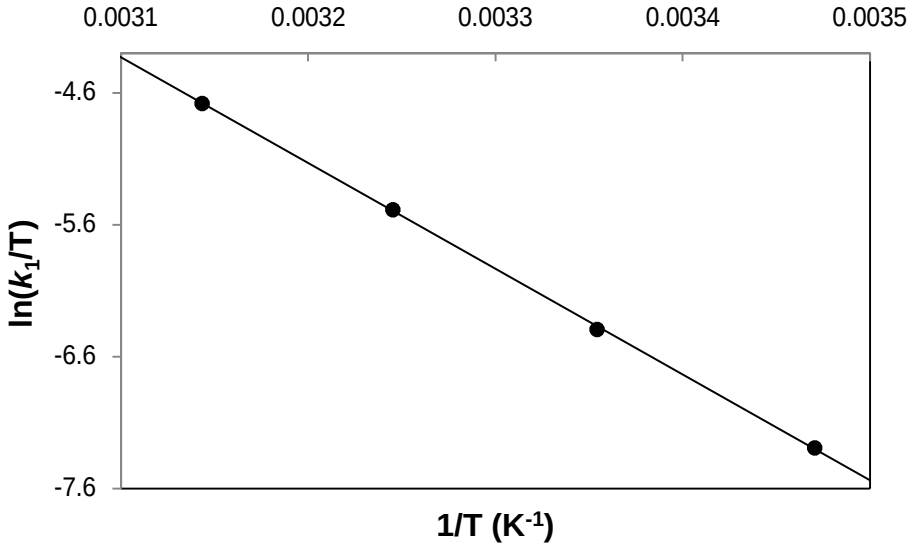

Figure 5.11: Eyring plot of ln(k_1/T) *vs.* 1/T for the reaction between *fac*-[Mn(CO)$_3$(Phen)(MeOH)]$^+$ and Br$^-$ at four different temperatures.

5.3.2 Substitution reactions of *fac*-[Mn(CO)$_3$(Bipy)(MeOH)]$^+$

The procedure for the synthesis of *fac*-[Mn(CO)$_3$(Bipy)(MeOH)]$^+$ is described in Chapter 3. The complex was dissolved in methanol and proved to be stable in methanol for several hours. Reactions between *fac*-[Mn(CO)$_3$(Bipy)(MeOH)]$^+$ and pyridine (Py), thiourea (TU) and NaBr (Br$^-$ ions) were performed at 25.0 °C. Figure 5.12 illustrates a typical reaction between *fac*-[Mn(CO)$_3$(Bipy)(MeOH)]$^+$ and pyridine at 25.0 °C in methanol. The k_{obs} values were obtained by fitting the rate data to Equation 3.

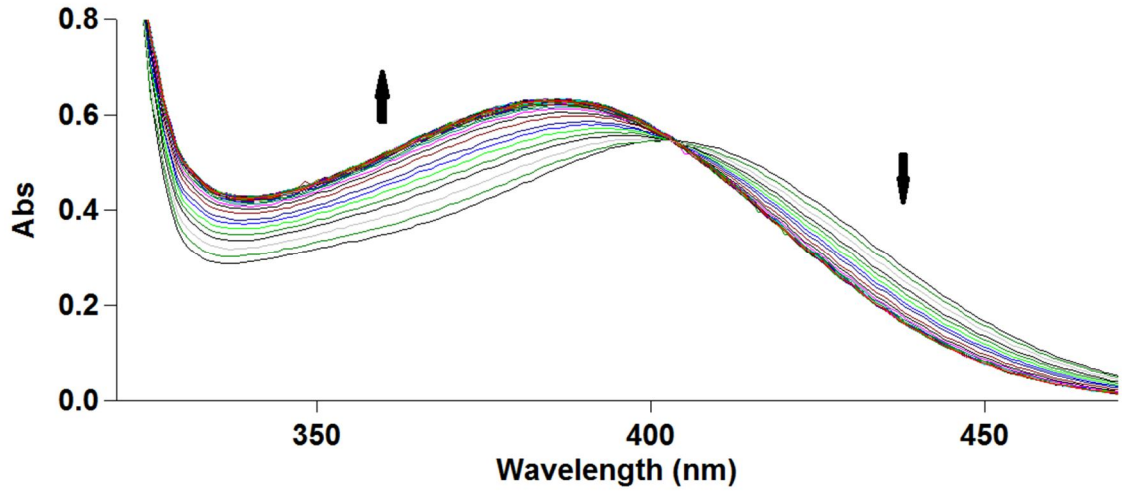

Figure 5.12: UV/vis spectral change of the reaction between *fac*-[Mn(CO)$_3$(Bipy)(MeOH)]$^+$ and pyridine (0.2 M) at 25.0 °C in methanol. [Mn] = 5 × 10^{-4} M.

The k_{obs} *vs.* [Py], [TU] and [Br^-] data at 25.0 °C are illustrated in Figure 5.13. A summary of the k_1, k_{-1} and K_1 values are given in Table 5.4.

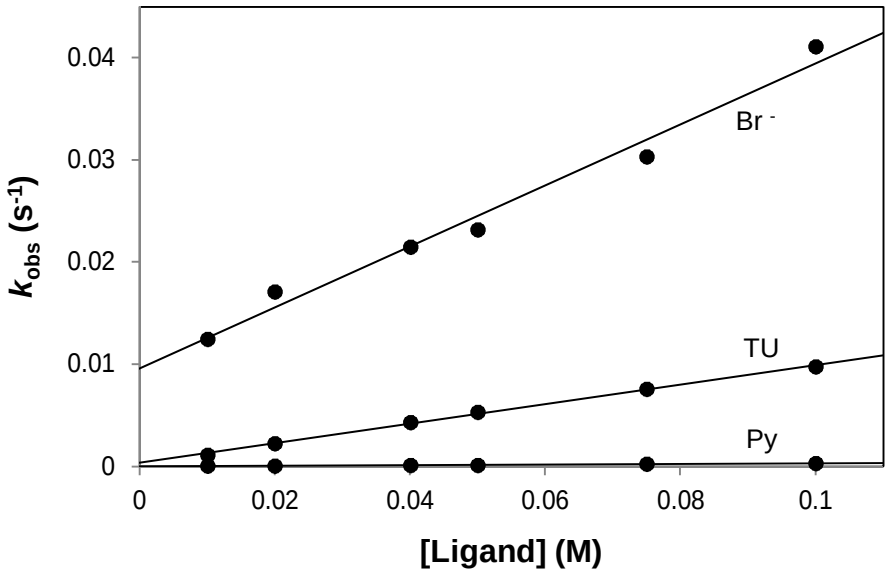

Figure 5.13: The k_{obs} *vs.* [Py], [TU] and [Br^-] data for the reactions between *fac*-[$Mn(CO)_3(Bipy)(MeOH)]^+$ and pyridine, thiourea and bromide ions at 25.0 °C. [Mn] =5 × 10^{-4} M, λ (Pyridine) = 370 nm , λ (Thiourea) = 365 nm , λ (Bromide) = 445 nm.

Table 5.4: A summary of the rate constants obtained in the reactions between *fac*-[$Mn(CO)_3(Bipy)(MeOH)]^+$ and Py, TU and Br^- ions. [Ligand] = 0.02 M – 0.2 M.

	[Py]	[TU]	[Br^-]
10^2 k_1 ($M^{-1}s^{-1}$)	0.293 ± 0.009	9.5 ± 0.2	31 ± 1
10^3 k_{-1} (s^{-1})	0.9 ± 0.5	0.04 ± 0.01	9.7 ± 0.6
K_1 (M^{-1})	3 ± 2	2375 ± 596	32 ± 2

5.3.3 Summary of substitution reactions of *fac*-[$Mn(CO)_3$(N,N'-bid)$(MeOH)]^+$ complexes

The first order rate constants for the substitution reactions of *fac*-[$Mn(CO)_3(Bipy)(MeOH)]^+$ and *fac*-[$Mn(CO)_3(Phen)(MeOH)]^+$ with different entering ligands, show a general trend of $k_1(Br^-) > k_1(TU) > k_1(Py)$.

- For the substitution reactions with pyridine at 25.0 °C, k_1 was reported as 2.93 × 10^{-3} ± 0.09 $M^{-1}s^{-1}$ for *fac*-[$Mn(CO)_3(Bipy)(MeOH)]^+$ and as 2.39 × 10^{-3} ± 0.05 $M^{-1}s^{-1}$ for *fac*-[$Mn(CO)_3(Phen)(MeOH)]^+$ complexes respectively. Similarly

for the reactions with thiourea and Br^- ions at 25.0 °C with values of 95 × 10^3 ± 2 $M^{-1}s^{-1}$ and 74 × 10^3 ± 2 $M^{-1}s^{-1}$ for thiourea, and for Br^- values of 31 × 10^2 ± 1 $M^{-1}s^{-1}$ and 50 × 10^2 ± 2 $M^{-1}s^{-1}$ respectively.

- Overall, the reactions showed that the 1,10-phenanthroline complex was faster than the 2,2'-bipyridyl complex. It is expected since 1,10-phenanthroline has an extra ring system compared to 2,2'-bipyridyl.

5.3.4 Substitution reactions of *fac*-[Mn(CO)$_3$(Pico)(MeOH)]

The reaction between *fac*-[Mn(CO)$_3$(Pico)(MeOH)] and three different entering ligands was performed in methanol, at four different temperatures. These entering ligands are pyridine (Py), thiourea (TU) and NaBr (Br^-). The synthesis of *fac*-[Mn(CO)$_3$(Pico)(MeOH)] is described in Chapter 3. Initial studies were performed and the complex revealed to be stable in methanol for several hours.

5.3.4.1 Pyridine

The reaction between *fac*-[Mn(CO)$_3$(Pico)(MeOH)] and pyridine was performed in methanol at four different temperatures. The UV/vis spectral change for the reaction between *fac*-[Mn(CO)$_3$(Pico)(MeOH)] and pyridine (0.2 M) at 15.0 °C is given in Figure 5.14. The k_{obs} *vs.* [Py] data for the different temperatures are given in Figure 5.15.

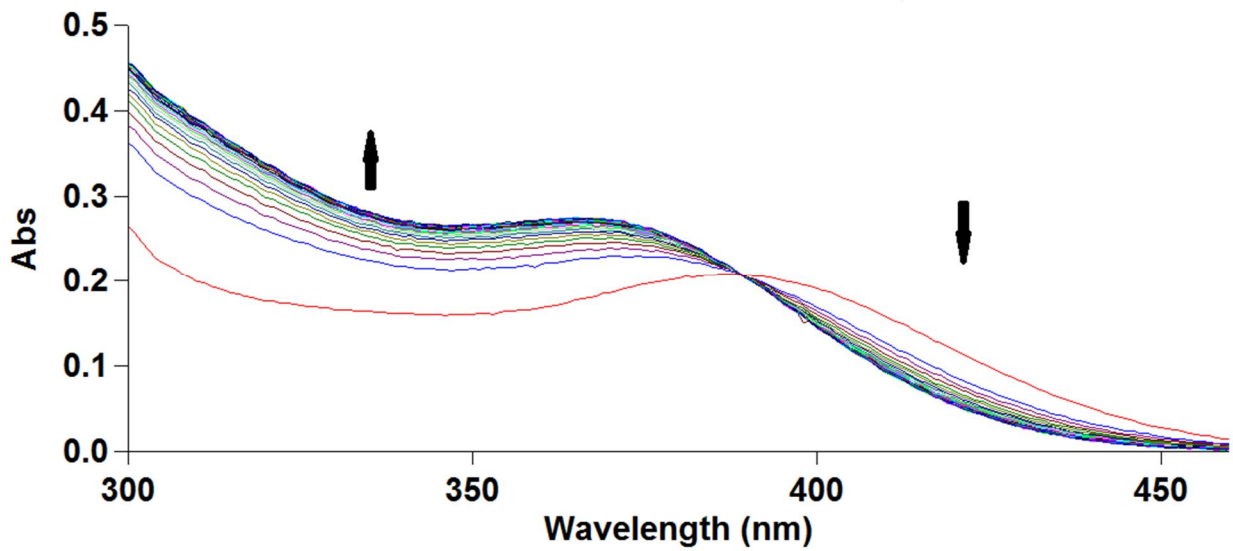

Figure 5.14: UV/vis spectral change for the reaction between *fac*-[Mn(CO)$_3$(Pico)(MeOH)] and pyridine (0.2 M) at 15.0 °C, methanol. [Mn] = 3 x 10^{-3} M.

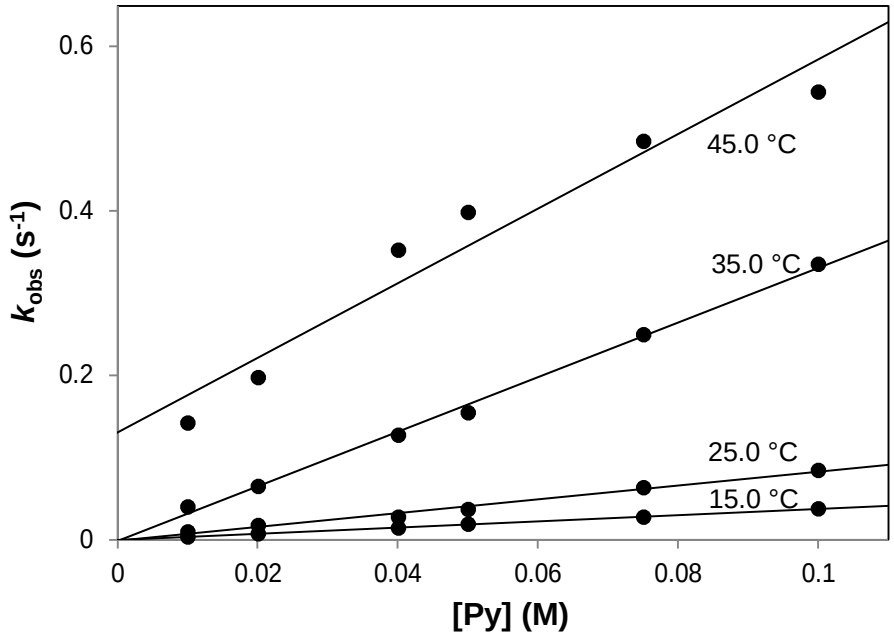

Figure 5.15: The k_{obs} *vs.* [Py] data for the reaction between *fac*-[Mn(CO)$_3$(Pico)(MeOH)] and pyridine at all four temperatures. [Mn] = 3 x 10^{-3} M, λ = 365 nm.

The kinetic data obtained is given in Table 5.5 for the reactions at all four temperatures. From the Eyring plot (Figure 5.16) the activation parameters, $\Delta H^{\dagger}$ = 60576 ± 1099 and $\Delta S^{\dagger}$ = -42 ± 4 are obtained.

Table 5.5: A summary of the rate constants and activation parameters obtained in the reaction between *fac*-[Mn(CO)$_3$(Pico)(MeOH)] and Py at four different temperatures.

	15.0 °C	**25.0 °C**	**35.0 °C**	**45.0 °C**
k_1 ($M^{-1}s^{-1}$)	0.378 ± 0.02	0.94 ± 0.01	2.19 ± 0.03	4.49 ± 0.08
$10^4 k_{-1}$ (s^{-1})	0.6 ± 0.1	1.3 ± 0.7	16 ± 5	62 ± 4
K_1 (M^{-1})	6300 ± 1051	7231 ± 3894	1369 ± 428	724 ± 49
$\Delta H^{\dagger}$ (kJ.mol^{-1})	60576 ± 1099			
$\Delta S^{\dagger}$ (J.K^{-1}.mol^{-1})	-42 ± 4			

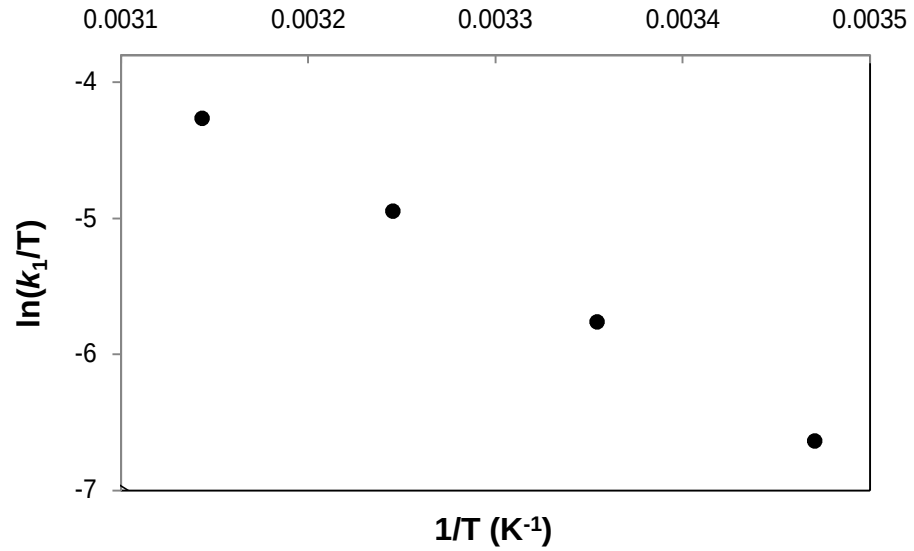

Figure 5.16: Eyring plot of ln(k_1/T) *vs*. 1/T for the reaction between *fac*-[Mn(CO)$_3$(Pico)(MeOH)] and pyridine at four different temperatures.

5.3.4.2 Thiourea

The reaction between *fac*-[Mn(CO)$_3$(Pico)(MeOH)] and thiourea was performed with a 5 x 10^{-4} M manganese complex solution and six different thiourea concentrations ranging from 0.2 M to 0.02 M in methanol. The reactions were performed at four different temperatures, 15.0 °C, 25.0 °C, 35.0 °C and 45.0 °C. Figure 5.17 illustrates the UV/vis spectrum of the reaction between *fac*-[Mn(CO)$_3$(Pico)(MeOH)] and thiourea (0.15 M) at 25°C.

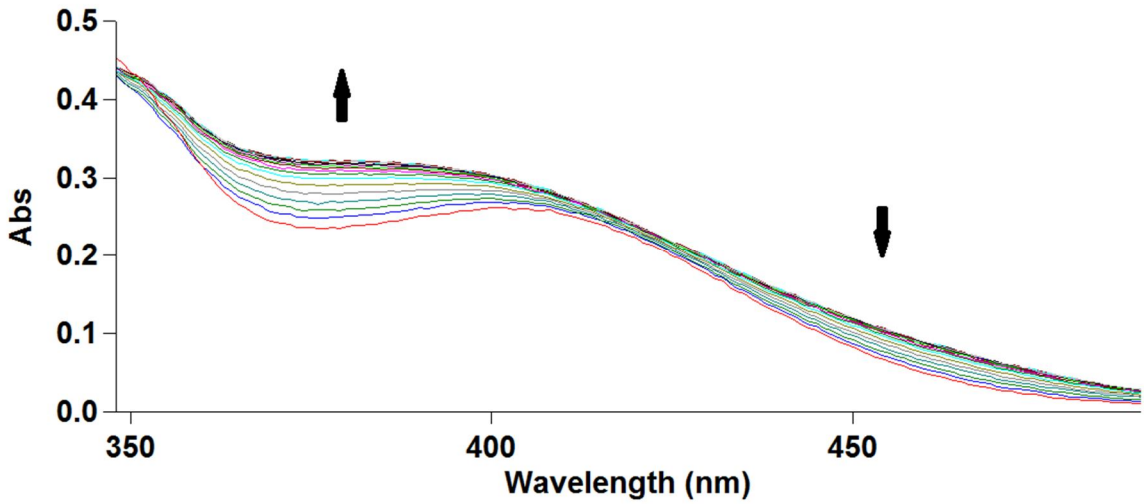

Figure 5.17: UV/vis spectral change for the reaction between *fac*-[Mn(CO)$_3$(Pico)(MeOH)] and TU in methanol at 25.0 °C. [Mn] = 3 x 10^{-3} M, [TU] = 0.15 M.

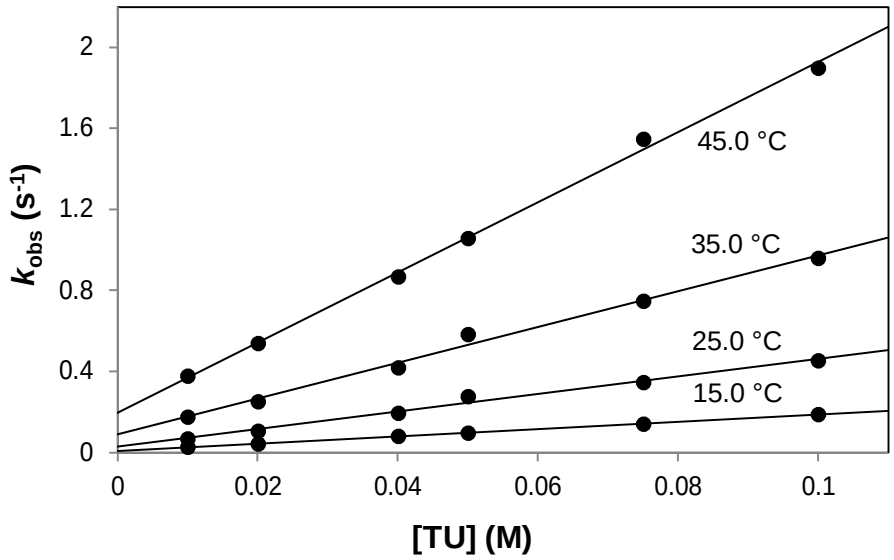

Figure 5.18: The k_{obs} *vs.* [TU] data for the reaction between *fac*-[Mn(CO)$_3$(Pico)(MeOH)] and thiourea at all four temperatures. [Mn] = 3 x 10^{-3} M, λ = 385 nm.

In Figure 5.18 the k_{obs} *vs.* [TU] data at the different temperatures are illustrated. The rate constants and activation parameters for the reaction are given in Table 5.6. Figure 5.19 represents the Eyring plot of the reaction, with the activation parameters obtained: $\Delta H^{\dagger}$ = 54339 ± 1786 and $\Delta S^{\dagger}$ = -51 ± 6.

Table 5.6: A summary of the rate constants and activation parameters obtained in the reaction between *fac*-[Mn(CO)$_3$(Pico)(MeOH)] and TU at four different temperatures.

	15.0°C	**25.0°C**	**35.0°C**	**45.0°C**
$\boldsymbol{k_1}$ ($M^{-1}s^{-1}$)	1.78 ± 0.02	4.31 ± 0.02	8.8 ± 0.4	16.8 ± 0.2
$\boldsymbol{k_{-1}}$ (s^{-1})	0.01 ± 0.05	0.025 ± 0.001	0.09 ± 0.02	0.21 ± 0.02
$\mathbf{K_1}$ (M^{-1})	178 ± 89	172 ± 7	98 ± 22	80 ± 8
$\Delta\mathbf{H}^{\dagger}$ ($kJ.mol^{-1}$)	54339 ± 1786			
$\Delta\mathbf{S}^{\dagger}$ ($J.K^{-1}.mol^{-1}$)	-51 ± 6			

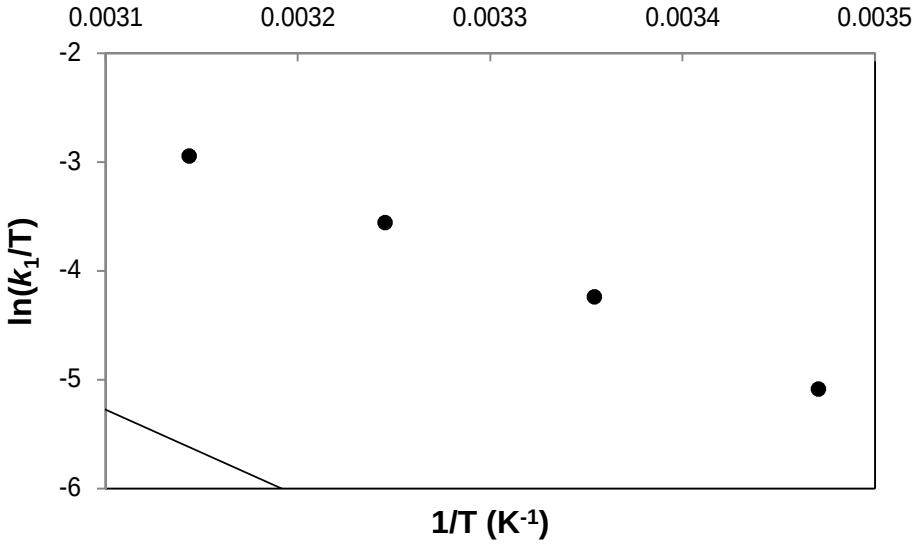

Figure 5.19: Eyring plot of ln(k_1/T) *vs*. 1/T for the reaction between *fac*-[Mn(CO)$_3$(Pico)(MeOH)] and thiourea at four different temperatures.

5.3.4.3 Bromide (Br^-)

This reaction between *fac*-[Mn(CO)$_3$(Pico)(MeOH)] and bromide ions was performed in methanol for all four different temperatures, 15.0 °C, 25.0 °C, 35.0 °C and 45.0 °C. The spectral change of the reaction is represented in Figure 5.20. The k_{obs} values were plotted against the six different bromide concentrations ranging from 0.02 M to 0.2 M. Figure 5.21 represents the plot of k_{obs} *vs*. [Br^-] for all the temperatures.

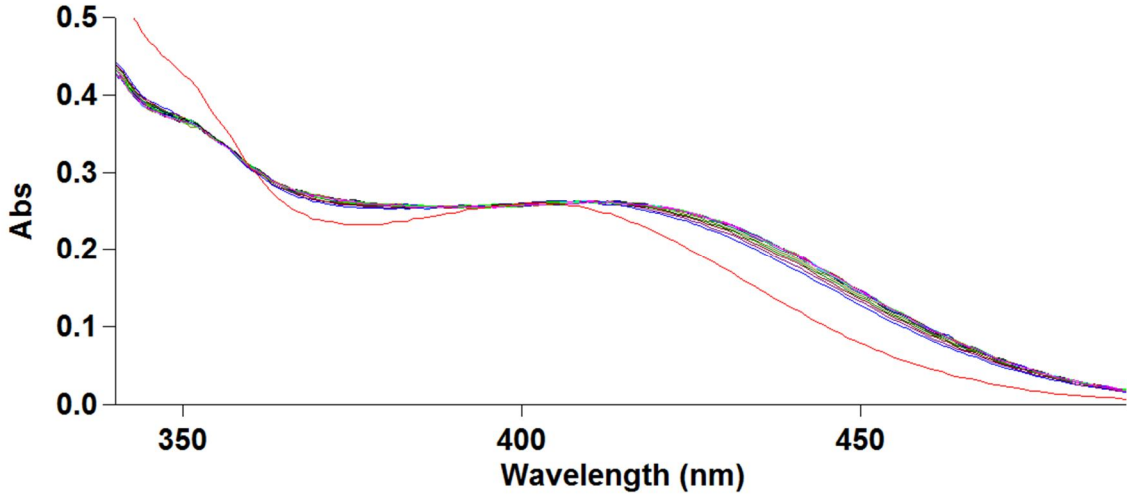

Figure 5.20: UV/vis spectral change for the reaction between *fac*-[Mn(CO)$_3$(Pico)(MeOH)] and Br^- in methanol at 25.0 °C. [Mn] = 3 x 10^{-3} M [Br^-] = 0.2 M.

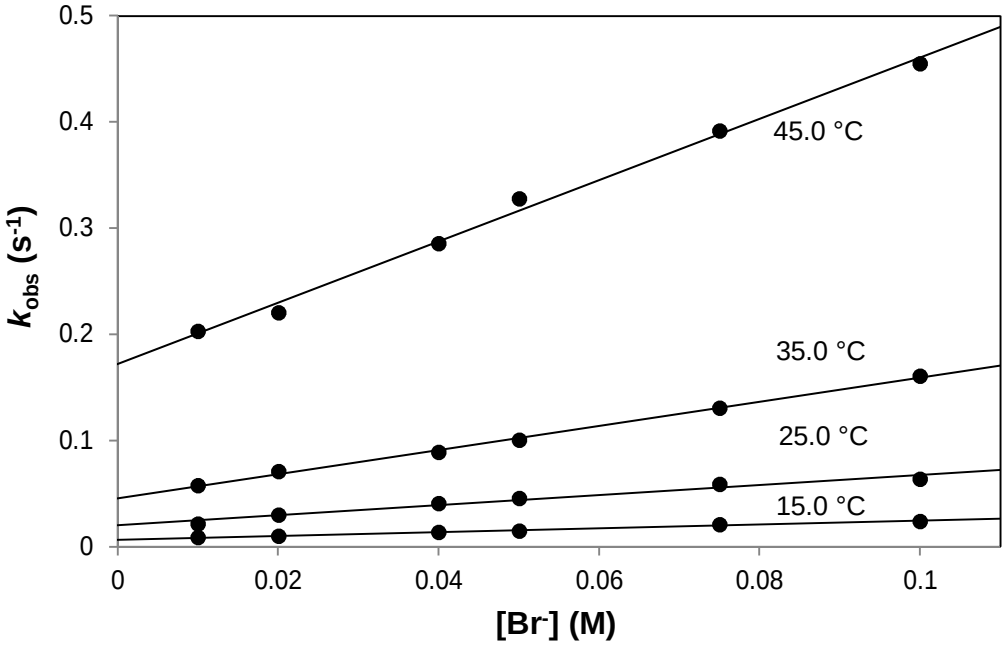

Figure 5.21: The k_{obs} *vs*. [Br^-] data for the reaction between *fac*-[$Mn(CO)_3$(Pico)(MeOH)] and bromide ions at all four temperatures. [Mn] = 3 x 10^{-3} M, λ = 415 nm.

Table 5.7: A summary of the rate constants and activation parameters obtained in the reaction between *fac*-[$Mn(CO)_3$(Pico)(MeOH)] and Br^- at four different temperatures.

	15.0°C	**25.0°C**	**35.0°C**	**45.0°C**
k_1 ($M^{-1}s^{-1}$)	1.78 ± 0.02	0.47 ± 0.04	1.12 ± 0.05	2.9 ± 0.1
k_{-1} (s^{-1})	0.010 ± 0.005	0.020 ± 0.002	0.047 ± 0.003	0.17 ± 0.06
K_1 (M^{-1})	178 ± 89	24 ± 3	24 ± 2	17 ± 6
$\Delta H^{\dagger}$ ($kJ.mol^{-1}$)	67882 ± 1548			
$\Delta S^{\dagger}$ ($J.K^{-1}.mol^{-1}$)	-24 ± 5			

In Table 5.7 the rate constants and activation parameters are given that were obtained by using Equation 3. From the Eyring plot (Figure 5.22) the parameters were determined: $\Delta H^{\dagger}$ = 67882 ± 1548 and $\Delta S^{\dagger}$ = -24 ± 5.

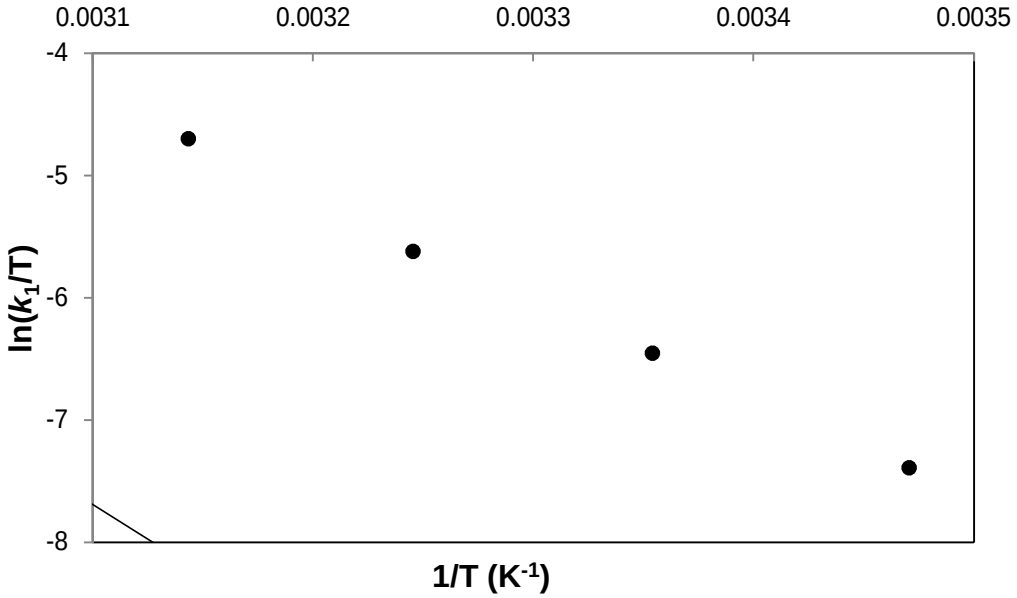

Figure 5.22: Eyring plot of ln(k_1/T) *vs*. 1/T for the reaction between *fac*-[Mn(CO)$_3$(Pico)(MeOH)] and bromide ions at four different temperatures.

5.3.5 Substitution reactions of *fac*-[Mn(CO)$_3$(2,4-Quin)(MeOH)]

fac-[Mn(CO)$_3$(2,4-Quin)(MeOH)] was synthesised using the method described in Chapter 3. Initial studies showed that *fac*-[Mn(CO)$_3$(2,4-Quin)(MeOH)] is stable in methanol for several hours. The kinetic investigation between *fac*-[Mn(CO)$_3$(2,4-Quin)(MeOH)] and pyridine and thiourea were performed in methanol at 25.0 °C using a stopped-flow device. The values for k_{obs} were obtained by fitting the rate data to Equation 3. The UV/vis spectral change for the reaction between *fac*-[Mn(CO)$_3$(2,4-Quin)(MeOH)] and bromide is illustrated in Figure 5.23.

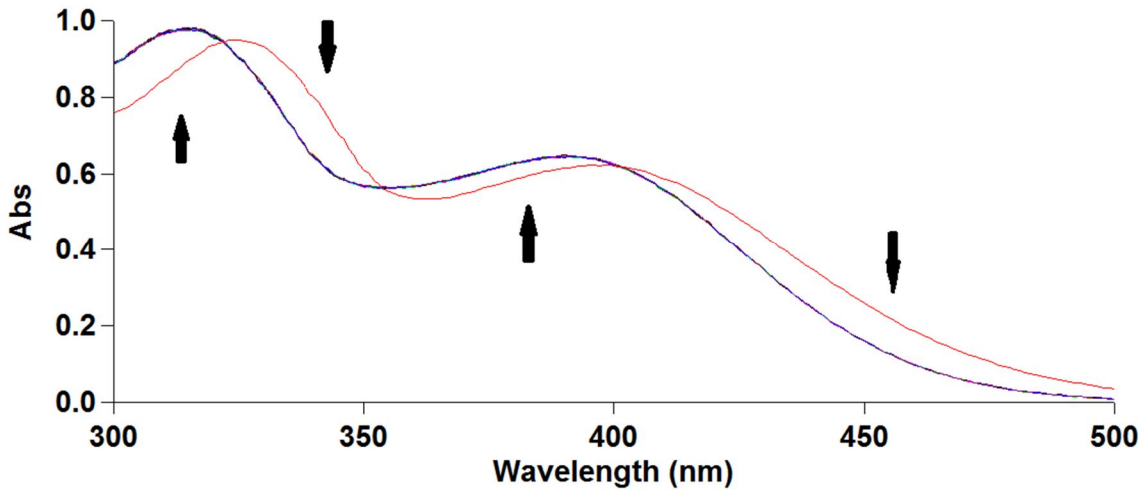

Figure 5.23: UV/Vis spectral change for the reaction between *fac*-[Mn(CO)$_3$(2,4-Quin)(MeOH)] and pyridine at 25.0 °C, in methanol. [Mn] = 2.5 × 10^{-4} M [Br] = 0.2 M.

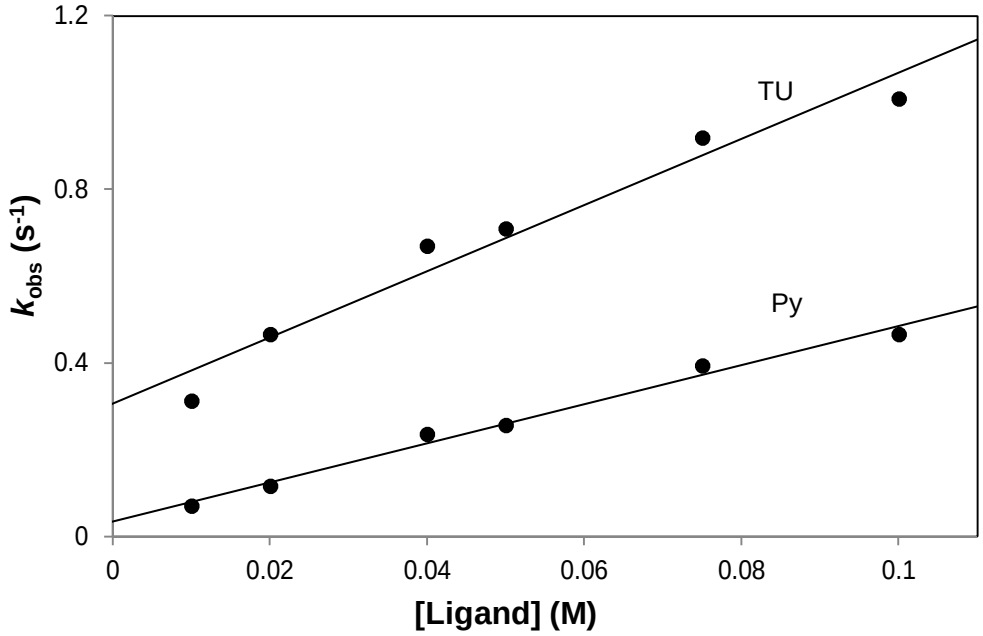

Figure 5.24: The k_{obs} vs. [Py] and [TU] for the reactions between *fac*-[Mn(CO)$_3$(2,4-Quin)(MeOH)] and pyridine as well as thiourea at 25.0 °C. [Mn] = 2.0 × 10^{-4}, λ (pyridine) = 380 nm and λ (thiourea) = 395 nm.

The k_{obs} *vs*. [Py] and [TU] data are illustrated in Figure 5.24 while a summary of the rate constants are given in Table 5.8.

Table 5.8: A summary of the rate constants for the reactions between *fac*-[Mn(CO)$_3$(2,4-Quin)(MeOH)] and Py and TU at 25.0 °C.

	[Py]	[TU]
k_1 (M^{-1} s^{-1})	4.5 ± 0.2	7.6 ± 0.7
k_{-1} (s^{-1})	0.04 ±0.01	0.31 ±0.05
K_1 (M^{-1})	113 ± 29	24.5 ± 0.46

5.3.6 Summary of substitution reactions of *fac*-[Mn(CO)$_3$(N,O'-bid)(MeOH)] complexes

The first order rate constants for the reactions of the Mn (I) complexes with N,O-bidentate ligands also follow a trend similar to that obtained with the N,N'-bidentate complexes with k_1 (TU) > k_1 (Py). Unfortunately we were unable to obtain reliable data

for the reaction of *fac*-[$Mn(CO)_3$(2,4-Quin)(MeOH)] with Br^-, under the same reaction conditions.

- In the case of the reactions between *fac*-[$Mn(CO)_3$(2,4-Quin)(MeOH)] and *fac*-[$Mn(CO)_3$(Pico)(MeOH)] with pyridine at 25.0 °C, the k_1 values were reported as 4.5 ± 0.2 $M^{-1}s^{-1}$ and 0.94 ± 0.01 $M^{-1}s^{-1}$ respectively. The substitution reactions of thiourea at 25.0 °C, the obtained values for k_1 are 7.6 ± 0.7 $M^{-1}s^{-1}$ and 4.31 ± 0.02 $M^{-1}s^{-1}$ respectively for the complexes.
- Overall, the 2,4-quinolinic acid complex was faster that the picolinic acid complex. This could be due to the fact that the quinolone has an extra phenyl ring than the picolinic.

5.4. Discussion

The k_1 values were reported as 2.93 × 10^{-3} ± 0.09 M^{-1} s^{-1} for *fac*-[$Mn(CO)_3$(Bipy)(MeOH)]$^+$ and 2.39 × 10^{-3} ± 0.05 M^{-1} s^{-1} for *fac*-[$Mn(CO)_3$(Phen)(MeOH)]$^+$ respectively with pyridine. Similarly for the reactions with thiourea and Br^- ions at 25.0 °C the k_1 values were 95 × 10^3 ± 2 $M^{-1}s^{-1}$ and 74 × 10^3 ± 2 M^{-1} s^{-1} for thiourea, and for Br^- the k_1 values were 31 × 10^2 ± 1 $M^{-1}s^{-1}$ and 50 × 10^2 ± 2 M^{-1} s^{-1} respectively. This follows a general trend of k_1 (Br^-) > k_1 (TU) > k_1 (Py). For the N,O-bidentate ligands the same trend was observed with the bromide reaction being the fastest, followed by thiourea and pyridine being the slowest. For pyridine as entering ligand the k_1 values for the reactions with *fac*-[$Mn(CO)_3$(2,4-Quin)(MeOH)] and *fac*-[$Mn(CO)_3$(Pico)(MeOH)] were reported as 4.5 ± 0.2 $M^{-1}s^{-1}$ and 0.94 ± 0.01 $M^{-1}s^{-1}$ respectively at 25.0 °C. With the thiourea as the entering ligand with the reactions at 25.0 °C, the obtained values for k_1 were 7.6 ± 0.7 $M^{-1}s^{-1}$ and 4.31 ± 0.02 $M^{-1}s^{-1}$ respectively for the complexes.

Table 5.9: Comparison of manganese(I) complexes with rhenium (I) complexes in their kineic studies at 25.0 °C.

	Constants	$Mn(CO)_3(Bipy)^a$	$Mn(CO)_3(Phen)^b$	$Re(CO)_3(Bipy)^c$	$Re(CO)_3(Phen)^d$
Br^-	k_1 ($M^{-1}s^{-1}$)	0.31 ± 0.01	0.50 ± 0.02	0.042 ±0.007	0.050 ±0.003
	10^3 k_{-1} (s^{-1})	9.7 ± 0.6	22 ± 1	0.62 ± 0.02	0.59 ± 0.03
	K_1 (M^{-1})	32 ± 2	23 ± 1	60 ± 1	75 ± 11
	$\Delta H^{\dagger}$ (kJ.mol^{-1})		66657 ± 646		
	$\Delta S^{\dagger}$ (J.K^{-1}.mol^{-1})		-27 ± 2		
Py	10^3 k_1 ($M^{-1}s^{-1}$)	2.93 ± 0.09	2.39 ± 0.05	0.96 ± 0.01	0.064 ± 0.003
	10^4 k_{-1} (s^{-1})	9 ± 5	0.15 ± 0.03	0.12 ± 0.01	0.058 ± 0.004
	K_1 (M^{-1})	3 ± 2	159 ± 32	80 ± 7	11.3± 0.9
	$\Delta H^{\dagger}$ (kJ.mol^{-1})		80432 ± 3221		
	$\Delta S^{\dagger}$ (J.K^{-1}.mol^{-1})		-27 ± 2		

a = *fac*-$[Mn(CO)_3(Bipy)(MeOH)]^+$, b = *fac*-$[Mn(CO)_3(Phen)(MeOH)]^+$, c = *fac*-$[Re(CO)_3(Bipy)(MeOH)]^+$, d = *fac*-$[Re(CO)_3(Phen)(MeOH)]^+$

By comparing the rate constants of the reactions between *fac*-$[Mn(CO)_3(Bipy)(MeOH)]^+$ and *fac*-$[Mn(CO)_3(2,4\text{-}Quin)(MeOH)]$ and pyridine, it can be seen that the 2,4-Quin complex reacted ~1500 times faster than the Bipy complex, with reported rate constants of 4.5 ± 0.2 M^{-1} s^{-1} and 2.93 × 10^{-3} ± 0.09 M^{-1} s^{-1} respectively. The rate constants of the reactions between *fac*-$[Mn(CO)_3(Bipy)(MeOH)]^+$ and *fac*-$[Mn(CO)_3(2,4\text{-}Quin)(MeOH)]$ and thiourea proved that the 2,4-quin complex was ~80 times faster than the Bipy complex, with k_1 values reported as 7.6 ± 0.7 M^{-1} s^{-1} and 9.5 × 10^{-2} ± 0.2 M^{-1} s^{-1}. The reactions of *fac*-$[Mn(CO)_3(Pico)(MeOH)]$ and *fac*-$[Mn(CO)_3(Phen)(MeOH)]^+$ proved that the N,O-bidentate complex was ~ 400 times faster in pyridine with k_1 values reported as 0.94 ± 0.01 M^{-1} s^{-1} and 2.39 × 10^{-3} ± 0.05 M^{-1} s^{-1} respectively and the reaction rate showing that the picolinic complex is ~ 58 times faster for thiourea. The rate constants are reported as 4.31 ± 0.02 M^{-1} s^{-1} for the picolinic complex and 7.4 × 10^{-2} ± 0.2 M^{-1} s^{-1} for the 1,10-phenanthroline complex. For the bromide reactions, the rate constants are almost similar with the k_1 values reported as 47 × 10^{-2} ± 4 $M^{-1}s^{-1}$ for the picolinic complex and 50 × 10^{-2} ± 2 M^{-1} s^{-1}. The reason for this could be the positive charge of the Phen complex.

Table 5.10: Comparison of N.O-bidentate ligand complexes of Mn (I) and Re (I) at 25.0 °C.

	Constants	[Mn(Pico)][a]	[Mn(2,4-Quin)][b]	[Re(Pico)][c]	[Re(2,4-Quin)][d]
Br⁻	$10^1 k_1$ ($M^{-1}s^{-1}$)	43.1± 0.2		0.118 ± 0.001	
	$10^3 k_{-1}$ (s^{-1})	25 ± 1		0.8 ± 0.1	
	K_1 (M^{-1})	172 ± 7		15 ± 2	
	$\Delta H^{\dagger}$ ($kJ.mol^{-1}$)	67882 ± 1548			
	$\Delta S^{\dagger}$ ($J.K^{-1}.mol^{-1}$)	-24 ± 5			
Py	$10^1 k_1$ ($M^{-1}s^{-1}$)	9.4 ± 0.1	45 ± 2	0.0159 ± 0.0001	0.031 ± 0.002
	$10^3 k_{-1}$ (s^{-1})	0.13 ± 0.07	40 ± 1	0.008 ± 0.001	0.051 ± 0.007
	K_1 (M^{-1})	7231 ± 3894	113 ± 29	199 ± 25	195 ± 97
	$\Delta H^{\dagger}$ ($kJ.mol^{-1}$)	60576 ± 1099		84 ± 1	
	$\Delta S^{\dagger}$ ($J.K^{-1}.mol^{-1}$)	-42 ± 4		-16 ± 4	

a = *fac*-[Mn(CO)$_3$(Pico)(MeOH)], b = *fac*-[Mn(CO)$_3$(2,4-Quin)(MeOH)], c = *fac*-[Re(CO)$_3$(Pico)(MeOH)], d = *fac*-[Re(CO)$_3$(2,4-Quin)(MeOH)]

In the comparison of the reaction rates of the Mn (I) complexes and the Re (I) complexes, it is observed that the Mn (I) complexes react much faster than the Re (I) complexes. The following comparisons are made from the data obtained at 25.0 °C.

- By comparing the Mn (I) and Re (I) Phen complexes it was found that the k_1 value is about 10 times larger for the Mn (I) complex with k_1 = 0.50 ± 0.02 M^{-1} s^{-1} for *fac*-[Mn(CO)$_3$(Phen)(MeOH)]$^+$ compared to the Re (I) complex with k_1 = 0.050 ± 0.003 M^{-1} s^{-1} for *fac*-[Re(CO)$_3$(Phen)(MeOH)]$^+$. The k_{-1} values, representing the reverse reaction, are reported as 22 × 10^{-3} ± 1 s^{-1} and 0.59 × 10^{-3} ± 0.03 s^{-1} for *fac*-[Mn(CO)$_3$(Phen)(MeOH)]$^+$ and *fac*-[Re(CO)$_3$(Phen)(MeOH)]$^+$ respectively. This shows the manganese reverse reaction was ~ 37 times faster than the rhenium reaction. The equilibrium constants are reported as 23 ± 1 M^{-1} for *fac*-[Mn(CO)$_3$(Phen)(MeOH)]$^+$ and 75 ± 11 M^{-1} for the *fac*-[Re(CO)$_3$(Phen)(MeOH)]$^+$ complex, indicating that the rhenium complex *fac*-[Re(CO)$_3$(Phen)Br] is much more stable than the corresponding manganese complex.
- The same trend is observed for the reactions between *fac*-[Mn(CO)$_3$(Bipy)(MeOH)]$^+$ and *fac*-[Re(CO)$_3$(Bipy)(MeOH)]$^+$ and bromide ions. The Mn (I) complex reacted ~10 times faster than the Re (I) analogue with k_1 = 0.31 ± 0.01 M^{-1} s^{-1} and 0.042 ± 0.007 M^{-1} s^{-1} for the manganese and rhenium complex respectively. The reverse reaction of *fac*-[Mn(CO)$_3$(Bipy)(MeOH)]$^+$ and *fac*-[Re(CO)$_3$(Bipy)(MeOH)]$^+$ has reported k_{-1} values of 9.7 × 10^{-3} ± 0.6 s^{-1} and 0.62 × 10^{-3} ± 0.02 s^{-1} respectively, with the value for the Mn (I) complex being ~15 times larger. The equilibrium constants are reported as 32 ± 2 M^{-1} and 60 ±

1 M^{-1} respectively, with the Re (I) complex more stable than the manganese analogue.

- In the reactions of the Phen complexes with pyridine, the Mn (I) complex reacted ~ 37 times faster than the Re (I) complex. *fac*-$[Mn(CO)_3(Phen)(MeOH)]^+$ has a reported k_1 value of 2.39 × 10^{-3} ± 0.05 $M^{-1}\,s^{-1}$ and *fac*-$[Re(CO)_3(Phen)(MeOH)]^+$ has a k_1 value of 0.064 × 10^{-3} ± 0.003 $M^{-1}\,s^{-1}$. The reverse reactions showed the manganese to be ~ 2 times faster with k_{-1} values reported as 0.15 × 10^{-4} ± 0.03 s^{-1} and 0.058 × 10^{-4} ± 0.004 s^{-1} respectively. The equilibrium constants were reported as 159 ± 32 M^{-1} for the *fac*-$[Mn(CO)_3(Phen)(MeOH)]^+$ complex and 11.3 ± 0.9 M^{-1} for the *fac*-$[Re(CO)_3(Phen)(MeOH)]^+$ complex. In this case, *fac*-$[Mn(CO)_3(Phen)(Py)]^+$ is a more stable complex than the rhenium counterpart.
- For the Bipy complexes, the Mn (I) complexes reacted ~3 times faster than the Re (I) complexes with pyridine as entering ligands. *fac*-$[Mn(CO)_3(Bipy)(MeOH)]^+$ in this reaction has a k_1 value of 2.93 × 10^{-3} ± 0.09 M^{-1} s^{-1} and *fac*-$[Re(CO)_3(Bipy)(MeOH)]^+$ has a k_1 value of 0.96 × 10^{-3} ± 0.01 $M^{-1}s^{-1}$. The reverse reactions showed the manganese to be ~ 75 times faster with k_{-1} values reported as 9 × 10^{-4} ± 5 s^{-1} and 0.12 × 10^{-4} ± 0.01 s^{-1} respectively. The equilibrium constants were reported as 3 ± 2 M^{-1} for the Mn (I) complex and 80 ± 7 M^{-1} for the Re (I) complex. Again the it is observed that the rhenium complex, *fac*-$[Re(CO)_3(Bipy)(Py)]^+$ is more stable than the manganese complex.
- The rate constants for *fac*-$[Mn(CO)_3(2,4\text{-}Quin)(MeOH)]$ indicated that it reacts faster than *fac*-$[Re(CO)_3(2,4\text{-}Quin)(MeOH)]^5$ with k_1 values of 4.5 ± 0.2 $M^{-1}\,s^{-1}$ and 0.0031 ± 0.0002 $M^{-1}s^{-1}$ respectively. The manganese complex proved to be ~1150 times faster than the rhenium complex in the reactions with pyridine. The k_{-1} values are reported as 40 × 10^{-3} ± 1 s^{-1} and 0.051 × 10^{-3} ± 0.007 s^{-1} respectively and this indicates that the reverse reaction is ~784 times faster for the manganese complex. The equilibrium constants were reported as 113 ± 29 M^{-1} and 195 ± 97 M^{-1} respectively, with the rhenium complex *fac*-$[Re(CO)_3(2,4\text{-}Quin)(Py)]$ once again more stable than the manganese complex.
- In the case of *fac*-$[Mn(CO)_3(Pico)(MeOH)]$ and *fac*-$[Re(CO)_3(Pico)(MeOH)]$ it is observed that the manganese substitution reactions are ~600 times faster than the rhenium complex with pyridine as entering ligand with k_1 values reported as 0.94 ± 0.01 $M^{-1}\,s^{-1}$ and 0.00159 ± 0.00001 $M^{-1}\,s^{-1}$. The k_{-1} values of 0.16 × 10^{-3} ± 0.07 s^{-1} and 0.008 × 10^{-3} ± 0.001 s^{-1} respectively indicates that the

manganese complex's reverse reaction is again faster than the rhenium complex (~16 times) while the equilibrium constants also proved the rhenium complex to be more stable than the manganese complex with K_1 values reported as 7231 ± 3894 M^{-1} and 199 ± 25 M^{-1} respectively.

- In the reactions with bromide ions *fac*-[$Mn(CO)_3$(Pico)(MeOH)] was ~360 times faster than the *fac*-[$Re(CO)_3$(Pico)(MeOH)] reaction with reported k_1 values of 4.31 ± 0.02 M^{-1} s^{-1} and 0.0118 ± 0.0001 M^{-1} s^{-1} respectively. The reverse reactions showed the manganese complex to be ~31 times faster than the rhenium with k_{-1} values reported as 25 × 10^{-3} ± 1 s^{-1} and 0.8 × 10^{-3} ± 0.1 s^{-1} respectively while the equilibrium constants were reported as 172 ± 7 M^{-1} and 15 ± 2 M^{-1} respectively. In this case, the manganese complex *fac*-[$Mn(CO)_3$(Pico)(Br)]$^-$ is more stable than the rhenium complex.

The negative $\Delta S^{\dagger}$ values reported throughout point towards an associative interchange mechanism, but more evidence is required to confidently report on the intimate mechanism for the methanol substitution in the Mn (I) complexes.

To summarize, it was shown that the N,O-bidentate ligands affected the rate of methanol substitution quite substantially, as was found for the corresponding Re (I) complexes. This work also proves that Mn (I) tricarbonyl could in principle be used as model radiopharmaceuticals for rhenium and technetium.

6 Evaluation of this study

6.1 Results

The following Mn(I) complexes were successfully synthesized and fully characterized: *fac*-$[Mn(CO)_3(N,N'\text{-Bid})(X)]^+$ and *fac*-$[Mn(CO)_3(N,O\text{-Bid})(X)]$ with N,N'-Bid = 1,10-phenanthroline (Phen) and 2,2'-bipyridine (Bipy), N,O-Bid = picolinic acid (Pico) and quinoline-2,4-dicarboxylic acid (2,4-Quin) and X= H_2O and MeOH.

The crystal structures of *fac*-$[Mn(CO)_3(Phen)(H_2O)][CF_3SO_3]$ and *fac*-$[Mn(CO)_3(Bipy)(H_2O)][CF_3SO_3]$ are reported in Chapter 4. A CSD search at the time of the study revealed only fifty five Mn (I) tricarbonyl complexes with N,N'-Bid and only three with N,O-Bid ligands in literature.[1] Also, the two aqua complexes reported here (H_2O ligand in the sixth/axial position) are two of the very few reported in literature with only five reported at the time of this study. The four Mn(I) tricarbonyl complexes with the different monodentate entering ligands (Py, TU, Br^-), were also fully characterized and reported in Chapter 3, which serves as confirmation of the kinetic end products. Unfortunately we were unable to find crystals suitable for single crystal x-ray diffraction of these products. The complexes reported in this study contribute significantly to the already available database of Mn (I) tricarbonyl complexes.

The methanol substitution reactions between *fac*-$[Mn(CO)_3(Phen)(MeOH)]^+$ and *fac*-$[Mn(CO)_3(Pico)(MeOH)]$ and different entering ligands, pyridine (Py), thiourea (TU) and bromide ions (Br^-) were monitored at 15.0 °C, 25.0 °C, 35.0 °C and 45.0 °C. For *fac*-$[Mn(CO)_3(Bipy)(MeOH)]^+$ and *fac*-$[Mn(CO)_3(2,4\text{-Quin})(MeOH)]$, the reactions with Py, TU and Br^- and Py and TU respectively were monitored at 25.0 °C. The following overall trend was found for k_1: *fac*-$[Mn(CO)_3(Phen)(MeOH)]^+$ ~ *fac*-$[Mn(CO)_3(Phen)(MeOH)]^+$ < *fac*-$[Mn(CO)_3(Pico)(MeOH)]$ < *fac*-$[Mn(CO)_3(2,4\text{-Quin})(MeOH)]$. The following trend for the N,O-bidenate comoplexes with different ligands was found: Br- < Py < TU. With the N,N'-bidentate complexes, the reactions with Br^- was found to be the fastest, thiourea second and pyridine the slowest. This

[1] Cambridge Structural Database (CSD), Version 5.34, Nov 2012 update. F.H. Allen, *Acta Cryst.*, **B58**, 2002, 380. Date Accessed : October 2013.

change might be due to electronic effects between the positively charged N,N'-bidentate complexes and the negatively charged bromide ions.

From the k_{-1} values obtained it was found that the reactions with bromide ions have the highest k_{-1} values each time. Between the reactions with thiourea and pyridine, no trend could be found for k_{-1}. The $\Delta S^{\dagger}$ values for the reactions of *fac*-$[Mn(CO)_3(Phen)(MeOH)]^+$ and *fac*-$[Mn(CO)_3(Pico)(MeOH)]$ with pyridine, thiourea and Br- are all small negative values with relatively large esd's indicate an interchange associative mechanism. High pressure studies need to be performed in order to unambiguously determine the mechanism of these reactions.

Overall these results found in this kinetic study correlates with the data reported by Schutte *et al*.[2]

6.2 Future Research

The expansion of this study in terms of more bidentate ligand systems, specifically to O,O'-donor atom ligand systems for these Mn (I) tricarbonyl complexes should be part of future research. For the Re (I) complexes, these ligand systems proved to be the most reactive. If the trend found for the Re (I) complexes is followed for the Mn (I) complexes, one could expect an incredible reactive metal centre.

Also, synthesis of water soluble Mn (I) tricarbonyl complexes in order to evaluate the aqueous kinetics of these systems is another priority. High pressure studies must be performed on these systems to determine the intimate mechanism of the reactions.

The expansion on the available crystal structure library, specifically the O,O'-bidentate systems, should be another future aim as well as a study in which these manganese complexes are used as rhenium models.

[2] Schutte, M., Kemp, G., Visser, H.G., Roodt, A., *Inorg. Chem.,* **50**,2011,12486.